

High-precision laser spectroscopy of helium-like carbon $^{12}\text{C}^{4+}$

Hochpräzise Laserspektroskopie von heliumähnlichem Kohlenstoff $^{12}\text{C}^{4+}$

Zur Erlangung des Grades eines Doktors der Naturwissenschaften (Dr. rer. nat.)

Genehmigte Dissertation von Phillip Imgram aus Seligenstadt

Tag der Einreichung: 15. November 2022, Tag der Prüfung: 21. Dezember 2022

1. Gutachten: Prof. Dr. Wilfried Nörtershäuser

2. Gutachten: Prof. Dr. Joachim Enders

Darmstadt, Technische Universität Darmstadt



TECHNISCHE
UNIVERSITÄT
DARMSTADT

Fachbereich Physik
Institut für Kernphysik
AG Nörtershäuser



High-precision laser spectroscopy of helium-like carbon $^{12}\text{C}^{4+}$
Hochpräzise Laserspektroskopie von heliumähnlichem Kohlenstoff $^{12}\text{C}^{4+}$

Accepted doctoral thesis by Phillip Ingram

Date of submission: 15. November 2022

Date of thesis defense: 21. Dezember 2022

Darmstadt, Technische Universität Darmstadt

Bitte zitieren Sie dieses Dokument als:

URN: urn:nbn:de:tuda-tuprints-230828

URL: <http://tuprints.ulb.tu-darmstadt.de/23082>

Jahr der Veröffentlichung auf TUprints: 2023

Dieses Dokument wird bereitgestellt von tuprints,

E-Publishing-Service der TU Darmstadt

<http://tuprints.ulb.tu-darmstadt.de>

tuprints@ulb.tu-darmstadt.de

Die Veröffentlichung steht unter folgender Creative Commons Lizenz:

Namensnennung 4.0 International

<https://creativecommons.org/licenses/by/4.0/>

This work is licensed under a Creative Commons License:

Attribution 4.0 International

<https://creativecommons.org/licenses/by/4.0/>

Erklärungen laut Promotionsordnung

§ 8 Abs. 1 lit. c PromO

Ich versichere hiermit, dass die elektronische Version meiner Dissertation mit der schriftlichen Version übereinstimmt.

§ 8 Abs. 1 lit. d PromO

Ich versichere hiermit, dass zu einem vorherigen Zeitpunkt noch keine Promotion versucht wurde. In diesem Fall sind nähere Angaben über Zeitpunkt, Hochschule, Dissertationsthema und Ergebnis dieses Versuchs mitzuteilen.

§ 9 Abs. 1 PromO

Ich versichere hiermit, dass die vorliegende Dissertation selbstständig und nur unter Verwendung der angegebenen Quellen verfasst wurde.

§ 9 Abs. 2 PromO

Die Arbeit hat bisher noch nicht zu Prüfungszwecken gedient.

Darmstadt, 15. November 2022

P. Imgram

Abstract

The size of an atomic nucleus is a fundamental observable and defined by the distribution of the neutrons and protons composing the nucleus and the respective mean-square radii. The precise investigation of the nuclear size across the chart of nuclides delivers important benchmarks for nuclear structure theory and tests our fundamental knowledge of matter. In contrast to matter and neutron radii, the nuclear charge radius can be probed through the well-known electromagnetic interaction. Different techniques have been developed over time to measure nuclear charge radii such as elastic electron scattering or muonic atom spectroscopy. While these techniques are typically limited to stable nuclei, collinear laser spectroscopy and resonant ionization spectroscopy are used to determine nuclear charge radii of short-lived radioactive isotopes relative to a reference charge radius of a stable isotope. In some cases, this can limit the uncertainty of the obtained charge radii of radioactive nuclei to the uncertainty of the reference measurements from elastic electron scattering or muonic atom spectroscopy.

To overcome this limit in light mass nuclei like $^{10,11}\text{B}$, an all-optical approach for the charge radius determination purely from laser spectroscopy measurements and non-relativistic QED calculations was tested in this work with the well-known nucleus of ^{12}C through laser excitation of helium-like $^{12}\text{C}^{4+}$ from the metastable $1s2s\ ^3\text{S}_1$ state with a lifetime of 21 ms to the $1s2p\ ^3\text{P}_J$ states. The high-precision collinear laser spectroscopy was performed at the Collinear Apparatus for Laser Spectroscopy and Applied Science (COALA), situated at the Institute for Nuclear Physics at the Technical University Darmstadt. In order to produce the the highly charged C^{4+} ions, a new electron beam ion source including a Wien filter for charge/mass separation was installed and commissioned at COALA. Additionally, a new switchyard and beam diagnostics were designed, built and installed. The $1s2s\ ^3\text{S}_1 \rightarrow 1s2p\ ^3\text{P}_J$ rest-frame transition frequencies were determined with less than 2 MHz uncertainty through quasi-simultaneous collinear and anticollinear laser spectroscopy. These transition frequencies are in excellent agreement with state-of-the-art *ab initio* atomic structure calculations and an all-optical nuclear charge radius of ^{12}C was extracted. Its accuracy is limited by theory, which must be improved by two orders of magnitude before the experimental uncertainty becomes significant again. At that point, the accuracy of the extracted charge radius would have already outperformed all previous measurements of this observable. Furthermore, the high precision of this work enabled the estimation of the next missing order in the atomic structure calculations and the transition frequencies from this work can be used together with ongoing measurements in $^{13}\text{C}^{4+}$ for a conventional determination of the mean-square charge radius difference $\delta\langle r^2 \rangle^{12,13}$ between ^{12}C and ^{13}C which has not been measured so far by laser spectroscopy.

Zusammenfassung

Kollineare Laserspektroskopie und die Resonanz-Ionisations-Spektroskopie werden typischerweise verwendet, um Kernladungsradien von kurzlebigen radioaktiven Isotopen relativ zu einem Referenzladungsradius eines stabilen Isotops zu bestimmen. In manchen Fällen kann dies die Unsicherheit der erhaltenen Ladungsradien radioaktiver Kerne auf die Unsicherheit der Referenzmessungen aus der elastischen Elektronenstreuung oder der myonischen Atom-spektroskopie limitieren.

Um dieses Limit in Kernen mit leichter Masse wie $^{10,11}\text{B}$ zu überwinden, wurde in dieser Arbeit ein rein optischer Ansatz für die Ladungsradienbestimmung basierend auf Laserspektroskopiemessungen und nicht-relativistischen QED Rechnungen mit dem bekannten Kern von ^{12}C getestet. Dafür wurden heliumähnliche $^{12}\text{C}^{4+}$ Ionen durch einen Laser aus dem metastabilen $1s2s\ ^3\text{S}_1$ Zustand, der eine Lebensdauer von 21 ms besitzt, in die $1s2p\ ^3\text{P}_J$ Zustände angeregt. Die hochpräzise kollineare Laserspektroskopie wurde an der Kollinearen Apparatur für Laserspektroskopie und Angewandte Wissenschaft (KOALA) am Institut für Kernphysik der TU Darmstadt durchgeführt. Um die hochgeladenen C^{4+} Ionen zu produzieren, wurde eine Elektronenstrahl-Ionenquelle und ein Wien-Filter zur Separation des Ladung-zu-Masse-Verhältnis an KOALA installiert und in Betrieb genommen. Außerdem wurden eine neue Überlagerungseinheit (Switchyard) und eine neue Strahldiagnostik entworfen, gebaut und installiert. Die Kombination dieser Neuerungen erlaubte es erstmals die Ruhfrequenzen der $1s2s\ ^3\text{S}_1 \rightarrow 1s2p\ ^3\text{P}_J$ Übergänge mit weniger als 2 MHz Unsicherheit zu bestimmen. Dies gelang mittels quasi-simultaner kollinear und antikollinear Laserspektroskopie bei der sich zahlreiche systematische Unsicherheiten konventioneller kollinearer Spektroskopie eliminieren lassen. Die ermittelten Übergangsfrequenzen sind in exzellenter Übereinstimmung mit modernsten *ab initio* Atomstrukturrechnungen und mit deren Hilfe wurde ein rein optischer Kernladungsradius von ^{12}C extrahiert. Dessen Genauigkeit ist noch durch die Genauigkeit der theoretischen Berechnungen limitiert, welche um zwei Größenordnungen verbessert werden müssten, bevor die experimentelle Unsicherheit wieder signifikant wird. Dann würde die Genauigkeit des aus den hier durchgeführten Messungen extrahierten Ladungsradius alle bisherigen Bestimmungen übertreffen. Zusätzlich ermöglicht die hier erreichte hohe Präzession eine Abschätzung der nächsthöheren, noch nicht berechneten Ordnung in den Atomstrukturrechnungen. Schließlich erlauben die gemessenen Übergangsfrequenzen zusammen mit noch laufenden Messungen in $^{13}\text{C}^{4+}$ und konventionellen Berechnungen des Masseneffekts in der Isotopieverschiebung eine sehr genaue laserspektroskopische Bestimmung der Differenz der mittleren quadratischen Kernladungsradien von ^{12}C und ^{13}C , welche bislang noch nicht mittels Laserspektroskopie gemessen wurde.

Contents

1	Motivation	1
1.1	Nuclear structure of light nuclei	1
1.2	Atomic structure of He-like systems	5
2	Theoretical background	7
2.1	Nuclear and atomic properties of $^{12}\text{C}^{4+}$	7
2.2	Atomic structure calculations of He-like systems	8
2.3	Highly charged ions from electron beam ion sources	10
2.3.1	Direct Coulomb ionization	13
2.3.2	Charge exchange	13
2.3.3	Radiative recombination	14
2.3.4	Further processes	14
2.3.5	Ion confinement	15
2.3.6	Ion-energy distribution and ion heating	16
2.3.7	Energy exchange between ions	17
2.3.8	Ion losses and evaporative cooling	17
2.3.9	Balance equation for the ion charge state distribution	18
2.3.10	EBIS simulations	19
2.4	Collinear laser spectroscopy	21
2.4.1	Laser beam alignment	22
2.4.2	Line shape	23
2.4.3	Photon recoil	24
2.4.4	Zeeman effect	25
3	The COALA setup	27
3.1	Dresden EBIS-A	28
3.2	Switchyard	30
3.3	Diagnostic stations	32
3.4	Laser system	34
4	EBIS-A ion production	37
4.1	Pulsed mode	37
4.2	Production of $^{12}\text{C}^{4+}$ in pulsed mode	38
4.2.1	Electron current vs. trap depth	39
4.2.2	Feeding gas pressure and breeding time	40
4.3	Transmission and leaky mode	40

5	Collinear laser spectroscopy with $^{12}\text{C}^{4+}$ ions	43
5.1	Characterization of $^{12}\text{C}^{4+}$ spectra with a single laser system	43
5.1.1	Resonance spectra with a bunched ion beam	43
5.1.2	Resonance spectra with a continuous ion beam	46
5.1.3	Systematic drift of the line center	48
5.2	Transition frequency determination in quasi-simultaneous collinear and anti-collinear laser geometry	50
5.2.1	Systematic effects in quasi-simultaneous collinear and anticollinear laser spectroscopy	51
5.2.2	$^3\text{S}_1 \rightarrow ^3\text{P}_J$ rest-frame transition frequencies	58
5.2.3	Fine-structure splitting	61
5.3	All-optical nuclear charge radius of ^{12}C	62
6	Summary and outlook	65
A	Appendix	69
A.1	Spatial velocity distribution simulation	69
	Bibliography	xv
	Curriculum Vitae	xxv
	List of publications	xxvii
	Acknowledgments	xxxi

List of Figures

1.1	Nuclear charge radii of He, Li, Be and B isotopes	3
1.2	Illustration of the all-optical approach for the nuclear charge radius determination	4
2.1	Relevant energy levels of $^{12}\text{C}^{4+}$	7
2.2	Ionization factors and electron energies to achieve a specific charge state	12
2.3	Confinement potentials in an electron beam ion source	15
2.4	Results of EBIS simulations with <i>ebisim</i>	20
2.5	Frequency shift estimation due to beam misalignment	23
2.6	Zeeman splitting of the $^{12}\text{C}^{4+}$ fine structure	26
3.1	Overview of the COALA beamline	27
3.2	The Dresden EBIS-A at COALA	29
3.3	The new switchyard for COALA	31
3.4	SIMION simulation of the new switchyard	31
3.5	The upgraded diagnostic stations.	32
3.6	Ion and laser beam overlap on a MCP stack.	33
3.7	Laser setup for the C^{4+} spectroscopy at COALA	34
4.1	EBIS output in pulsed mode with residual gas	37
4.2	Velocity filter scans in pulsed mode for three different breeding times	38
4.3	Number of C^{4+} ions for several trap depths and electron currents	39
4.4	Number of C^{4+} ions for several propane gas pressures and breeding times	40
4.5	Comparison between leaky mode and transmission mode	40
5.1	Time-resolved spectra in bunched beam mode	44
5.2	Comparison between bunched mode spectra and continuous mode spectra	47
5.3	Relative line-center drift	49
5.4	Line-shape analysis of collinear spectra	51
5.5	Systematic frequency shift for ion-laser beam misalignment	52
5.6	Experimental frequency shift due to laser-laser beam misalignment	53
5.7	Power dependency of the rest-frame transition frequency	55
5.8	Scan voltage difference δU dependency of the rest-frame transition frequency.	57
5.9	Comparison between linear and circular laser light polarization	58
5.10	Single frequency measurements of the $1s2s\ ^3\text{S}_1 \rightarrow 1s2p\ ^3\text{P}_J$ transitions	59
5.11	Rest-frame transition frequency comparison to literature values	60
5.12	Comparison of all available ^{12}C charge radii	63



6.1	"Pathway" to the halo distance d_{halo} of ^8B	67
A.1	Simulation of the spatial velocity distribution shift	71

List of Tables

2.1	Calculated transition energy ΔE_p and the respective field-shift factor F	10
2.2	Parameters for the cross-section of charge exchange	14
5.1	EBIS production parameters of the shown spectra	45
5.2	SNR comparison of the spectra (a) and (d) in Fig. 5.2	48
5.3	Estimated photon scattering in resonance	55
5.4	Results of the rest-frame transition frequency determination	59
5.5	Rest-frame transition frequency comparison to literature values	61
5.6	Fine-structure splitting of the $1s2p\ ^3P_J$ levels in $^{12}\text{C}^{4+}$	61
5.7	Parameters for the all-optical nuclear charge radius determination	62

1 Motivation

The fruitful interplay between atomic and nuclear physics continuously leads to new discoveries and knowledge about our fundamental building blocks of matter through the refinement of their theory and experiments for more than a century. The discovery that most of the mass of an atom is located in a compact massive center by E. Rutherford (1911) [1] enabled the explanation of observed spectral lines in hydrogen, postulating a quantized angular momentum by N. Bohr (1913) [2]. Later, the precise observation of the hydrogen lines resulted in the discovery of deuterium by H. Urey (1932) [3]. The steady increase in precision of spectroscopy experiments challenged theory and resulted in the discovery of relativistic and quantum electrodynamical (QED) corrections [4] in the atomic shell, but also allowed new insights into the nucleus. The observation of the hyperfine structure splitting led to the proposal of the existence of a nuclear spin and the related nuclear magnetic moment [5, 6]. Later, the deviation from the Landé-interval rule in $^{151,153}\text{Eu}$ was explained as a deviation of the nucleus from a spherical form [7]. Thus, a nuclear quadrupole moment and a nuclear deformation was introduced. With the development of the laser, highly precise investigations of these properties in ground states of even short-lived radioactive nuclei became possible and have been driven by the workhorses collinear laser spectroscopy (CLS) and resonant ionization spectroscopy (RIS) in the last decades [8–10]. However, to extract nuclear moments from the recorded hyperfine spectra, reliable and precise state-of-the-art atomic structure calculations are needed as used in, e.g., [11]. The determination of nuclear charge radii from isotope shift measurements also requires the precise calculation of the corresponding field-shift and mass-shift constant when an element has less than 3 stable isotopes. This is particularly challenging in the lightest elements where the mass shift is about 10000 times larger than the field shift and has, thus, to be calculated with an accuracy of about 10 parts-per-million (ppm). In the last two decades, *ab initio* methods like non-relativistic QED calculations have been pushed to accommodate such calculations up to 5-electron systems [12].

Thus, atomic and nuclear physics should not be seen as two different disciplines but rather as vital partners where both profit from their progress. The laser spectroscopy of helium-like $^{12}\text{C}^{4+}$ can be therefore motivated from two different perspectives as will be discussed in the two following sections.

1.1 Nuclear structure of light nuclei

The size of a nucleus is a fundamental observable and several techniques were developed to measure it since its discovery by Rutherford and coworkers [1]. Due to its composition of protons and neutrons, one has to distinguish between a matter radius with respect to

the combined proton and neutron (nucleon) distribution, the neutron radius and the charge radius, referring to the neutron and proton distribution, respectively. While the matter radius can only be probed in nuclear reactions and is therefore affected with a considerable model dependence, the electromagnetic interaction is well understood. Thus, accurate charge radii can be determined from the electron-nucleus interaction either of free high energy electrons in electron scattering [13] or of bound electrons or muons [14] from the finite nuclear size effect in atomic or muonic spectra, respectively. Generally, a mean-square radius of the relevant distribution $\rho(\vec{r})$ is the experimental observable, i.e., in case of the charge distribution

$$\langle r_c^2 \rangle = \frac{1}{Z} \int d^3r \, r^2 \rho_c(\vec{r}), \quad (1.1)$$

and the corresponding (charge) radius is defined as $R_c = \sqrt{\langle r_c^2 \rangle}$. While elastic electron scattering and muonic atom spectroscopy deduce absolute nuclear charge radii R_c^A of stable isotopes, the isotope shift in optical spectra, i.e., the frequency difference of a transition between two isotopes

$$\delta\nu^{AA'} = \nu^{A'} - \nu^A = K_{\text{MS}} \frac{M_{A'} - M_A}{M_A M_{A'}} + F \delta \langle r_c^2 \rangle^{AA'}, \quad (1.2)$$

allows to extract changes in the mean-square nuclear charge radius between a stable and a radioactive isotope with mass number A and A' , respectively. The nuclear charge radius of the radioactive nucleus (A') is then referenced to a R_c^A measurement of the stable nucleus by

$$R_c^{A'} = \sqrt{(R_c^A)^2 + \delta \langle r_c^2 \rangle^{AA'}}. \quad (1.3)$$

While nuclear charge radii globally scale with the nuclear mass as $\sqrt[3]{A}$, the individual size and especially its variation across an isotopic chain of an element exhibits a rich structural diversity caused by underlying nuclear structure like nuclear shell closures, shape changes, shape coexistence, or pairing correlations. Therefore, each mass region in the nuclear chart exhibits different features which test nuclear structure theories and therefore our fundamental knowledge of matter. One of these especially challenging features are so-called halo nuclei which are very prominent in the region of the lightest nuclei ($A \leq 12$). The two-neutron halo ^{11}Li is one of the most prominent examples. It consists of a ^9Li core and a halo of diluted nuclear matter formed by the two valence neutrons. The large extension of the wave function caused by the small binding energies of the valence nucleons [15, 16] leads to large interaction cross sections [17] and a narrow momentum distribution of the halo nucleons in breakup reactions [18, 19]. Even though the halo consists of neutron matter, a strong increase in the nuclear charge radius is observed as illustrated in Fig. 1.1. This is also the case for ^6He , ^8He and the one-neutron halo nucleus ^{11}Be [20]. It is caused by the center-of-mass motion of the nuclear core and the halo neutrons, which smears out the nuclear charge distribution and, thus, strongly increases the nuclear charge radius in comparison to the neighbouring isotope. This is illustrated in the insets of Fig. 1.1 for the case of $^{6,8}\text{He}$.

For the proposed proton halo nucleus ^8B , the situation is different, since the halo is formed by the proton and directly contributes to the charge radius. Therefore, the increase in the nuclear charge radius is expected to be especially large. First indications towards a proton halo

character of ^8B came from its surprisingly large quadrupole moment measured with β -NMR [21, 22]. Then, various attempts have been made in the past to extract the decisive halo distance d_{halo} between the ^7Be core and the valence (halo) proton from the $^8\text{B} \rightarrow ^7\text{Be} + p$ breakup reaction in thin targets [23–26] and from precise mass radii measurements [27]. However, the results of these experiments contain a model dependency which allows for different interpretations regarding the halo character of ^8B . Therefore, a model-independent measurement is needed to extract d_{halo} of ^8B to make a definite statement about its halo character. This can be provided by laser spectroscopy as it can access the mean-square nuclear charge radius of ^7Be and ^8B model-independently.

As mentioned above, collinear laser spectroscopy is a proven technique to measure nuclear charge radii of radioactive nuclei, but it relies on nuclear charge radii of the stable isotopes from other measurements as is obvious from Eq. (1.3). This connects the uncertainty $\Delta R_c^{A'}$ to ΔR_c^A which can limit the reachable accuracy of $R_c^{A'}$ like in the case of the lithium isotopic

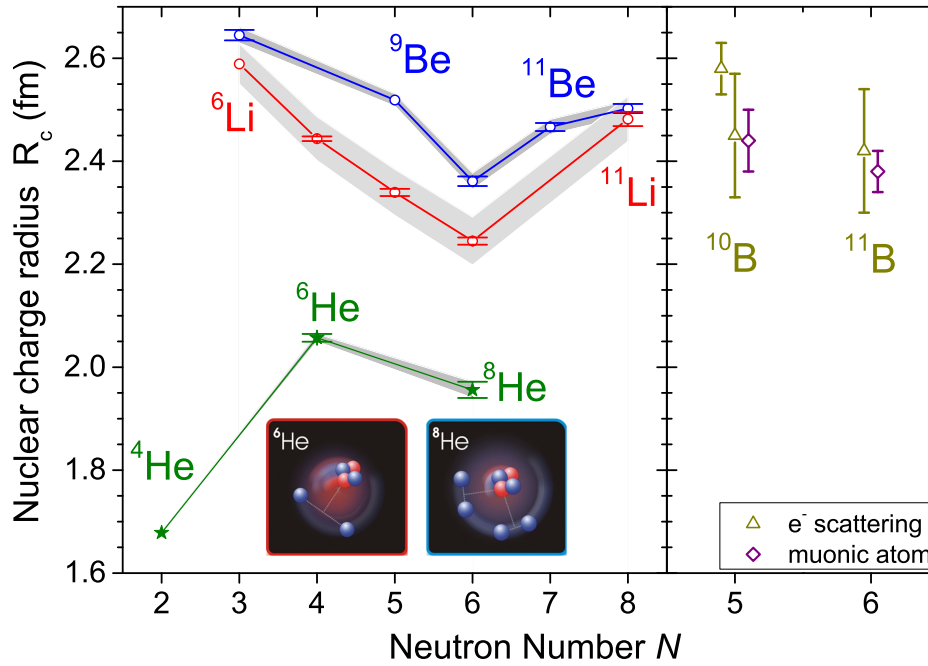


Figure 1.1: *Left panel:* Nuclear charge radii of the helium ($Z = 2$), lithium ($Z = 3$), and beryllium ($Z = 4$) isotopes. The stable reference isotopes and halo isotopes are marked with labels. The error bars represent the uncertainties from the respective isotope-shift measurements, whereas the grey bands show the combined uncertainty including the uncertainty of the reference radius. In the depiction of the nuclear structure of ^6He and ^8He , red spheres represent protons and blue spheres represent neutrons. It illustrates how the nuclear charge distribution is smeared out by the center-of-mass motion of the charge carrying α particle core and the halo neutrons. *Right panel:* Nuclear charge radii of boron ($Z = 5$) isotopes determined from elastic electron scattering and muonic atom spectroscopy.

chain (see Fig. 1.1) and especially the boron isotopic chain. The charge radius of the stable nuclei ^{10}B and ^{11}B derived from electron scattering has a comparably low precision on the 5 % level due to an interference of two scattering components [28, 29] and also muonic atom spectroscopy delivers results only on the 1.6 % level [30]. In comparison, the precision of $\delta \langle r_c^2 \rangle^{11,8}$ between ^{11}B and ^8B extracted from laser spectroscopy is estimated to be on the 4 % level, which would translate in a relative accuracy on the 0.7 % level for R_c of ^8B if the nuclear charge radius of ^{11}B was known precisely [31]. Therefore, new measurements of the absolute nuclear charge radius of $^{10,11}\text{B}$ with higher precision than previous experiments are required. In principle, this can be provided in an all-optical approach with the $1s2s\ ^3S_1 \rightarrow 1s2p\ ^3P_J$ transitions in He-like systems as illustrated in Fig. 1.2, motivated in Sec. 1.2 and explained in Sec. 2.2. A successful application of this method to ^9Be and $^{10,11}\text{B}$ would base all measurements needed for the investigation of ^8B on equal footing. In order to verify this approach, first measurements of He-like $^{12}\text{C}^{4+}$ were carried out and are reported in this thesis. The charge radius of ^{12}C is well-known from elastic electron scattering [33–36] and from muonic atom spectroscopy [37, 38] and the results from both approaches are in good agreement. Thus, the results constitute a strong anchor point for upcoming progress in atomic structure theory. They also represent the first high-precision measurement in a He-like system beyond He with the exception of Li^+ . Additionally, the carbon isotopic chain has not been studied with high-precision laser spectroscopy so far since no suitable transitions exist in the level structure

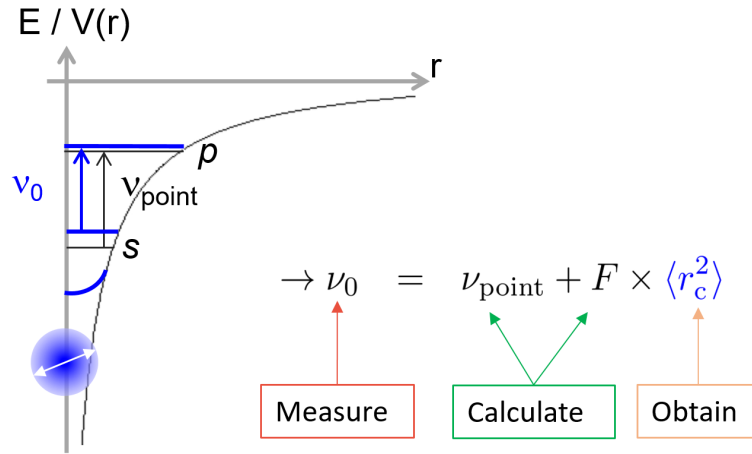


Figure 1.2: Illustration of an all-optical approach for the nuclear charge radius determination. The rest-frame transition frequency ν_0 in an atomic system is the sum of the transition frequency under assumption of a point-like nucleus ν_{point} and the finite nuclear size effect $\delta\nu_{\text{FS}} = F \cdot \langle r_c^2 \rangle$. The latter modifies the binding potential $V(r)$ inside the nucleus and with it the binding energies E of the electronic states (blue lines). The mean-square charge radius can be obtained by measuring the transition frequency ν_0 and calculating ν_{point} and F in an appropriate atomic system. This method has been demonstrated so far in hydrogen and hydrogen-like systems, while helium-like systems came just in reach with the most recent atomic structure calculations [32].

of C and C⁺ starting in the ground state or a higher lying but metastable state that can be efficiently populated in standard ion sources. The precise determination of the $1s2s\ ^3S_1 \rightarrow 1s2p\ ^3P_J$ transition frequencies will therefore also serve as the starting point for a first $\delta \langle r_c^2 \rangle^{12,A'}$ extraction from isotope shift measurements in the carbon isotopic chain. A measurement of $^{13}\text{C}^{4+}$ is currently ongoing, which will provide an accurate measurement of $\delta \langle r_c^2 \rangle^{12,13}$ based on precise mass-shift calculations in the He-like system. Agreement with the known value will strongly support the consistency of the mass-shift calculations as well as of the transition frequency measurements at the COALA beamline.

1.2 Atomic structure of He-like systems

The calculation of energy levels in one-electron systems has reached a precision level which enables the extraction of absolute nuclear charge radii purely from laser spectroscopic measurements as demonstrated in hydrogen [39], muonic hydrogen [40], muonic deuterium [41] and muonic helium [42]. The observed discrepancy in muonic hydrogen compared to atomic hydrogen lead to the famous proton radius puzzle [43]. Meanwhile, convincing evidence for the smaller proton radius as observed in muonic hydrogen comes from improved measurements of hydrogen [44], a new lamb-shift measurement [45] as well as electron scattering at very low q^2 using a windowless target [46]. However, some of the results are still heavily discussed and hydrogen experiments that support the larger proton radius are also reported [47, 48]. Therefore, a more elaborate comparison between muonic and electronic systems beyond hydrogen is demanded. In order to extend this approach towards heavier atomic systems ($Z > 1$), it is necessary to precisely calculate energy levels in two-electron systems since no laser addressable transitions exist in H-like systems for $Z > 1$. Related non-relativistic QED (NRQED) calculations made significant progress recently [32, 49–51] and surpassed all available experimental data beyond He in precision and accuracy. Therefore, new high-precision data for $Z > 2$ is requested. In return, absolute nuclear charge radii can be determined purely from laser spectroscopic measurements and NRQED calculations as explained in Sec. 2.2.

Furthermore, accurate fine-structure splitting measurements in the $1s2p\ ^3P_J$ states of He can be used in combination with NRQED calculations to obtain the fine-structure constant α as demonstrated in [52]. Here, the stated uncertainty of α is dominated by the next missing order in the NRQED calculations. It was suggested that a precise measurement of the fine-structure splitting in $^{12}\text{C}^{4+}$ could help to derive an estimate for the next order contribution.

The targeted accuracy of 2 MHz in the $1s2s\ ^3S_1 \rightarrow 1s2p\ ^3P_J$ transition frequency measurements of $^{12}\text{C}^{4+}$ within this work will serve as benchmark for NRQED calculations and will therefore help to refine these atomic structure calculations.

2 Theoretical background

This chapter contains the necessary theoretical background to understand the properties of He-like carbon, atomic theory calculations in He-like systems, their production in an electron beam ion source and the investigation through quasi-simultaneous collinear and anticollinear laser spectroscopy. Furthermore, physical effects that might lead to systematic uncertainties in this approach are explained.

2.1 Nuclear and atomic properties of $^{12}\text{C}^{4+}$

The nucleus of ^{12}C consists of 6 Protons and 6 Neutrons with a natural abundance of $\approx 99\%$. The nuclear charge radius of ^{12}C is precisely known from a muonic atom spectroscopy measurement to $R_C = 2.4829(19)$ [38], but also less accurate results from elastic electron scattering [33–36] exist and are in good agreement with the muonic results. The ground-state nuclear spin is $I = 0$ and therefore no hyperfine splitting occurs in the atomic level structure. However, no suitable transition for laser spectroscopy exists in the level structure of C and C^+ starting in the ground state or a higher lying but metastable state that can be efficiently populated in standard ion sources. Therefore, the only way for high-precision laser spectroscopic investigations with non-relativistic ions ($v \ll c$) is using highly charged C^{4+} ions. It has two electrons and is therefore part of the He-like isoelectronic sequence. Here, the two electron spins can be either aligned antiparallel or parallel, which results in a total electron spin of $S = 0$ or $S = 1$. This leads to a separation of the level structure in singlet ($S = 0$) and triplet ($S = 1$) states as illustrated in Fig. 2.1.

For $S = 0$, no laser accessible transition exists from the $1s^2\ ^1S_0$ ground state since the energy difference to the next excited state is of the order of 300 eV which corresponds to a wavelength of 4 nm. This photon energy could only be reached with free electron lasers like the European

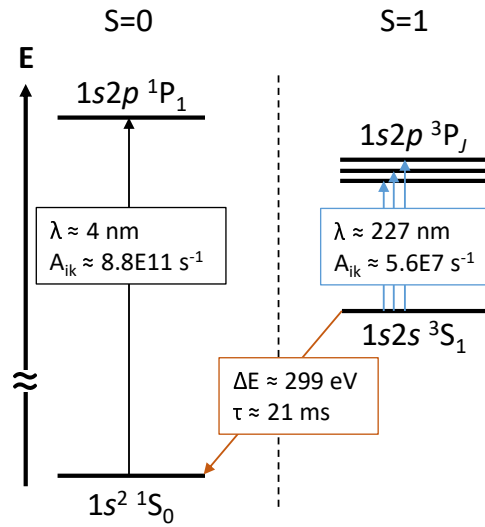


Figure 2.1: Level scheme of $^{12}\text{C}^{4+}$ with the ground state $1s^2\ ^1S_0$ and the first excited states. Not to scale.

XFEL¹. Furthermore, the natural linewidth in this transition is approximately 140 GHz due to the extremely short 1P_1 lifetime of only 1 ps. This excludes the transition from high-precision laser spectroscopy.

For $S = 1$, the $1s2s\ ^3S_1$ state is the starting point for the almost closed $1s2s\ ^3S_1 \rightarrow 1s2p\ ^3P_J$ transitions which have a transition wavelength $\lambda \approx 227$ nm in the UV and a spontaneous decay rate $A_{ik} \approx 5.6 \cdot 10^7$ 1/s which corresponds to a natural linewidth of 8.9 MHz. The branching ratio from the $1s2s\ ^3P_J$ states to the ground state is only 0.04 %. The lifetime of the metastable $1s2s\ ^3S_1$ state is about $\tau \approx 21$ ms in C^{4+} which calls for a fast laser spectroscopic technique once the ions are extracted from the source. Laser spectroscopy of short-lived isotopes with comparable lifetimes are routinely performed with collinear laser spectroscopy (CLS).

Furthermore, recent progress in atomic theory brought two-electron systems like C^{4+} in reach of *ab initio* atomic structure calculations. Precision laser spectroscopy is, thus, of high interest since it allows to test these calculations as well as a source for nuclear structure investigations as soon as theory is sufficiently advanced.

2.2 Atomic structure calculations of He-like systems

He-like ions are two-electron systems and the simplest many-body problem for atomic structure calculations. Since it requires the inclusion of all electron-electron correlations, different strategies have been developed to solve this problem. The most precise solution in light ions is from non-relativistic QED (NRQED) calculations [32]. Details on this technique can be found in [32, 49, 51]. Here, only the principle idea and some basic considerations are briefly explained. For two electrons at position \vec{r}_1 and \vec{r}_2 bound to a nucleus, the corresponding Hamiltonian in the center-of-mass frame is given by [53, p. 199]

$$H = -\frac{\hbar^2}{2m_e} \left(\vec{\nabla}_1^2 + \vec{\nabla}_2^2 + \frac{\mu}{M} \vec{\nabla}_1 \cdot \vec{\nabla}_2 \right) + \frac{1}{4\pi\epsilon_0} \left(-\frac{Ze^2}{|\vec{r}_1|} - \frac{Ze^2}{|\vec{r}_2|} + \frac{e^2}{|\vec{r}_1 - \vec{r}_2|} \right) \quad (2.1)$$

with the reduced mass $\mu = m_e M / (m_e + M)$ of the electron mass m_e and the mass of the nucleus M . Due to the electron-electron repulsion term, the Hamiltonian is non-separable and the Schrödinger equation cannot be solved exactly. However, it can be separated in

$$H = H_0 + \eta H_{MP}, \quad (2.2)$$

where H_0 is the dominant nuclear-mass independent term, $\eta = \mu/M$ is the perturbation parameter and

$$H_{MP} = -\frac{\hbar^2}{2m_e} \vec{\nabla}_1 \cdot \vec{\nabla}_2, \quad (2.3)$$

is the mass polarization term.

In NRQED, this problem is solved perturbatively in the following steps: First, a precise representation of the non-relativistic wave function $\Psi(\vec{r}_1, \vec{r}_2)$ must be found, using a variational approach in an appropriate basis set to approximately solve the Schrödinger equation for H_0 . Typically, the Hylleraas basis set is used since it provides a set of functions that are explicitly

¹<https://www.xfel.eu>

correlated [54]. When the wave functions are constructed, perturbation theory is used to evaluate the contributions of the mass polarization term H_{MP} , relativistic and quantum electrodynamic (QED) contributions through an expansion of the level energy in a power series of α [49]

$$E(\alpha, \eta) = E^{(2)} + E^{(4)} + E^{(5)} + E^{(6)} + E^{(7)} + \dots \quad (2.4)$$

where $E^{(n)} \equiv m\alpha^n \mathcal{E}^{(n)}$ is a contribution of order α^n . Each $\mathcal{E}^{(n)}$ is expanded again in a power series of η to

$$\mathcal{E}^{(n)} = \mathcal{E}_0^{(n)} + \eta \mathcal{E}_1^{(n)} + \eta^2 \mathcal{E}_2^{(n)} + \dots \quad (2.5)$$

with the mass-independent contributions $\mathcal{E}_0^{(n)}$ like the non-relativistic energy $\mathcal{E}_0^{(2)}$ and relativistic corrections $\mathcal{E}_0^{(4)}$, and the mass-polarizing terms $\mathcal{E}_{>0}^{(n)}$. In the most recent publication [32], relativistic and QED corrections have been calculated up to the order of α^7 for two-electron systems.

The influence of the nuclear finite-size effect to the level energy is also treated as a perturbation. Therefore, the binding energy of an electron to a nucleus can be written in first order as

$$E = E_p(\alpha, \eta) + E_{\text{fs}} = E_p(\alpha, \eta) + \frac{Ze^2}{6\epsilon_0} \langle r_c^2 \rangle \sum_i \langle \delta^3(\mathbf{r}_i) \rangle, \quad (2.6)$$

with the level energy of the system with a point-like nucleus $E_p(\alpha, \eta)$ and the energy shift due to the finite-size effect E_{fs} . Here, $\langle r_c^2 \rangle$ is the mean-square nuclear charge radius and $\langle \delta^3(\mathbf{r}_i) \rangle$ is the probability density of the i -th electron at the nucleus. For a transition from an initial level i to a final level f with energies E_i and E_f , respectively, it can be written

$$\begin{aligned} \Delta E_{i \rightarrow f} = E_f - E_i &= \Delta E_{p, i \rightarrow f} + \frac{Ze^2}{6\epsilon_0} \langle r_c^2 \rangle \sum_i \Delta \langle \delta^3(\mathbf{r}_i) \rangle_{i \rightarrow f} \\ &= \Delta E_p + F \langle r_c^2 \rangle \end{aligned} \quad (2.7)$$

with the transition frequency for a point-like nucleus ΔE_p and the field-shift factor F . Here, $\Delta \langle \delta^3(\mathbf{r}_i) \rangle_{i \rightarrow f}$ is the difference of the electric probability densities at the nucleus in the levels i and f for the i -th electron. This equation opens the possibility of an all-optical charge radius determination through the measurement of the transition energy $\Delta E_{\text{exp}} = \Delta E_{i \rightarrow f}$ and the calculation of the transition energy ΔE_p for an atom with an idealized point-like nucleus and the field-shift factor F . The charge radius R_c is then given by

$$R_c = \sqrt{\langle r_c^2 \rangle} = \sqrt{\frac{\Delta E_{\text{exp}} - \Delta E_p}{F}}. \quad (2.8)$$

The latest calculated values of ΔE_p and F for the $1s2s\ ^3S_1 \rightarrow 1s2p\ ^3P_J$ transitions of $^{12}\text{C}^{4+}$ are shown in Tab. 2.1. They have been extracted from [32] where the ionization potentials (IP) $E_{\text{IP}}(x)$ of the involved states x and the respective finite nuclear size contribution $\Delta E_{\text{FNS}}(x)$ are given. The latter was calculated for the nuclear charge radius $R_c = 2.407$ from [55]. Therefore, the field-shift factor is given by

$$F = \Delta E_{\text{FNS}}(x) / R_c^2.$$

The transition frequencies ΔE_p can be extracted through

$$\Delta E_p(2p^3P_J) = [E_{\text{IP}}(2p^3P_J) - \Delta E_{\text{FNS}}(2p^3P_J)] - [E_{\text{IP}}(2s^3S_1) - \Delta E_{\text{FNS}}(2s^3S_1)].$$

So far, this method has only been demonstrated in hydrogen [39] and muonic systems [40–42], but is examined for the first time in a He-like system beyond He within this work. The experimental investigation of these transitions in He-like $^{12}\text{C}^{4+}$ requires an ion source capable of populating the $1s2s^3S_1$ state efficiently. This can be expected in the production process in an electron beam ion source.

Table 2.1: Calculated transition energy ΔE_p assuming a point-like nucleus and the corresponding field-shift factor F of the $1s2s^3S_1 \rightarrow 1s2p^3P_J$ transitions of $^{12}\text{C}^{4+}$. The last two rows are the frequency converted values. ΔE_p and F were extracted from [32].

	$1s2s^3S_1 \rightarrow 1s2p^3P_2$	$1s2s^3S_1 \rightarrow 1s2p^3P_1$	$1s2s^3S_1 \rightarrow 1s2p^3P_0$
ΔE_p (eV)	5.45804678(53)	5.4412107(31)	5.4427592(11)
F ($\mu\text{eV}/\text{fm}^2$)	-0.875	-0.875	-0.874
ν_p (GHz)	1319749.83(13)	1315678.89(75)	1316053.32(27)
F (GHz/ fm^2)	0.2115	0.2115	0.2113

2.3 Highly charged ions from electron beam ion sources

Ions with nuclear charge Z and atomic charge q in units of e are often defined as highly charged when they fulfill

$$q > Z/2. \quad (2.9)$$

Due to their unique properties like very high electric fields up to 10^{16} V/m for heavy ions, tens of thousands keV potential energy and their energy level structure, they are of interest in many different fields of physics from tests of QED in strong fields, e.g. in [56–58], optical clocks and fundamental physics [59] or microelectronics to biomedicine research [60, 61].

The production of heavy highly charged ions (HCI) is classically accomplished by stripping off electrons from high energy ions in large accelerator complexes like GSI/FAIR in Darmstadt. Here, the highest charge states of the heaviest elements like U^{92+} can be produced [62]. However, also more compact HCI sources are available in the meantime like laser ion sources [63], electron cyclotron resonance (ECR) [64] ion sources and electron beam ions sources (EBIS) [64]. The latter is particularly interesting for precision experiments since it produces a rather ordered plasma compared to the other sources. A comprehensive introduction and overview about the EBIS technology can be found in [64, 65]. The most important physical effects that happen during the HCI production in an EBIS are briefly summarized in the following.

In an EBIS, neutral atoms are ionized and confined by a magnetically compressed electron beam in combination with an electrostatic trap in axial direction. The balance between charge-state

generation and charge-state destruction is of importance in order to reach a targeted charge state. The differential equations describing the ion production in an EBIS are given by [65]

$$\begin{aligned}
 &\text{ionization} \\
 &\text{to } q = 1 \quad \frac{dn_0}{dt} = -\lambda_1 n_0, \\
 &\quad \vdots \\
 &\text{to } q \quad \frac{dn_q}{dt} = \underbrace{\lambda_q n_{q-1}}_{\text{ion production}} - \underbrace{\lambda_{q+1} n_q}_{\text{ion destruction}} \\
 &\quad \vdots \\
 &\text{to } Z \quad \frac{dn_Z}{dt} = \lambda_Z n_{Z-1},
 \end{aligned} \tag{2.10}$$

with the neutral particle density n_0 and the reaction rate

$$\lambda_q = \sigma_q v_e n_e. \tag{2.11}$$

Here, σ_q is the ionization cross-section, v_e the electron velocity and n_e the electron density. If the ionization process starts only with neutral particles, the boundary conditions

$$t = 0, \quad n_0(0) = n_0^0, \quad n_q(0) = 0$$

lead to the solution [65]

$$\begin{aligned}
 n_0 &= n_0^0 e^{-\lambda_1 t} \\
 n_1 &= \frac{n_0^0 \lambda_1}{\lambda_2 - \lambda_1} (e^{-\lambda_1 t} - e^{-\lambda_2 t}) \\
 n_2 &= n_0^0 \lambda_1 \lambda_2 \left(\frac{e^{-\lambda_1 t}}{(\lambda_2 - \lambda_1)(\lambda_3 - \lambda_1)} + \frac{e^{-\lambda_2 t}}{(\lambda_3 - \lambda_2)(\lambda_1 - \lambda_2)} + \frac{e^{-\lambda_3 t}}{(\lambda_1 - \lambda_3)(\lambda_2 - \lambda_3)} \right) \\
 &\vdots \\
 n_q &= n_0^0 \prod_{l=1}^q \lambda_l \left(\sum_{j=1}^{q+1} \frac{e^{-\lambda_j t}}{\prod_{k=1, k \neq j}^{q+1} (\lambda_k - \lambda_j)} \right).
 \end{aligned} \tag{2.12}$$

Developing the exponents in Eq. (2.12) in a first-order Taylor series yields the more compact solution

$$\begin{aligned}
 n_0 &= n_0^0 (1 - \lambda_1 t) \\
 n_1 &= n_0^0 \lambda_1 t \\
 n_2 &= n_0^0 \lambda_1 \lambda_2 \frac{t^2}{2} \\
 &\vdots \\
 n_q &= n_0^0 \frac{t^q}{q!} \prod_{j=1}^q \lambda_j.
 \end{aligned} \tag{2.13}$$

Under assumption of a step-wise ionization from one charge state to another, the characteristic time τ_q when a charge state q reaches its distribution maximum can be estimated by [64]

$$\begin{aligned}
\tau_1 &= t_1 \\
\tau_2 &= t_1 + t_2 \\
&\vdots \\
\tau_q &= \sum_{k=1}^q t_k
\end{aligned} \tag{2.14}$$

with $t_q = 1/\lambda_q$. This can also be rewritten with Eq. (2.11) in the more usable form

$$j\tau_q = \sum_{k=1}^q \frac{1}{\sigma_k} \tag{2.15}$$

where $j = v_e n_e$ is the electron current density. $j\tau_q$ is called ionization factor and is a fundamental value which determines the maximum achievable charge state. The production of a charge state q is only possible if the ionization factor of the ion source fulfills

$$j\tau_q \geq \sum_{k=1}^q \frac{1}{\sigma_k} \tag{2.16}$$

and if the electron energy is higher than the ionization potential I_q (ideally two to three times of I_q [64]). Figure 2.2 illustrates the necessary ionization factors and electron energies to

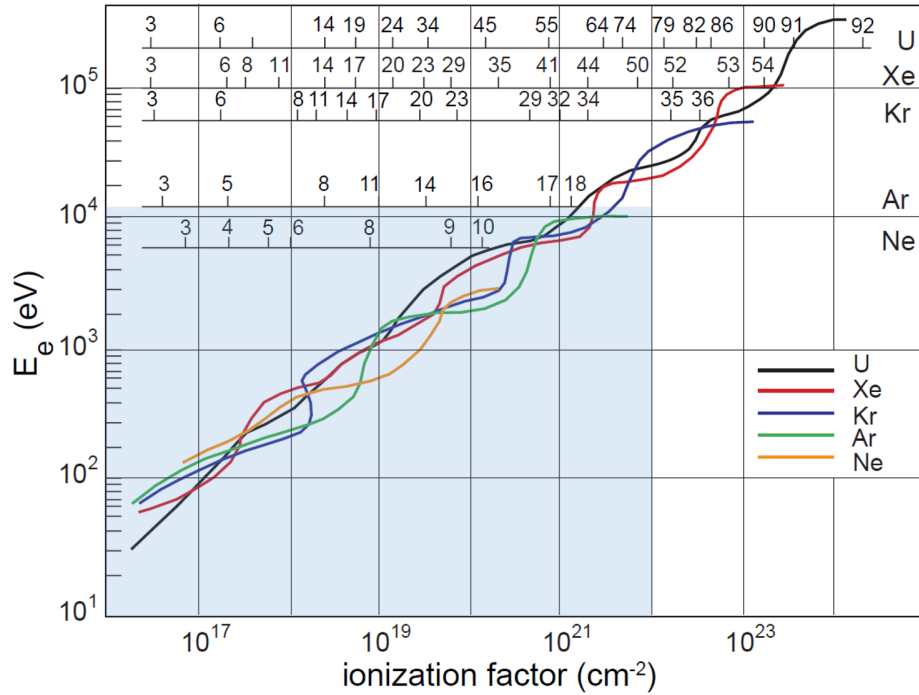


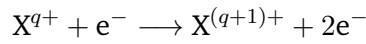
Figure 2.2: Necessary ionization factors and electron energies to achieve a specific charge state of different elements. The blue shaded area marks roughly the working space of the Desden EBIS-A from Dreebit. Taken and modified from [65].

reach a specific charge state of different elements [65]. The blue shaded area marks roughly the working space of the Dresden EBIS-A from Dreebit.

However, Eq. (2.16) is only valid under the idealized assumption that only single-electron impact ionization by electrons is prominent. In reality also other processes like recombination and charge exchange processes are present and influence the ionization factor and with it the maximum charge state. The main processes will be described below followed by a description of the ion confinement and the ion dynamics inside the trap.

2.3.1 Direct Coulomb ionization

The direct coulomb ionization through electron impact



is the main ionizing process in an EBIS. The cross-section for an ionization from charge state q to $q + 1$ by removing an electron from subshell j can be estimated by the Lotz formula [66]

$$\sigma_{qj} = a_{qj} g_{qj} \frac{\ln(E_e/I_{qj})}{E_e I_{qj}} \left\{ 1 - b_{qj} \exp \left[-c_{qj} \left(\frac{E_e}{I_{qj}} - 1 \right) \right] \right\}. \quad (2.17)$$

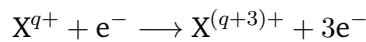
It is important that the electron energy E_e must be greater than the related ionization potential I_{qj} . The constants a_{qj} , b_{qj} and c_{qj} are tabulated values and given by

$$\begin{aligned} a_{qj} &= 4.5 \cdot 10^{-14} \text{ cm}^2 \text{ eV}^2, \\ b_{qj} = c_{qj} &= 0 \end{aligned} \quad (2.18)$$

and g_{qj} is the occupation number of the subshell j of an ion in the charge state q . The total cross-section for an electron impact ionization from q to $q + 1$ is then the sum over all subshells:

$$\sigma_{q \rightarrow q+1}^{\text{EI}}(E_e) = \sum_q \sigma_{qj}(E_e). \quad (2.19)$$

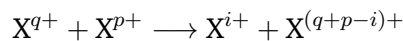
Double ionization



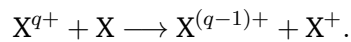
can occur as well but the cross-sections are about one order of magnitude or more lower than for single ionization for most species [65] and is not treated here further.

2.3.2 Charge exchange

Charge exchange (CX) between HCI and neutral atoms is the main loss mechanism in an EBIS due to high cross-section in the order of 10^{-14} to 10^{-15} cm^2 . It often limits the reachable charge state in the electron beam. Generally, it can be written as



and correspondingly for CX with neutral atoms as



The cross-section for CX of k charges between a HCI with charge state q and a colliding ion or atom resulting in a charge state $q - k$ for energies below 25 keV/u can be estimated by the empirical formula [67]

$$\sigma_{q \rightarrow q-k}^{\text{CX}} / \text{cm}^2 \approx A_k \cdot q^{\alpha_k} \cdot (I_q / \text{eV})^{\beta_k} \quad (2.20)$$

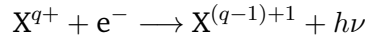
with the ionization potential I_q of the HCI and the tabulated parameters A_k , α_k and β_k , listed in Tab. 2.2.

Table 2.2: Parameters for the cross-section of charge exchange as given by Eq. (2.20). All values are taken from [67].

k	Parameter		
	A_k	α_k	β_k
1	$(1.43 \pm 0.76) \cdot 10^{-12}$	1.17 ± 0.09	-2.76 ± 0.19
2	$(1.08 \pm 0.95) \cdot 10^{-12}$	0.71 ± 0.14	-2.80 ± 0.32
3	$(5.50 \pm 5.80) \cdot 10^{-14}$	2.10 ± 0.24	-2.89 ± 0.39
4	$(3.57 \pm 8.90) \cdot 10^{-16}$	4.20 ± 0.79	-3.03 ± 0.86

2.3.3 Radiative recombination

Another mechanism which leads to the reduction of the ion charge state is the radiative recombination (RR)



where an electron with energy E_e is captured by an ion with the negative electron binding energy E_B and a photon with energy $h\nu = E_e - E_B$ is emitted. The cross-section for RR can be estimated by [68]

$$\sigma_q^{\text{RR}}(E_e) = \frac{8\pi}{3\sqrt{3}} \alpha \lambda_e^2 \chi_q(E_e) \ln \left(1 + \frac{\chi_q(E_e)}{2\hat{n}} \right) \quad (2.21)$$

with

$$\chi_q(E_e) = (Z + q)^2 \frac{I_H}{4E_e}$$

and

$$\hat{n} = n + (1 - W_n) - 0.3.$$

Here, α is the fine structure constant, λ_e is the electron Compton wavelength, $I_H = 13.6$ eV is the ionization potential of hydrogen, E_e is the electron energy, n the principal quantum number of the valence shell and W_n the ratio of unoccupied valence states to the total number of states in the valence shell.

2.3.4 Further processes

Besides the main processes discussed above, in some cases like X-ray spectroscopy of HCI further processes like

- dielectric recombination (DR),
- three-body recombination,
- vacancy cascades and
- photoionization

have to be considered. Since all of these effects have basically no impact to this work, they are not discussed here.

2.3.5 Ion confinement

Ions produced in an EBIS are trapped in axial direction by electrostatic potentials and in radial direction by the space-charge potential of the electron beam and the magnetic field. This is illustrated in Fig. 2.3.

The effective radial trapping potential can be described by [69]

$$V_{\text{rad}}^{\text{eff}}(r) = V_e(r) + \frac{qeB^2r^2}{8m_i} \quad (2.22)$$

with the ion charge state q , the electron charge e , the ion mass m_i and the magnetic field strength B . Assuming an uniform electron beam with radius r_e , the space-charge potential is

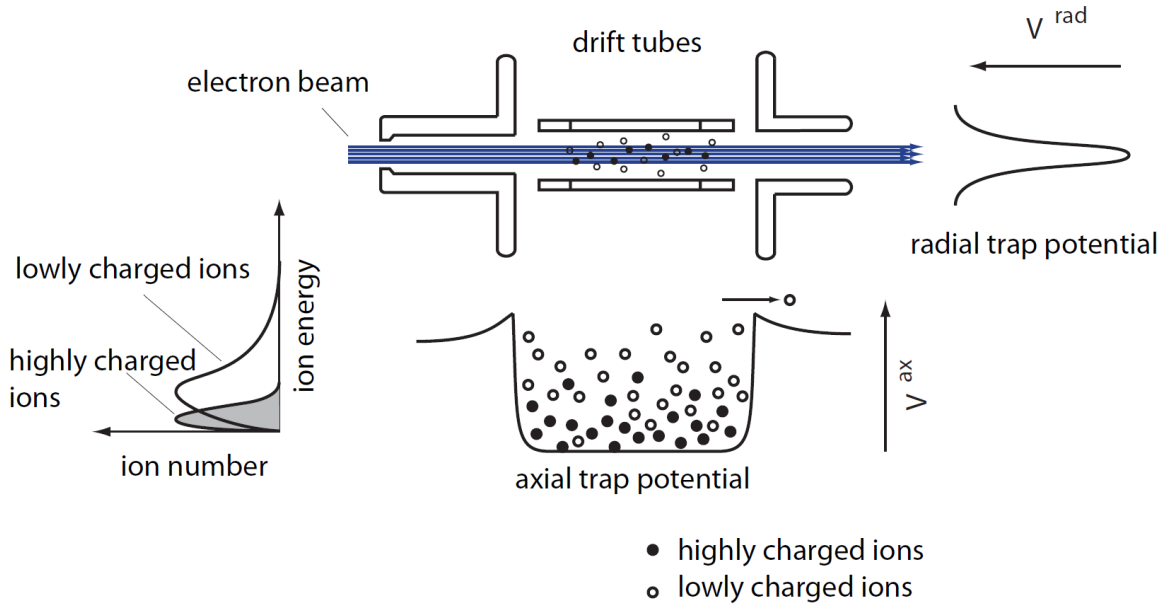


Figure 2.3: Confinement potentials in an electron beam ion source. The radial trap potential is generated by the negative space charge of the electron beam and the axial trap potential is defined by voltages applied to the different drift tube sections. Taken from [65].

given by [69]

$$V_e(r) = \begin{cases} U_e \left(\frac{r}{r_e} \right)^2 & r < r_e \\ U_e \left(2 \ln \frac{r}{r_e} + 1 \right) & r > r_e \end{cases} \quad (2.23)$$

with

$$U_e = \frac{I_e}{4\pi\epsilon_0 v_e} = \frac{1}{4\pi\epsilon_0} \sqrt{\frac{m_e}{2}} \frac{I_e}{\sqrt{E_e}}, \quad (2.24)$$

m_e is the electron mass, I_e is the beam current and E_e is the electron-beam energy. The confinement potential in the axial direction is generated by voltages applied to the different drift tube sections.

The electric trap capacity C_{el} is a measure for the maximum number of trappable ions in an EBIS. Under the assumption of a homogeneous electron beam with current I_e and electron energy E_e passing through a trap of length L , the trap capacity is given by [65]

$$C_{el} = 1.05 \cdot 10^{13} \frac{I_e/A \cdot L/m}{\sqrt{E_e/\text{eV}}}. \quad (2.25)$$

The real number of stored ions will be below C_{el} as the positive charge of the trapped ions partly screens the electron space charge which leads to compensation of the radial trap depth and with it to increased ion losses.

2.3.6 Ion-energy distribution and ion heating

Through elastic ion-ion collisions inside the trap, a Boltzmann distribution (Boltzmann constant k_B) of the ion energy corresponding to a temperature T_i [65]

$$f(E_i) = \frac{2}{\sqrt{\pi} k_B T_i} \sqrt{\frac{E_i}{k_B T_i}} \exp\left(-\frac{E_i}{k_B T_i}\right) \quad (2.26)$$

is formed within milliseconds. As a consequence, for a specific mean ion energy, there are always ions which have more energy than the critical energy

$$E_c = eq_i \cdot \Delta U_{\text{trap}}$$

and can surpass the trap barrier ΔU_{trap} . As E_c depends on the ion charge state q_i , lowly charged ions will leave the trap earlier than highly charged ions.

The ion cloud is constantly heated through elastic electron-ion collisions. A δ -distribution for the electron velocity v_e is assumed. If v_e is much larger than the ion velocity v_i , the heating rate of the ion cloud can be estimated by [69]

$$\left[\frac{d}{dt} (n_i k_B T_i) \right]^{\text{heating}} \approx \frac{2}{3} n_i n_e Y \frac{m_e}{m_i} \frac{m_e}{v_e}, \quad (2.27)$$

with

$$Y = 4\pi \left(\frac{q_i e^2}{m_e} \right)^2 \ln \Lambda_{ei}.$$

Here, n_i is the mean ion density in charge state q_i , n_e the electron beam density and $\ln \Lambda_{ei}$ is the Coulomb logarithm for electron-ion collisions [70].

2.3.7 Energy exchange between ions

Besides electron-ion collisions, also elastic ion-ion collisions happen in the ion cloud. Here, energetic 'hot' ions are cooled by colder ions. The energy gain of the i -th ionic species through energy exchange with ions of the j th ionic species can be described by [69]

$$\left[\frac{d}{dt} (n_i k_B T_i)_j \right]^{\text{exchange}} = 2\nu_{ij} n_i \frac{m_i}{m_j} \frac{k_B (T_j - T_i)}{\left(1 + \frac{m_i T_j}{m_j T_i} \right)^{3/2}} \quad (2.28)$$

with the Coulomb collision rate

$$\nu_{ij} = \frac{4}{3} \frac{\sqrt{2\pi} n_j}{(4\pi\epsilon_0)^2} \left(\frac{q_i q_j e^2}{m_i} \right)^2 \left(\frac{m_i}{k_B T_i} \right)^{3/2} \ln \Lambda_{ij}.$$

Here, $\ln \Lambda_{ij}$ is the Coulomb logarithm for ion-ion collisions.

2.3.8 Ion losses and evaporative cooling

As mentioned above, ions in charge state q_i with an energy more than $E_c = eq_i \cdot \Delta U_{\text{trap}}$ can leave the trap. The ion escape rate can be obtained from an approximate solution of the Fokker-Planck equation as [69]

$$\frac{dn_i}{dt} = -n_i \nu_i \left(\frac{e^{-\omega_i}}{\omega_i} - \sqrt{\omega_i} (\text{erf}(\omega_i) - 1) \right) \quad (2.29)$$

with

$$\omega_i = \frac{eq_i \Delta U_{\text{trap}}}{k_B T_i}$$

and the total Coulomb collision rate of the i -th ion species

$$\nu_i = \sum_j \nu_{ij}.$$

When ions are lost from the trap, energy is removed as well from the trap. This leads to a cooling of the remaining ions. This energy loss can be described by [69]

$$\left[\frac{d}{dt} (n_i k_B T_i) \right]^{\text{esc}} = - \left(\frac{2}{3} n_i \nu_i e^{-\omega_i} - \frac{dn_i}{dt} \right) k_B T_i \quad (2.30)$$

and is referred to as evaporative cooling. This effect can be increased by feeding lowly charged ions into the trap or by increasing the gas pressure inside the EBIS to use it as source for lowly charged ions. Since E_c depends on the ion charge, lowly charged ions can leave the trap earlier and by that cool the remaining ions. However, if the gas pressure is chosen too high, the production of HCI will be strongly limited by charge exchange. An alternative to increase evaporative cooling is by lowering the electrostatic trap potential which leads to an increased ion loss which cools the ion cloud. If the trap potential is chosen too small, this will again hinder the production of HCI.

2.3.9 Balance equation for the ion charge state distribution

The time-dependent evolution of ion densities n_q of the different charge states q is given by [69]

$$\begin{aligned} \frac{dn_q}{dt} = & R_{q-1 \rightarrow q}^{\text{EI}} - R_{q \rightarrow q+1}^{\text{EI}} + R_{q+1 \rightarrow q}^{\text{RR}} - R_{q \rightarrow q-1}^{\text{RR}} \\ & + R_{q+1 \rightarrow q}^{\text{CX}} - R_{q \rightarrow q-1}^{\text{CX}} - R_q^{\text{axesc}} - R_q^{\text{radesc}} + R_q^{\text{source}}. \end{aligned} \quad (2.31)$$

and consists of the different charge creation or destruction rates. The effective ionization rate is given by [69]

$$R_{q \rightarrow q+1}^{\text{EI}} = \frac{j_e}{e} n_q \sigma_{q \rightarrow q+1}^{\text{EI}}(E_e) f(r_e, r_q) \quad (2.32)$$

with the electron current density j_e , the ionization cross-section $\sigma_{q \rightarrow q+1}^{\text{EI}}(E_e)$ and a factor $f(r_e, r_q)$ which takes the overlap between the electron beam with radius r_e and the ion density distribution with radius r_q into account. The effective radiative-recombination rate is given similarly by

$$R_{q \rightarrow q-1}^{\text{RR}} = \frac{j_e}{e} n_q \sigma_{q \rightarrow q-1}^{\text{RR}}(E_e) f(r_e, r_q). \quad (2.33)$$

In thermal equilibrium, the charge-exchange rate is given by

$$R_{q \rightarrow q-1}^{\text{CX}} = n_0 n_q \sigma_{q \rightarrow q-1}^{\text{CX}} \bar{v}_q \quad (2.34)$$

with the mean ion velocity

$$\bar{v}_q = \sqrt{\frac{8k_B T_q}{\pi m_q}}.$$

The ion loss rate is given by Eq. (2.29) for the axial direction (R_q^{axesc}) and for the radial direction (R_q^{radesc}). In the latter case, ΔU_{trap} is defined by the radial potential from Eq. (2.22). The source term in case of a continuous injection of neutral gas is given by

$$R_1^{\text{source}} = \frac{j_e}{e} n_0 \sigma_{0 \rightarrow 1}^{\text{EI}} \quad R_{q>1}^{\text{source}} = 0. \quad (2.35)$$

The evolution of the ion temperatures is described by [69]

$$\begin{aligned} \frac{d}{dt} (n_q k_B T_q) = & \left[\frac{d}{dt} (n_q k_B T_q) \right]^{\text{heating}} + \sum_j \left[\frac{d}{dt} (n_q k_B T_q) \right]_j^{\text{exchange}} \\ & - \left[\frac{d}{dt} (n_q k_B T_q) \right]^{\text{axesc}} - \left[\frac{d}{dt} (n_q k_B T_q) \right]^{\text{radesc}}. \end{aligned} \quad (2.36)$$

The energy change through heating and energy exchange is given by Eq. (2.27) and (2.28), respectively. The energy loss from ion escape is given by Eq. (2.30) for the respective axial and radial potential.

2.3.10 EBIS simulations

Eq. (2.31) and (2.36) can be solved together with the corresponding cross-sections and EBIS parameters to estimate the charge state and temperature evolution, respectively. A dedicated Python 3 package is available with *ebisim*². It uses input like geometrical properties, electron current and energy, axial trap depth and gas pressure to numerically solve the rate equations for discrete time steps. Figure 2.4 shows the result of a carbon simulation with typical EBIS-A parameters from $t_{\text{breed}} = 0.1 \text{ ms}$ to $t_{\text{breed}} = 1 \text{ s}$ on a logarithmic time axis.

The top panel illustrates the charge-state evolution as relative abundance of the different states over time. The maximum abundance of C^{4+} (pink line) is predicted between 15 ms and 40 ms indicated by the blue shaded area. The corresponding plasma temperature evolution is depicted in the bottom panel. Although all charge states start with different temperatures, they are quickly thermalized after 1 ms through ion-ion collisions. The simulation for this parameter set estimates a C^{4+} temperature of roughly 7 eV which strongly depends on the electron current since electron-ion collisions are the main heating source. By decreasing the electron current to 30 mA, also the temperature is reduced to 2.5 eV at the expense of reduced C^{4+} yield by roughly the same factor.

The middle plot shows the evolution of the electron ionization rate $R_{3+ \rightarrow 4+}^{\text{EI}}$ (black dashed line), the charge exchange rate $R_{5+ \rightarrow 4+}^{\text{CX}}$ (red dashed line) and the radiative recombination rate $R_{5+ \rightarrow 4+}^{\text{RR}}$ (blue dashed line) which reflect the production of C^{4+} . In the relevant time window, the EI rate and CX rate start to become comparable whereas the RR rate is many orders of magnitude smaller.

The population of the $1s2s\ ^3\text{S}_1$ state in C^{4+} is driven by CX, RR and electron impact excitation (EIE). RR can be neglected as well as EIE since the cross-section of EIE is also some orders of magnitude smaller than electron ionization for electron energies around 12 keV [71]. Thus, the metastable $1s2s\ ^3\text{S}_1$ state is efficiently populated only by charge exchange from C^{5+} to C^{4+} . The fraction of $R_{5+ \rightarrow 4+}^{\text{CX}}$ to the sum of all process rates leading to C^{4+} without losses is plotted in orange in the middle panel of Fig. 2.4. It is 5 % to 15 % between 15 ms and 40 ms. Together with the probability of ≈ 0.75 for a C^{4+} ion to end up in a triplet state, the population of the triplet ground-state can be estimated from 3.75 % to 11.25 %. The curve suggests an even larger population for breeding times of 1 s. However, the absolute number of C^{4+} ions will be lower for long breeding times due to the shift of the charge state distribution which compensates the larger $1s2s\ ^3\text{S}_1$ state population. Summarized, a slightly longer breeding time than 15 ms until the maximum yield of C^{4+} is reached might be preferable.

²<https://github.com/ebisim/ebisim>

$I_e = 80 \text{ mA}$, $E_e = 12.7 \text{ keV}$, $\Delta U_{\text{trap}} = 140 \text{ V}$, $p_{\text{gas}} = 6\text{E-}8 \text{ mbar}$

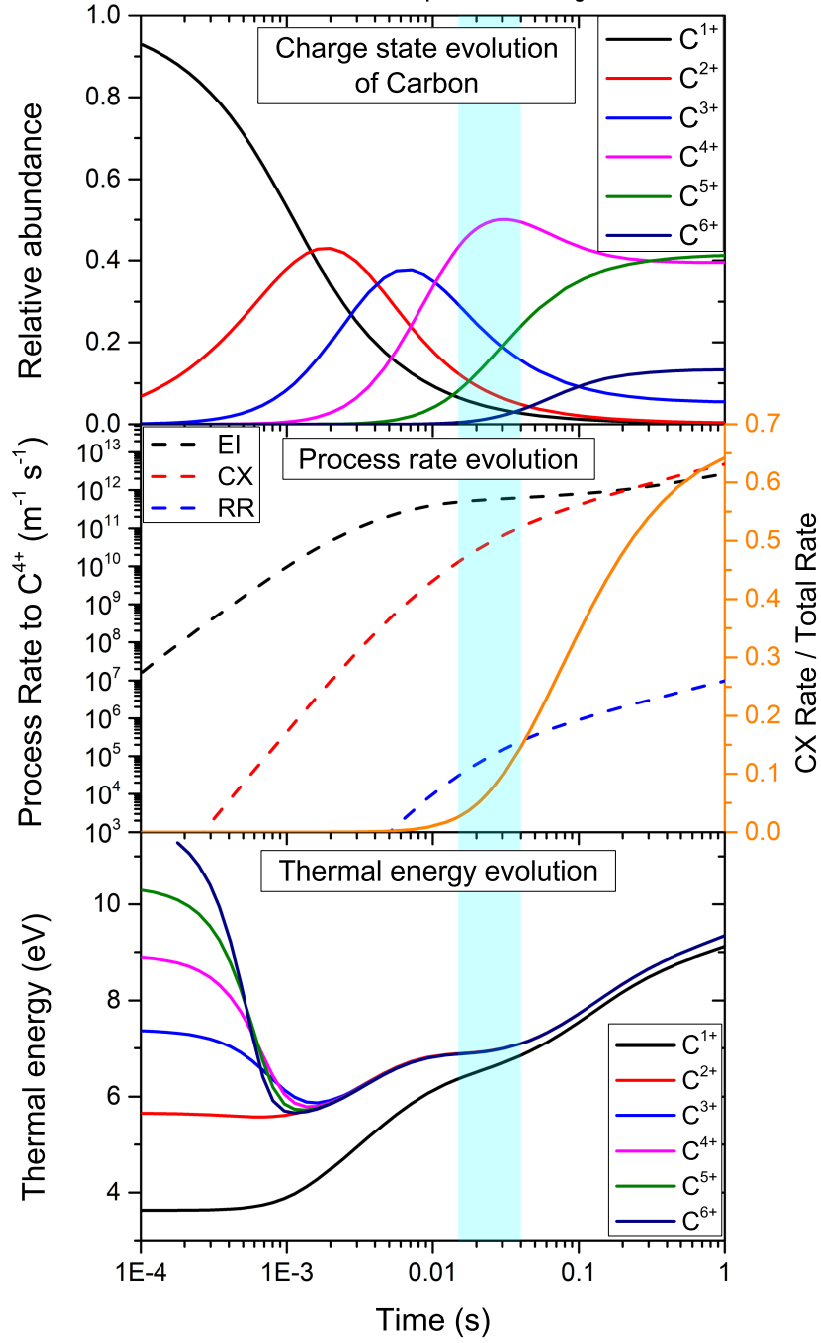


Figure 2.4: Simulation of relative abundances (top), process rates leading to the production of C^{4+} (middle) and the temperature evolution (bottom) for typical EBIS parameters with the Python package *ebisim*.

2.4 Collinear laser spectroscopy

Collinear laser spectroscopy (CLS) has been developed for more than four decades to perform laser spectroscopy with short-lived radioactive nuclei [72–74]. CLS combines high sensitivity and a fast measurement cycle which is necessary to investigate short-lived isotopes and can be used to extract nuclear ground-state properties like the nuclear spin, magnetic dipole moments and electric quadrupole moments.

Ions with charge state q and mass m produced from any source are accelerated by an electrostatic potential of typically $U = 10 - 60$ kV and transported through electrostatic deflection to an optical detection region (ODR) within a few μs . Here, the ion beam is superposed with a collinear (c) or anticollinear (a) laser beam. When the laser frequency in the ions rest frame coincides with the transition frequency ν_0 , that is defined as

$$\nu_0 = \frac{E_2 - E_1}{h}$$

between a populated lower state at energy E_1 and an excited state at energy E_2 , the resulting fluorescence light can be detected perpendicular to the beam direction.

A useful side effect of the electrostatic acceleration is the compression of the initial longitudinal velocity distribution. Since the energy spread δE remains constant during an electrostatic acceleration and [74]

$$\delta E = \delta \left(\frac{1}{2} m v^2 \right) = m v \delta v = \text{const.},$$

the velocity spread δv has to decrease if the velocity v of the ions is increased. Thereby, the optical Doppler broadening is strongly reduced and an observed linewidth in the order of the natural linewidth can be achieved.

Another consequence of the fast-moving ions is the shift of the rest-frame transition frequency ν_0 to ν_L in the laboratory-frame due to the relativistic Doppler effect. The shift is given by

$$\nu_L = \nu_0 \gamma (1 + \beta \cos \alpha) \quad (2.37)$$

with the Lorentz factor $\gamma = (1 - \beta^2)^{-1/2}$, the velocity $\beta = v/c$ and the angle between laser and ion beam α . In case of a collinear (c, $\alpha = 0$) or anticollinear (a, $\alpha = \pi$) geometry, the equation is reduced to

$$\nu_{c/a} = \nu_0 \gamma (1 \pm \beta). \quad (2.38)$$

This enables the possibility to change the ion velocity β instead of scanning the laser frequency to excite the ions which is often faster and more convenient. It is typically realized by applying a tunable voltage to the floated optical detection region (ODR) and is referred to as Doppler-tuning.

To extract the rest-frame transition frequency ν_0 from the measured laboratory-frame frequency $\nu_{c/a}$, the ion velocity $v = \sqrt{2qeU/m}$ must be known. However, the starting potential U is often known only to few V due to unknown voltage gradients and contact potentials inside the source. This restricts the achievable precision in ν_0 . This is particularly problematic in plasma ion sources like an ECR or an EBIS.

Alternatively, the laboratory-frame frequency is measured in collinear and anticollinear geometry for the same ion velocity β . Then, the rest-frame transition frequency can be extracted through

$$\nu_c \nu_a = \nu_0^2 \gamma^2 (1 + \beta)(1 - \beta) = \nu_0^2 \frac{1}{1 - \beta^2} (1 - \beta^2) = \nu_0^2. \quad (2.39)$$

To ensure the same β in both directions, the measurements should be carried out in fast iterations which is then referred to as quasi-simultaneous collinear and anticollinear laser spectroscopy. When Doppler-tuning is used, the laser frequencies must be chosen in a way that the resonance appears at the same scan voltage $U_{c/a}$ for both directions, which is experimentally difficult to realize. However, a systematic shift of ν_0 originating from a small remaining voltage difference $\delta U = U_a - U_c$ can be corrected by the following adaption of Eq. (2.39)

$$\nu_0 = \sqrt{\left(\nu_c - \frac{\partial \nu_c}{\partial U} \cdot \delta U \right) \cdot \nu_a}. \quad (2.40)$$

The differential Doppler shift $\frac{\partial \nu_c}{\partial U}$ is given by [75]

$$\frac{\partial \nu_c}{\partial U} = \frac{\nu_0}{mc^2} \left(q \cdot e + \frac{q \cdot e (mc^2 + q \cdot eU)}{\sqrt{q \cdot eU (2mc^2 + q \cdot eU)}} \right). \quad (2.41)$$

2.4.1 Laser beam alignment

The determination of ν_0 through Eq. (2.39 – 2.41) assumes that both laser beams probe the same ion velocity β . This does not hold if an angle α_{IL} between ion and laser beam and an angle α_{LL} between both laser beams is introduced. The resulting shift between the measured rest-frame frequency $\nu_{0, \text{meas}}$ and ν_0 can be estimated for the "worst-case" with

$$\begin{aligned} \delta \nu_{\text{angle}}(\alpha_{IL}, \alpha_{LL}) &= \nu_0 - \nu_{0, \text{meas}} \\ &= \nu_0 - \sqrt{\nu_c \nu_a} \\ &= \nu_0 - \sqrt{\nu_0^2 \gamma^2 (1 + \beta \cdot \cos(\alpha_{IL} + \alpha_{LL}))(1 - \beta \cdot \cos \alpha_{IL})}. \end{aligned} \quad (2.42)$$

Fig. 2.5 illustrates $\delta \nu_{\text{angle}}(\alpha_{IL}, \alpha_{LL})$ for a $^{12}\text{C}^{4+}$ ion beam with a kinetic energy per charge q of $E_{\text{kin}} = 10.5 \text{ keV}/q$, the roughly known $1s2s\ ^3\text{S}_1 \rightarrow 1s2p\ ^3\text{P}_2$ transition frequency and typical angles in CLS. When at least two of the three beams are perfectly aligned, a small angle of the third beam is negligible. However, the superposition of the two laser beams is critical since laser angles in the μrad regime already increase the sensitivity to a laser-ion angle significantly.

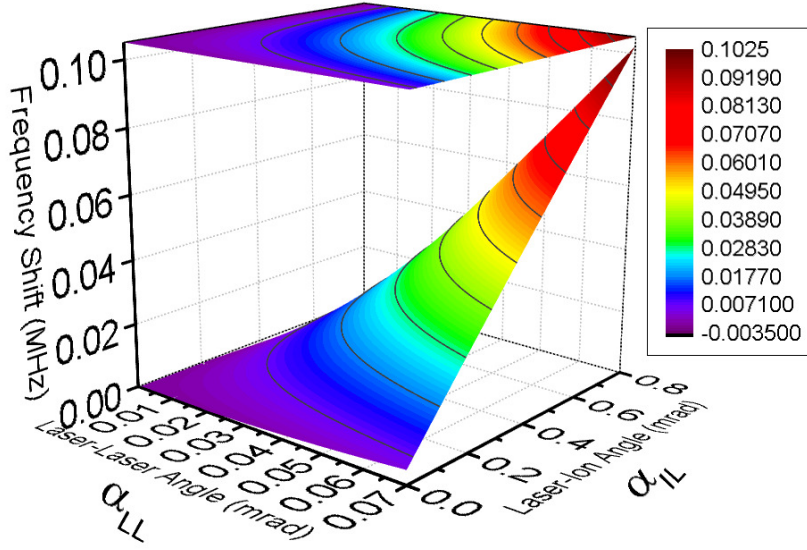


Figure 2.5: Surface plot and its projection of the frequency shift $\delta\nu_{\text{angle}}(\alpha_{\text{IL}}, \alpha_{\text{LL}})$ for various laser-ion beam angles α_{IL} and laser-laser beam angles α_{LL} for a $^{12}\text{C}^{4+}$ ion beam with a kinetic energy per charge q of $E_{\text{kin}} = 10.5 \text{ keV}/q$.

2.4.2 Line shape

An ion with a transition between two energy levels $E_2 - E_1 = h\nu_0$ inside a laser beam with a spectral frequency ν and an intensity I can be described by the model of a damped harmonic oscillator [76]. The line profile of the transition is then given by the area-normalized Lorentzian function

$$L(\nu) d\nu = \frac{1}{\pi} \frac{\Gamma/2}{(\nu - \nu_0)^2 + (\Gamma/2)^2} d\nu \quad (2.43)$$

with the full-width at half maximum (FWHM) Γ . The smallest possible linewidth is the natural linewidth Γ_{nat} that is linked to the lifetime τ of the excited state (assuming that the lower state has a considerably longer lifetime) and the Einstein coefficient of spontaneous decay A_{21} by

$$\Gamma_{\text{nat}} = \frac{A_{21}}{2\pi} = \frac{1}{2\pi\tau}. \quad (2.44)$$

When the laser intensity I reaches the saturation intensity

$$I_{\text{sat}} = \frac{\pi h \nu_0^3}{3c^2 \tau}, \quad (2.45)$$

the induced emission rate becomes equal to the spontaneous decay rate and the lifetime τ of the excited state is shortened. This increases the Lorentzian linewidth by

$$\Gamma = \Gamma_{\text{nat}} \sqrt{1 + \frac{I}{I_{\text{sat}}}} \quad (2.46)$$

and is called power broadening.

In case of an ensemble of ions that has a velocity distribution described by the Maxwell-Boltzmann-distribution with temperature T , the laser frequency ν is differently Doppler shifted in the rest-frame of each ion depending on its individual velocity. The line profile purely from this so-called Doppler broadening (DB) is given by an area-normalized Gaussian profile

$$G(\nu) = \sqrt{\frac{mc^2}{2\pi k_B T}} \exp\left(-\frac{mc^2}{2k_B T} \left(\frac{\nu - \nu_0}{\nu_0}\right)^2\right) = \frac{1}{\sigma\sqrt{2\pi}} \exp\left(-\frac{(\nu - \nu_0)^2}{2\sigma^2}\right) \quad (2.47)$$

with the FWHM

$$\delta\nu_{\text{DB}} = \sigma\sqrt{8\ln 2} = \frac{\nu_0}{c} \sqrt{\frac{8k_B T \ln 2}{m}}. \quad (2.48)$$

When the ensemble with charge q is accelerated with an electrostatic voltage U like in CLS, the FWHM is compressed in beam direction by the factor [77]

$$R = \sqrt{\frac{k_B T}{qeU}}. \quad (2.49)$$

The full line profile of a transition in a Doppler broadened ionic ensemble is now described by the convolution of Lorentzian and Gaussian profile given by

$$V(\nu) = \int L(\nu') G(\nu - \nu') d\nu'. \quad (2.50)$$

The convolution has no closed analytical expression but it can be related to the real part of the Faddeeva function $\omega(z)$ by

$$V(\nu, \sigma, \gamma = \Gamma/2) = \frac{\text{Re}[\omega(z)]}{\sigma\sqrt{2\pi}} \quad (2.51)$$

with

$$z = \frac{\nu + i\gamma}{\sigma\sqrt{2}}.$$

2.4.3 Photon recoil

A photon carries a momentum $p_\gamma = h\nu_L/c$ additional to its energy $E = h\nu_L$. Energy and momentum are conserved during absorption and emission processes in an ion. This means that a part of the photon energy is added to the kinetic energy of the ion instead of the internal transition energy $\Delta E = h\nu_0$ which results in slightly higher measured resonance frequencies ν_L than ν_0 . Therefore, Eq. (2.40) must be corrected by the recoil frequency $\delta\nu_{\text{rec}}$ for comparison with *ab initio* calculations that calculate the difference of level energies. The corresponding correction can be derived in the ion's rest-frame ($p_{\text{ion}} = 0$, $E_{\text{kin}} = 0$) with the conservation of momentum

$$\begin{aligned} p'_{\text{ion}} &= p_{\text{ion}} + p_\gamma \\ mv &= \frac{h\nu_L}{c} \end{aligned} \quad (2.52)$$

and energy

$$\begin{aligned} E'_{\text{kin}} + \Delta E &= E_{\text{kin}} + E_{\gamma} = E_{\gamma} \\ \frac{m}{2}v^2 + h\nu_0 &= h\nu_{\text{L}}, \end{aligned} \quad (2.53)$$

yielding

$$\delta\nu_{\text{rec}} = \nu_{\text{L}} - \nu_0 = \frac{(mv)^2}{2mh} = \frac{h\nu_{\text{L}}^2}{2mc^2} \approx \frac{h\nu_0^2}{2mc^2} \approx \frac{h(\nu_{\text{c}} + \nu_{\text{a}})^2}{8mc^2}. \quad (2.54)$$

for a collinear and anticollinear laser. The complete equation for the rest-frame frequency determination from collinear and anticollinear laser spectroscopy is then given by

$$\nu_0 = \sqrt{\left(\nu_{\text{c}} - \frac{\partial\nu_{\text{c}}}{\partial U} \cdot \delta U\right) \cdot \nu_{\text{a}} - \delta\nu_{\text{rec}}}. \quad (2.55)$$

if the measured transition frequency is to be compared with frequencies theoretically obtained for level energies $E_2 - E_1$.

Another consequence of the photon momentum transfer to the ion in CLS is the acceleration and deceleration of ions in a collinear or anticollinear laser beam, respectively. Since the spontaneous decay emits a photon in any direction with the same probability, the ion's velocity is changed on average by $\delta v = h\nu_{\text{L}}/mc$ in the direction of the laser. This shifts the resonance frequency in the laboratory-frame for both directions by

$$\delta\nu = \frac{\partial\nu_{\text{c/a}}}{\partial v} \cdot \delta v = \nu_0 \left((c - v) \sqrt{1 - \frac{v^2}{c^2}} \right)^{-1} \cdot \delta v \quad (2.56)$$

towards higher frequencies and therefore a systematic shift occurs if more than one photon is scattered. For typical ion velocities v and laboratory laser frequencies ν_{L} in this work, the mean shift of the laboratory-frame resonance frequency per excitation and emission cycle is $\delta\nu \approx 0.65$ MHz.

The mean number of scattered photons during an interaction time t can be estimated through

$$\bar{n}_{\text{sc}} = R_{\text{sc}} \cdot t \quad (2.57)$$

with the scattering rate [78]

$$R_{\text{sc}}(\nu) = \frac{I/I_0 \cdot A_{\text{ik}}/2}{1 + I/I_0 + (4\pi(\nu - \nu_0)/A_{\text{ik}})^2}. \quad (2.58)$$

The saturation intensity in the $1s2s\ ^3\text{S}_1 \rightarrow 1s2p\ ^3\text{P}_J$ transitions of C^{4+} is roughly $I_{\text{sat}} = 1.01$ mW/mm².

2.4.4 Zeeman effect

In presence of a magnetic field B , the degeneracy of the magnetic sub-states m_J is lifted by an additional energy shift [79]

$$\Delta E_{\text{Zeeman}} = g_J m_J \mu_{\text{B}} B \quad (2.59)$$

with the Bohr magneton $\mu_B = e\hbar/(2m_e)$ and the Landé factor

$$g_J = 1 + \frac{J(J+1) - L(L+1) + S(S+1)}{2J(J+1)}.$$

The Zeeman splitting of the first triplet states in $^{12}\text{C}^{4+}$ is illustrated in Fig. 2.6 and can lead to systematic shifts in the determination of ν_0 when circular polarized light is used and the different transitions are not resolved. This is usually the case for weak magnetic fields like the geomagnetic field. Therefore, the average of the different magnetic shifts affects the determination of ν_0 . The strongest shift arises in the $1s2s\ ^3S_1 \rightarrow 1s2p\ ^3P_0$ transition with $\Delta E_{P0} = \pm 2\mu_B B$ for σ^\pm light. The $1s2s\ ^3S_1 \rightarrow 1s2p\ ^3P_1$ transition is shifted by $\Delta E_{P1} = \pm 1.75\mu_B B$ and the $1s2s\ ^3S_1 \rightarrow 1s2p\ ^3P_2$ transition is shifted by $\Delta E_{P2} = \pm 1.5\mu_B B$. Linear polarized light does not introduce any shift but the line profile is broadened.

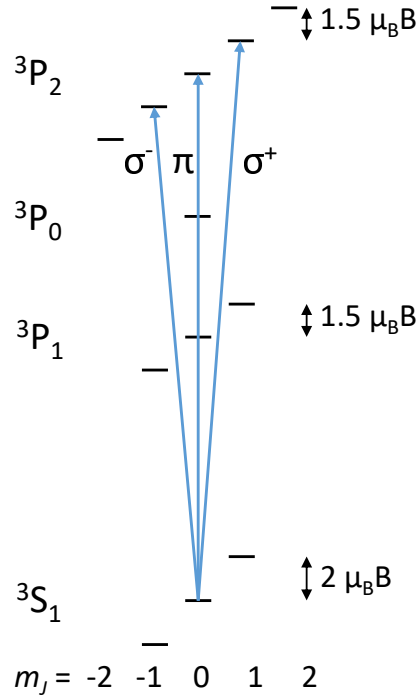


Figure 2.6: Zeeman splitting of the $^{12}\text{C}^{4+}$ fine structure.

3 The COALA setup

The Collinear Apparatus for Laser Spectroscopy and Appplied Science (COALA), situated at the Institute for Nuclear Physics at the Technical University Darmstadt, has originally been designed for high-voltage evaluations through collinear laser spectroscopy (CLS) [81, 82]. In preparation for the measurements that reached the ppm-accuracy level, the apparatus has been characterized in detail and the cornerstone for high-precision CLS has been set. This resulted in accurate rest-frame transition frequency measurements in Ba^+ and Ca^+ exploring and resolving a puzzling behavior in the atomic structure of earth-alkaline elements [83, 84]. Another part of COALA is the assistance of online experiments investigating exotic nuclei with atomic reference values which improve the extraction of nuclear parameters like the nuclear charge radius [85]. Furthermore, new ion-sources and CLS techniques have been developed at COALA. For example, different schemes of laser ablation sources have been tested [86]. One of these will be used at Argonne National Laboratory as offline ion source in upcoming experiments. Additionally, a new versatile buffer gas-cooled laser ablation source with a combined RF-funnel ion guide system has been constructed and successfully commissioned with Ti^+ ions at COALA [87, 88]. Also a technique for the creation of a neutral boron beam by photo-detachment of negative B^- ions has successfully been demonstrated [89].

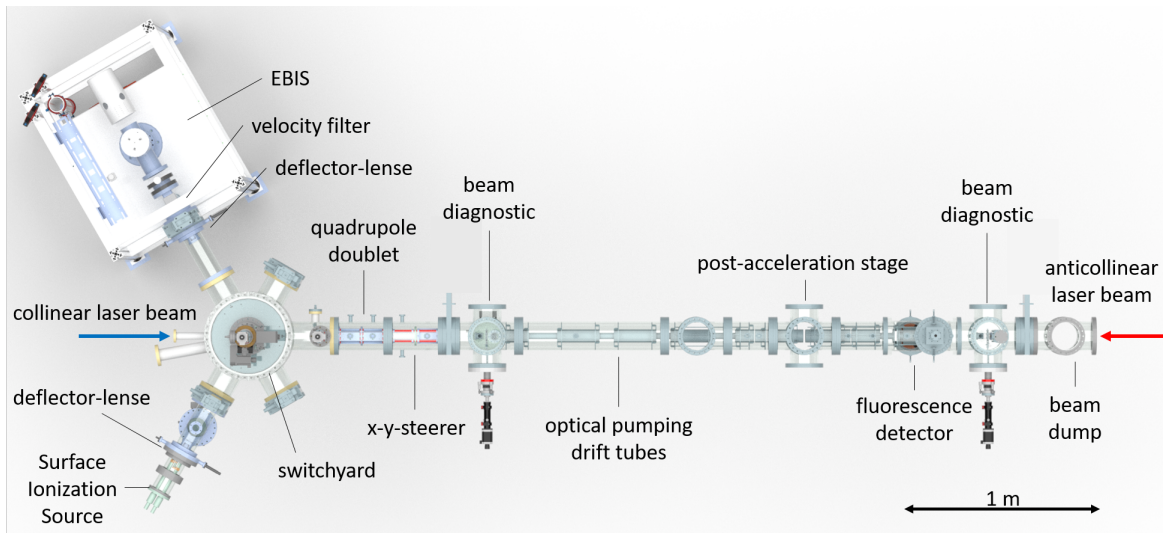


Figure 3.1: Overview of the COALA beamline. Main differences of the nearly 7-m long beamline to the previous version detailed in [80] are the electron beam ion source (EBIS) with an attached velocity filter, the switchyard and changes in the beam diagnostic.

The COALA setup consists of a nearly 7-m long beamline that is shown in Fig. 3.1 and discussed in detail in [80, 82]. For the investigation of highly charged ions, a new electron beam ion source (EBIS) and velocity filter from DREEBIT were installed. This required a new switchyard and an upgrade of the beam diagnostic stations which were designed and commissioned within this work. These are described separately in the following sections.

Ions exiting the EBIS velocity filter are collimated and steered with a commercial deflector-lens from DREEBIT into the the switchyard and are deflected into the main section of the beamline. A quadrupole doublet and another x-y-steerer are used to optimize the ion beam shape and to align the beam to the laser beam axis which is defined by two iris diaphragms 2.6 m apart in the beam diagnostic chambers. The optical pumping section and post-acceleration stage, which are instrumental in high-voltage measurements, were not used in this work. Details for these parts can be found in [82]. The fluorescence light of the ions is detected in the optical detection region (ODR) that is described in [31, 90]. It consists of two elliptical mirrors (ODR1 and ODR2) that can be floated internally to apply Doppler-tuning (see Sec. 2.4). The mirror in ODR2 has been upgraded with MIRO 3 coating which has a high UV reflectivity of $> 90\%$, improving the light collection compared to the polished aluminum mirror in ODR1. Furthermore, the compound parabolic concentrators (CPC) have been removed and instead two photomultiplier tubes (PMT) per elliptical mirror have been installed which increased the total number of PMTs from 2 to 4. Thereby even more fluorescence light can be collected on cost of an acceptably higher laser background rate. After the second beam diagnostic, the ion beam is dumped onto an off-axis Faraday cup with a steerer.

3.1 Dresden EBIS-A

The Dresden EBIS-A is a room-temperature electron beam ion source and commercially available from DREEBIT GmbH. It produces highly charged ions through electron impact ionization as explained in Sec. 2.3. A schematic illustration of the EBIS and the applied voltages are depicted in Fig. 3.2 together with a picture of the EBIS at COALA.

An iridium-cerium cathode generates an electron beam of up to 120 mA which is subsequently accelerated into three drift tubes forming the ion trap. Afterwards, the electron beam is repelled by a negative voltage $U_{\text{Rep}} < U_C$ and guided onto a water cooled electron collector. The necessary electron beam compression is accomplished by an axially symmetric magnetic field created and formed by two NbFeB permanent magnet rings and soft iron parts producing an on-axis magnetic field strength of ≈ 620 mT. Thereby ionization factors of $j\tau > 10^{22} \text{ 1/cm}^2$ are reached in the central drift tube which has an effective length of 60 mm and an inner diameter of 5 mm. Positive ions produced in this section at potential U_A are axially trapped by the voltages U_0 and U_{B1} applied to the first and third drift tube, respectively. The radial ion trap is formed by the negative space charge of the electron beam. In order to extract the ions after a charge breeding time t_{breed} , the third drift tube is lowered to $U_{B2} \leq U_A$ within a few μs . Alternatively, U_{B1} can be decreased with respect to U_0 ($U_A < U_{B1} < U_0$) and held statically to extract a continuous beam of leaking ions.

The easiest way feeding the EBIS with the element of interest is through leakage of a gaseous sample into the drift tube section. For the production of C^{4+} propane gas (C_3H_8) was used.

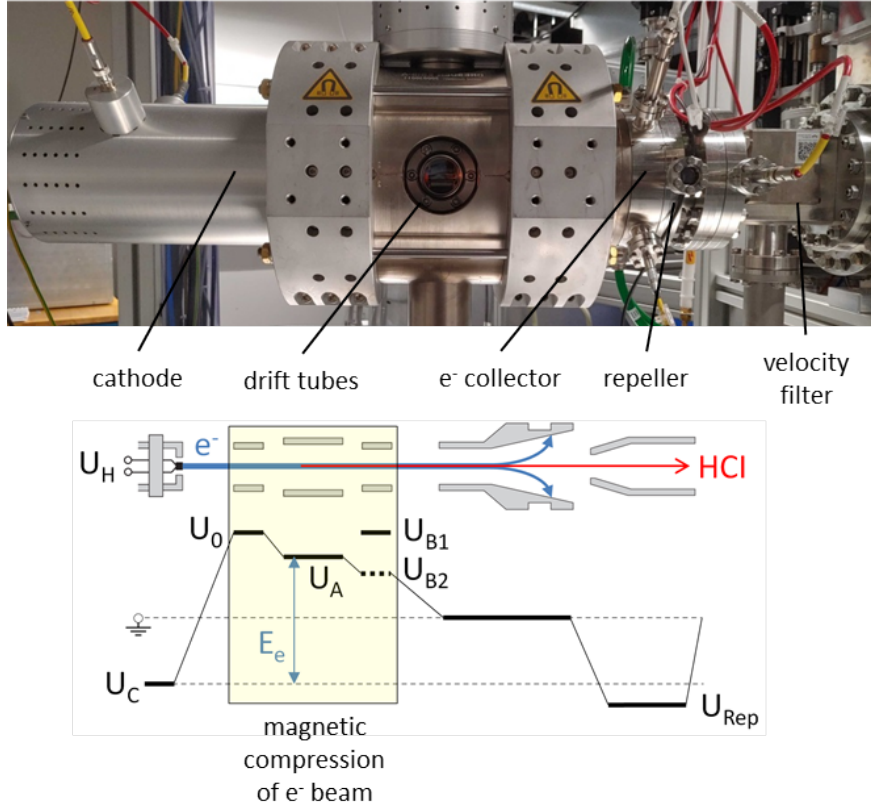


Figure 3.2: Picture (top) of the Dresden EBIS-A at COALA and schematic illustration (bottom) of the potentials inside the EBIS (not to scale). Partly taken and modified from [65].

The molecules are broken up by the electron beam and the atoms become ionized. For some elements like B and Fe volatile organic compounds exist which become gaseous under low pressure. This is referred to as MIVOC method. A compilation of already used and proposed compounds can be found in [91, 92]. The range of ions that can be produced by the EBIS can be further extended by feeding singly-charged ions from other ion sources into the EBIS for further charge breeding.

The EBIS was delivered together with a subsequent velocity filter (Wien filter), in which the ions with mass m and charge q can be separated by their q/m ratio. Therefore, a horizontal magnetic field with $B_{\text{vel}} = 500 \text{ mT}$ is crossed with a vertical electric field $0 \leq E_{\text{vel}} \leq 720 \text{ kV/m}$. The electric field is generated by two electric plates with a distance of $d = 1.93 \text{ mm}$ with applied voltages $\pm U_{\text{vel}}$, respectively. Depending on $E_{\text{vel}} = 2 \cdot |U_{\text{vel}}|/d$, only ions with matching

$$\frac{q}{m} = \frac{E_{\text{vel}}^2}{B_{\text{vel}}^2} \cdot \frac{1}{2U_A} \quad (3.1)$$

are not deflected. All other ions are deflected in the vertical direction and removed from the beam by a 2 mm diameter aperture at the exit of the Wien filter. This simplifies the optimization

of the ion production and reduces space-charge effects induced by unwanted ions.

3.2 Switchyard

The production of highly charged ions with an EBIS requires an ultra-high vacuum below 10^{-9} mbar inside the source. This makes it mandatory to bake out the whole source over several days after venting. Together with the heavy frame including the pumping stages, this source is not readily interchangeable like ion sources that have been used at COALA so far. Since the setup described in [80] had only one ion source port, a new switchyard for multiple sources was designed to ensure rapid switching between different ion sources.

The design is based on a switchyard from the Extra Low ENergy Antiproton (ELENA) ring at CERN and details can be found in [93, p. 146]. Figure 3.3 shows the adapted COALA version without the cover flange for better visibility. The main difference to the ELENA version is the equally spaced 120° arrangement of the bending electrodes (a) while keeping all other symmetries from the original design. This has some advantages for the COALA setup: Not only can the ions be directed straight into a possible other experiment like a mass-resolving time-of-flight setup at port (j) or (k) instead of the main beamline (e), but there is also the option to feed the EBIS (h) from another ion source like a liquid metal ion source (LMIS) either straight from port (j) or through bending the ions in the other direction from port (i). This enables the usage of different ion sources for collinear laser spectroscopy and it enables the usage of the same sources for new experiments. Additionally, the original 10° port (g) was also included. Ions coming from this port can only be directed to the main beamline (e) with the two steerer electrodes in front of the exit into (e). Therefore, the pivot point of this axis is not in the center of the surrounding chamber but between the two electrodes of port (e). The exact point has been optimized with the goal of minimal beam disturbances in ion beam simulations with the software SIMION³. In order to measure the ion current from each ion source and to estimate the ion beam size, a Faraday cup (b) with an iris diaphragm in front is installed in the center of the chamber. This cup can be rotated to each port and moved in and out with a linear z -stage. Since the central axis of port (g) does not pass the center of the chamber, another Faraday cup for the 10° port (c) has been implemented in a straight line. A disadvantage of the switchyard design is the double-focusing behavior which is illustrated with SIMION simulations in Fig. 3.4. It shows a focus in the horizontal ion flight plane (1) and in the vertical plane (2) with different focal lengths. This can be compensated through a following quadrupole-doublet to re-collimate the ion beam. An aligned iris diaphragm (d) can be used to ensure a central entry into the quadrupole-doublet. Opposite to the main beamline port (e) is the laser entry port (f).

This new switchyard is an important part for the laser spectroscopic investigation of highly charged ions like C^{4+} within this work and it brings many new possibilities for upcoming experiments to COALA as will be discussed in the outlook.

³SIMION™ 8.0 © 2003-2006 Scientific Instrument Service, Inc.

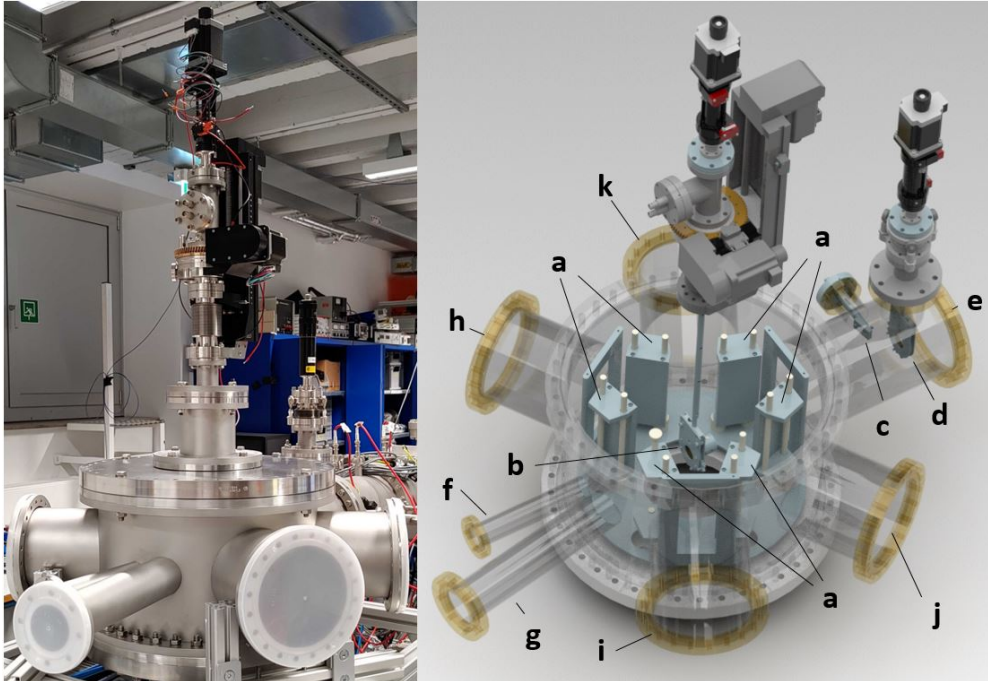


Figure 3.3: The new switchyard for COALA adapted from a design used at the Extra Low ENergy Antiproton (ELENA) ring, CERN [93]. Details can be found in the text.

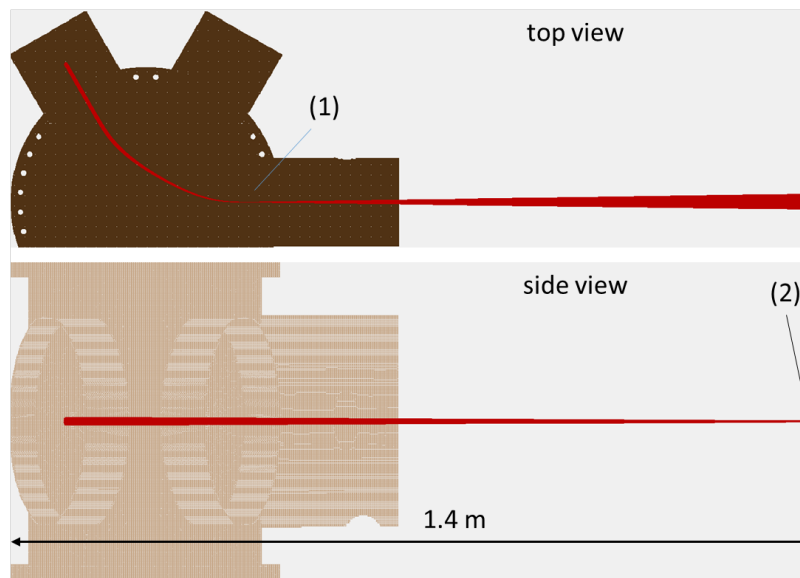


Figure 3.4: Illustration of the double-focusing behavior of the switchyard with SIMION simulations. The simulated ion beam (red) is deflected and focused with different focal lengths in the horizontal (1) and vertical (2) ion flight plane. These foci can be compensated through a following quadrupole-doublet.

3.3 Diagnostic stations

The purpose of the beam diagnostic stations (DS) is to monitor the number of incoming ions, to investigate the beam shape and - most importantly - to ensure a good ion-laser beam superposition. In the original design, two 6-way CF150 crosses were equipped with a Faraday cup, a 45°-tilted phosphor screen with an off-vacuum camera and an iris diaphragm which can be opened and closed from the outside. These two irises define the common laser and ion beam axis which is crucial for CLS. However, the old design which can be found in [80] had several disadvantages: First, the iris diaphragm was directly connected to the rest of the diagnostic elements, which complicated a precise alignment and required a realignment every time the diagnostic elements are taken out for repair or changes. Additionally, the mechanism to open and shut the iris was not reliable enough and had a strong hysteresis. Secondly, the slides to move the diagnostics vertically got stuck regularly. Third, the phosphor screen itself is only sensitive to ion currents above 100 fA. All of these points have been addressed in the new design shown in Fig. 3.5.

In the new design, the sliding solution of the diagnostics holder was discarded and replaced by a fixed holder which is mounted to a linear z -stage. In the redesign process, the iris diaphragm (b) with a 25 mm diameter was separated from the ion beam diagnostics and moved to an adjustable flange (e). This improves the alignment precision vastly. Furthermore, the open and close mechanism is now more reliable by using a small spring, which pulls the iris open, and a motorized linear feedthrough (f) that can counteract to shut the iris. Last but not least, the

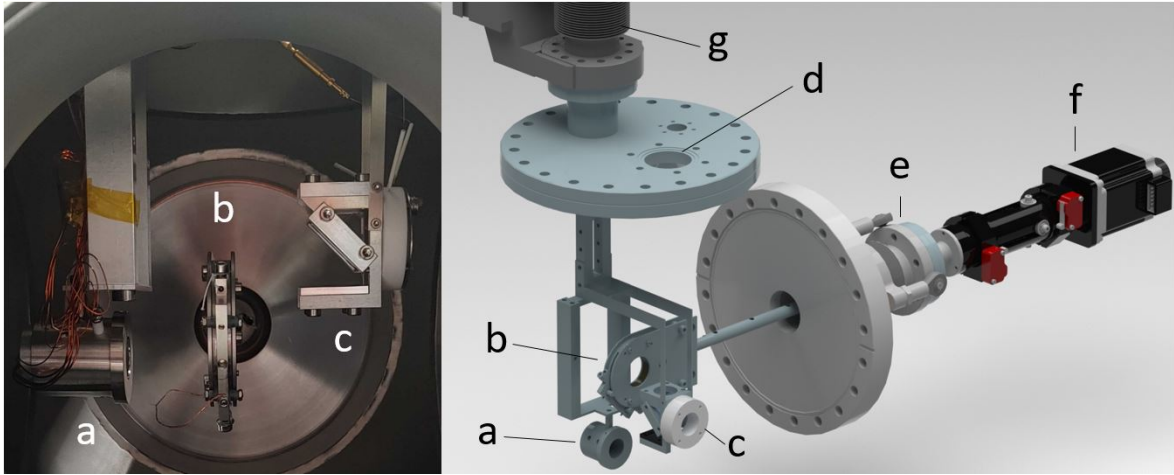


Figure 3.5: New version of the diagnostic stations. A Faraday cup (a) and a multichannel plate with phosphor screen stack (c) are mounted to a linear z -stage (g). The fluorescence light of impinging ions or laser photons can be observed through a view port (d) and a 45° beam splitter. The iris diaphragms (b) define the ion-laser beam superposition axis. They can be opened and closed with a motorized linear feedthrough (f). The alignment of the iris has been improved by decoupling the iris from the rest of the element holder and the usage of an adjustable flange (e).

phosphor screen has been replaced by a chevron-style multichannel plate (MCP) combined with a phosphor screen in a stack (c). Impinging ions release electrons in the MCP which are accelerated through a high voltage onto a second MCP where the incoming electrons are further multiplied. This electron avalanche is then accelerated further onto the phosphor screen where they induce fluorescence light. The electron gain in the MCPs can be controlled through the applied high voltage across the plates and, therefore, ion currents of 1 nA can be measured as well as single ions impinging onto the device. This allows the observation of small ion bunches with highly charged ions from the EBIS as well as continuous beams from surface ionization or liquid metal ion sources. A UV beam splitter is incorporated into the MCP holder to monitor the ion beam as well as the superposition with the laser beam at the view port (d). Figure 3.6 shows a camera recorded picture of the MCP fluorescence only with ions (right) and together with the laser beam (left). This system allows a robust and reliable check for a very good laser-ion beam overlap through the following routine: At first, the collinear laser beam is aligned to the axis defined by the two irises of the two diagnostic stations but also with respect to a minimal laser-induced background in the PMTs. Then, the anticollinear laser beam is superposed with the collinear laser beam. This overlap can be ensured over a path length of about 5.2 m with an uncertainty of 0.2 mm on both beamline sides resulting in a maximum angle of about $\arctan(2 \cdot 0.2 \text{ mm} / 5.2 \text{ m}) \approx 0.077 \text{ mrad}$. In a last step, the already pre-aligned ion beam is superposed with the laser beams by using the new MCP stacks. Due to the larger ion beam size compared to the laser beams and the shorter overlap distance of about 2.6 m, a conservative estimation of the largest angle between the ion and the laser beam is $\arctan(2 \text{ mm} / 2.6 \text{ m}) \approx 0.77 \text{ mrad}$.

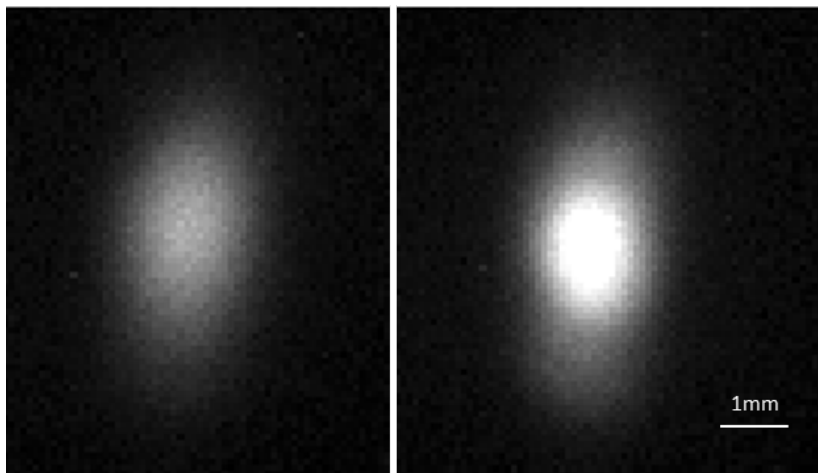


Figure 3.6: Ion and laser beam overlap on a MCP stack. The left panel shows a picture taken with only the ion beam while in the right panel the laser beam was also present. The pictures were recorded with a CCD camera on top of the view port.

3.4 Laser system

The rest-frame wavelengths of the $^3S_1 \rightarrow ^3P_J$ transitions in C^{4+} range from 227.1 nm to 227.8 nm. The production of this UV light is accomplished by frequency quadrupling of ≈ 910 nm light from a titanium-sapphire (Ti:Sa) laser. The Doppler shift in this transition for $^{12}C^{4+}$ with $E_{\text{kin}} = 42$ keV is about ± 0.5 nm for the respective direction. Therefore, two independent laser systems for the collinear and anticollinear direction are required to enable fast measurement cycles. The full laser setup is illustrated in Fig. 3.7 and is almost identical to the one described in [80, 82].

The Ti:Sa lasers⁴ are pumped by a 20 W and 25 W Nd:YAG laser⁵ respectively. The fundamental infrared laser light is then frequency quadrupled in two steps by second harmonic generation enhancement cavities⁶. Before the laser beams are sent to the experiment, a combined spatial filter and telescope setup is used to form a collimated, Gaussian-shaped beam profile. The two lenses have a focal length of $f_1 = 75$ mm and $f_2 = 200$ mm. For the collinear laser a 1:1 telescope with two $f = 50$ mm lenses just in front of the beamline is used to recollimate the

⁴Sirah Lasertechnik GmbH, Matisse 2 TS

⁵Spectra Physics, Millennia eV

⁶Sirah Lasertechnik GmbH, WaveTrain 2

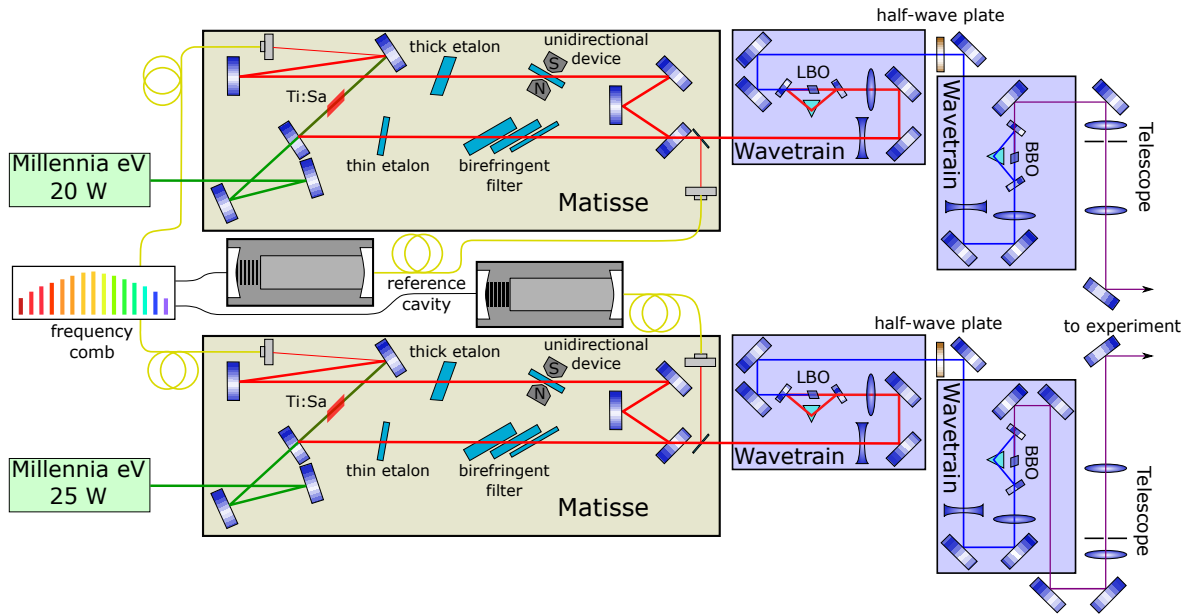


Figure 3.7: Laser setup for the production of 227 nm laser light. One laser system consists of a Nd:YAG pumped Ti:Sa laser whose light is subsequently frequency quadrupled by two second harmonic generation enhancement cavities. The free-space UV laser light is transported via mirrors to the beamline setup. The mode-matching inside the optical detection region has been accomplished through telescope setups. The laser frequency is stabilized and measured by a tunable reference cavity and a GPS referenced frequency comb. Adapted from [82].

laser beam. This is necessary due to the longer path length of the collinear laser beam. All lens distances in the telescopes are chosen to have a good laser beam overlap inside the optical detection region with a low laser background at the same time. This resulted in a $1/e^2$ beam diameter of ≈ 1.2 mm for both directions inside the ODR.

For accurate laser spectroscopy results, the laser frequency has to be stable and well-known. This is accomplished by a tunable reference cavity for fast frequency stabilization and a GPS-referenced frequency comb⁷ to compensate slow frequency drifts of the reference cavity.

⁷Menlo Systems FC1500-250-WG

4 EBIS-A ion production

The first step towards laser spectroscopy of $^{12}\text{C}^{4+}$ is the commissioning of the new electron beam ion source. In this chapter, the charge-state distribution of produced ions in different operation modes are compared and analyzed through velocity filter scans. Afterwards the source parameters are optimized with regard to the C^{4+} production.

4.1 Pulsed mode

The typical EBIS operation mode is the pulsed-beam output mode where the trapped ions are charge bred and ejected as an ion bunch after the time t_{breed} through quickly pulsing the barrier voltage U_{B1} down to $U_{\text{B2}} \leq U_{\text{A}}$ (see Sec. 3.1 and Fig. 3.2).

The charge-state distribution of extracted ions can vary greatly depending on t_{breed} . In order to investigate this behavior, the velocity filter after the EBIS can be used. Ions can only pass this filter if they have the matching q/m ratio to the applied voltage U_{vel} as given by Eq. (3.1). By scanning U_{vel} and recording the respective ion current at the switchyard Faraday cup with a picoamperemeter, a detailed and well resolved charge distribution is obtained. An example of such a scan with residual gas in pulsed mode for $t_{\text{breed}} = 15$ ms is depicted in Fig. 4.1. With

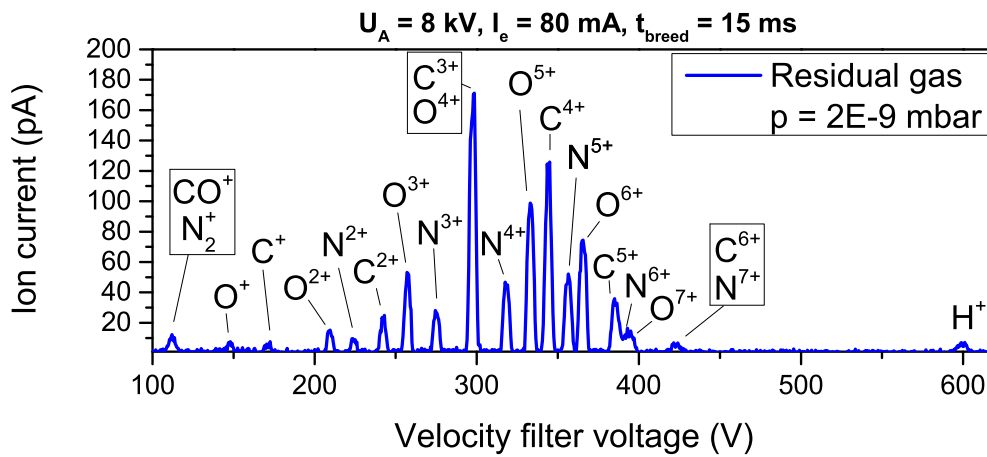


Figure 4.1: Velocity filter scan of the EBIS output in pulsed mode only with residual gas at a pressure of $p_{\text{gas}} = 2 \cdot 10^{-9}$ mbar. The charge breeding time of $t_{\text{breed}} = 15$ ms results in a charge state distribution centered around medium charge states of elements which are the main constituents of residual air and propane gas.

Eq. (3.1) each peak can be assigned to a q/m ratio. In case the deflector plate distance d is unknown, it can be determined with the set voltage U_A and the peak position of H^+ since it is always the peak with the highest deflector plate voltage U_{vel} due to the highest possible $q/m = 1$. The other peaks can now be assigned through a rough knowledge of the gas present inside the EBIS (mainly residual air and some propane in case of Fig. 4.1) and the assumption of a continuous charge state distribution. This means that a charge state q has to be present in the spectrum if the neighbouring charge states $q \pm 1$ are identified. Some charge state and element combinations have the same q/m ratio like $^{12}C^{6+}$, $^{14}N^{7+}$ and $^{16}O^{8+}$. These cannot be separated in a velocity filter and the proportion of each overlapping state can only be estimated by the neighbouring charge states.

4.2 Production of $^{12}C^{4+}$ in pulsed mode

The easiest way to produce highly charged ions of the desired element is by feeding an appropriate gas into the EBIS. In case of carbon, propane gas (C_3H_8) was used since it is easily available. But also other gases like methane (CH_4) could be used. The molecules are broken up by the electron beam and generated ions are confined. By trapping and charge breeding an ion cloud for t_{breed} , the charge state distribution is shifted towards higher charge states for longer times t_{breed} . This is illustrated in the left panel in Fig. 4.2 for three different breeding times $t_{breed} = 4, 15, 50$ ms. For a better comparison, the mean current over 1 s measured by the picoamperemeter has been normalized to the respective pulse rate. Note, that the trap is open for 1 ms after the breeding time which results in a breeding period of $T_{breed} = t_{breed} + 1$ ms. An observed C^{4+} particle current of 470 ppA for $t_{breed} = 15$ ms therefore corresponds to a particle charge per pulse of 7.5 ppAs.

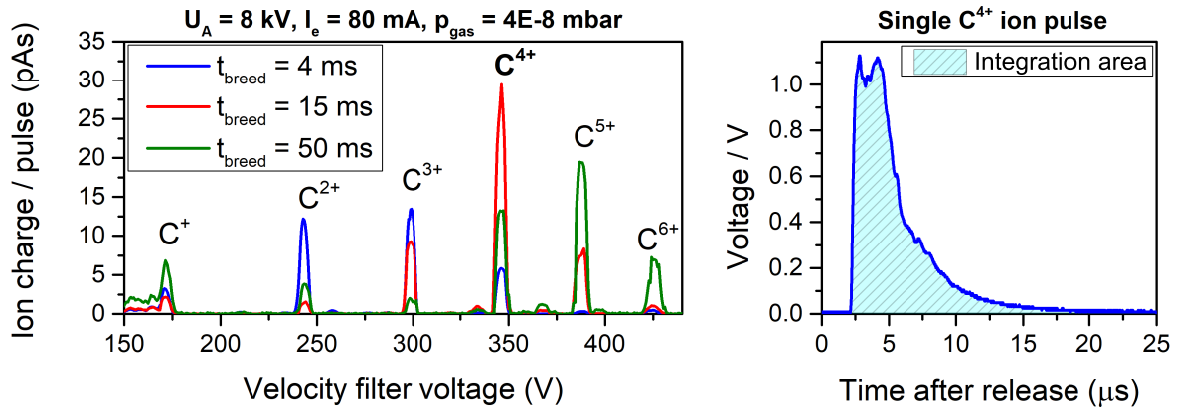


Figure 4.2: *Left panel:* Velocity filter scans in pulsed mode for three different breeding times $t_{breed} = 4, 15, 50$ ms. The charge state distribution is shifted towards higher states for longer breeding times. *Right panel:* Ion pulse detection with a current amplifier. The area under the pulse (shaded light blue) corresponds to the number of ions per pulse.

A more elaborate way to investigate single pulses is by detecting them with a fast current-to-voltage amplifier⁸ and an oscilloscope at the switchyard Faraday cup. Such a C^{4+} pulse is depicted on the right in Fig. 4.2. Hereby, the number of ions within each pulse is given by $N_{\text{ion}} = A/(q \cdot G)$ with the area of the pulse A , the charge of the ions $q = 4e$ and the amplifier gain $10^5 \text{ V/A} \leq G \leq 10^7 \text{ V/A}$. The typical pulse length is $\Delta t_{\text{pulse}} \approx 10 \mu\text{s}$. The number of C^{4+} ions is optimized through a variation of different production parameters like electron current, trap depth, feeding gas pressure and breeding time.

4.2.1 Electron current vs. trap depth

The ion confinement trap is set by the axial potential $\Delta U_{\text{trap}} = U_{B1} - U_A$ and the radial potential given by the space charge of the electron beam current I_e as explained in Sec. 2.3.5. In the left panel of Fig. 4.3 the number of extracted ions is plotted as a function of ΔU_{trap} for different electron currents I_e . Since the radial potential is increased with higher electron current as given by Eq. (2.22), more ions are preserved and can be extracted from the trap. The axial trap depth ΔU_{trap} has to be adjusted accordingly in order to fully exploit the radial trap potential. When it is reached, any additional ions which could be trapped axially will leave the trap radially and a plateau becomes visible. The height of these plateaus increases linearly with I_e as depicted on the right in Fig. 4.3. The electron current I_e is technically limited to 120 mA, but in order to increase the lifetime of the electron cathode, a typical current of $I_e = 80 \text{ mA}$ was used in this work.

This behavior has also been investigated in [64, 91] with other setups where similar observations were made, but the detailed characteristic is unique to each EBIS.

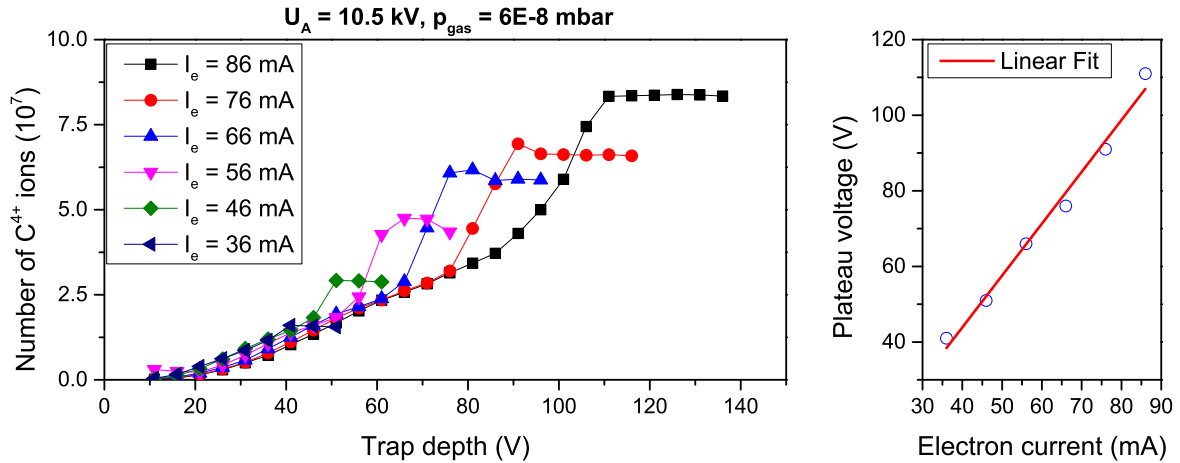


Figure 4.3: Number of extracted C^{4+} ions for several trap depths ΔU_{trap} and electron currents I_e (left panel). When ΔU_{trap} reaches the space-charge potential of the electron beam, no additional ions are trapped and a plateau is reached. The plateau height increases linearly with I_e (right panel).

⁸Femto DHPA-100

4.2.2 Feeding gas pressure and breeding time

For the production of C^{4+} , propane gas was continuously fed into the EBIS. The gas pressure p_{gas} can be set and is then stabilized by an electronic feedback loop. Fig. 4.4 shows the number of extracted ions for several breeding times t_{breed} and three different p_{gas} . The electron current was set to $I_e = 80$ mA and the trap depth to $\Delta U_{\text{trap}} = 200$ V. For all three pressures the number of extracted ions increases with longer t_{breed} until it reaches a maximum and starts to decline slowly afterwards. This was already visible in Fig. 4.2 and can be explained by the shift of the charge state distribution. The maximum number of C^{4+} was found for $t_{\text{breed}} = 15$ ms and $p_{\text{gas}} = 6 \cdot 10^{-8}$ mbar which is the technical limit. A higher gas pressure would strongly decrease the lifetime of the electron cathode.

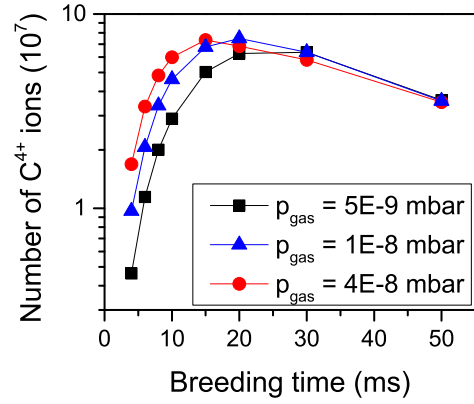


Figure 4.4: Number of extracted C^{4+} ions for several propane gas pressures inside the EBIS and breeding times with $\Delta U_{\text{trap}} = 200$ V and $I_e = 80$ mA.

4.3 Transmission and leaky mode

In transmission and leaky mode the barrier voltage U_{B1} is lowered to $U_0 > U_{B1} \geq U_A$ and kept statically. While $U_{B1} \leq U_A$ leads to immediate extraction of all generated ions (transmission mode) and can only produce lowly charged ions, the leaky mode can also produce higher

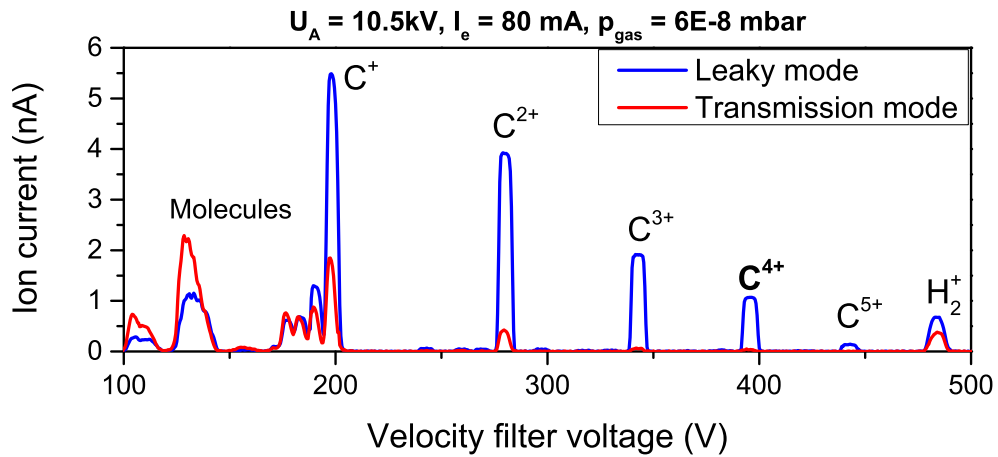


Figure 4.5: Velocity filter scan comparison between C^{4+} optimized leaky mode and transmission mode.

charge states if the axial trap depth ΔU_{trap} is setup correctly. When ΔU_{trap} is chosen too high, the ions cannot leave the trap. When ΔU_{trap} is too low, the ions cannot reach the desired charge state before they leave the trap. Fig. 4.5 compares the output of both modes. In leaky mode, the trap parameter $\Delta U_{\text{trap}} = 190 \text{ V}$ was optimized for the production of C^{4+} yielding a particle current of $I_p = 0.35 \text{ pA}$. This yield is comparable to the Ca^+ yield from the surface ionization source used in [82] raising the expectation of continuous beam CLS with C^{4+} although only a portion of these ions is expected to be in the metastable $1s2s^3S_1$ configuration.

5 Collinear laser spectroscopy with $^{12}\text{C}^{4+}$ ions

5.1 Characterization of $^{12}\text{C}^{4+}$ spectra with a single laser system

The precise determination of a line center depends strongly on its signal-to-noise ratio (SNR), the symmetry of the lineshape and its width. Thus, EBIS production parameters were optimized to achieve a significant population of the $1s2s\ ^3\text{S}_1$ state and a symmetric and narrow line profile simultaneously. During these optimizations, a single anticollinear laser beam was used and the strongest fine-structure transition $1s2s\ ^3\text{S}_1 \rightarrow 1s2p\ ^3\text{P}_2$ of $^{12}\text{C}^{4+}$ was studied. The laser frequency ν_a was measured with a GPS-stabilized frequency comb and fixed to match the Doppler-shifted resonance condition $\nu_c = \nu_0\gamma(1 - \beta)$ coarsely as explained in Sec. 2.4. Scans across the resonance were performed with Doppler-tuning by applying a scan voltage U_{DAC} to the floatable optical detection region (see Sec. 2.4 and Sec. 3). All photon counts registered by the PMTs were time tagged with 10 ns resolution for each U_{DAC} by the FPGA-based data acquisition system [94]. In the analysis process, the scan voltage U_{DAC} was converted to a corresponding scan frequency of the laser with the differential Doppler shift given by Eq. (2.41) and the initial acceleration voltage of the ions which was $U_A \approx 10.5$ kV in all measurements.

5.1.1 Resonance spectra with a bunched ion beam

The natural production mode of an EBIS is the so-called bunched-beam mode as described in Sec. 3.1. The trapped ions are charge bred for a time t_{breed} . After this time, the potential of the ejection electrode U_{B1} is lowered and the ions are accelerated into the beamline. The choice of the breeding time t_{breed} determines the charge distribution of the ion cloud as shown in Fig. 4.2. Other production parameters are the electron current I_e , the axial trap depth $\Delta U_{\text{trap}} = U_{\text{B1}} - U_A$ and the methane gas pressure inside the EBIS p_{gas} . The interplay of all of these parameters defines the electron space charge, the capacity of the trap and the temperature of the ion cloud as explained in Sec. 2.3. Especially the latter is very important since a colder ion cloud results in a smaller linewidth which improves the statistical uncertainty in the line-center determination. The comparison of many parameter combinations has shown that the amount of produced ions per bunch and the ion cloud temperature cannot be optimized simultaneously but a trade-off has to be made for many parameters. A typical example is shown in Fig. 5.1. Panel (a) and (b) are time-resolved spectra for two different EBIS parameter sets given in the first two lines of Tab. 5.1. In a time-resolved spectrum, the number of photon counts is depicted color-coded as a function of the scan voltage (top x -axis) or the corresponding scan frequency (bottom x -axis) and the time after the ejection of the ions from the EBIS (y -axis). It should be noted that - even though the vertical axis represents the time-of-flight of the ions - the vertical position cannot be directly related to the kinetic energy of the ions since it also depends on the complex extraction

process and the position of the ions in the trap at the time of release. The velocity of the ions is rather encoded in the position of the resonance along the x -axis because it represents the Doppler-shift. The black line elucidates the change of the resonance frequency through the time window. In this picture, the energy distribution of the ion bunch is visualized in a time-resolved way from bottom to top where ions more on the right side of the x -axis have less kinetic energy than ions on the left side.

It enables an analysis of the ion ejection behavior. One can identify roughly three different

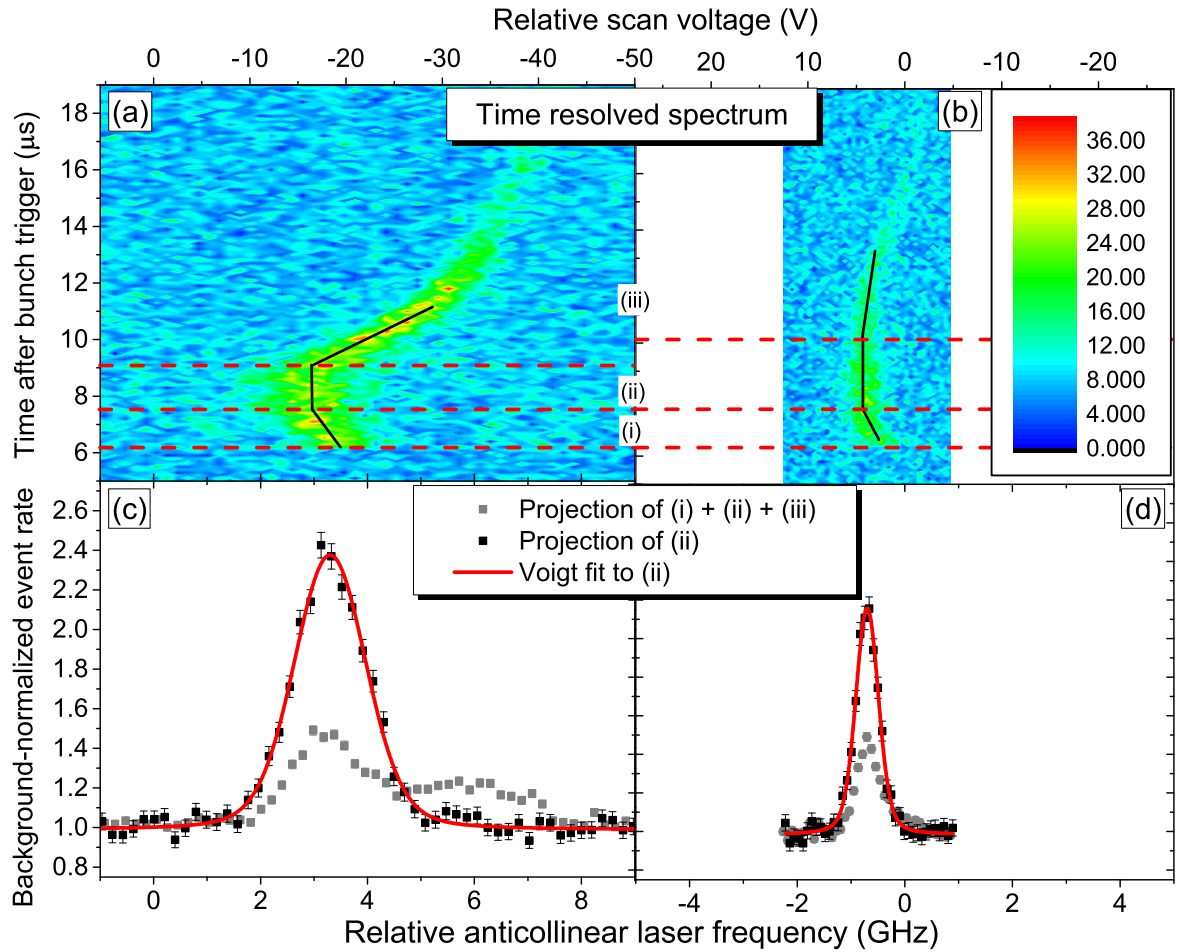


Figure 5.1: Time-resolved spectra for two different EBIS production parameter sets (a) and (b) measured in anticollinear geometry with a laser power of 2 mW. The projection of the photon events within time window (ii) onto the laser frequency axis is shown in panel (c) and (d) as black squares along with a Voigt fit (red line). The full projection of time window (i) + (ii) + (iii) is depicted as grey squares and exhibits a strong asymmetry for the parameter set (a). The production parameters and the FWHM of the Fit are detailed in Tab. 5.1. Further explanation can be found in the text.

parts separated through the red dashed lines. It shows two parts, (i) and (iii), in which the ion energy changes with time whereas it is constant in part (ii). For laser spectroscopy, a time-independent behavior is required to allow for a precise and accurate determination of the resonance frequency. It is obvious that a projection of all fluorescence events onto the frequency axis leads to a strongly asymmetric resonance profile as it is depicted in grey in panel (c) and (d) of Fig. 5.1, whereas restricting the projection to the time period (ii), in which the resonance frequency is constant, provides a symmetric and narrower resonance signal as shown by the black data points.

In part (i), the ion energy increases from some lower value to the nominal ion energy of the "main bunch" (ii) which can be explained by the switching behavior of the ejection electrode. Due to the capacitance of the electrode and the cables connecting it to the high-voltage supply, the potential change of the electrode is not instantaneous but has a switching time of a few μs according to the manufacturer. At a certain potential, a part of the ions start to leave the trap while the potential of the electrode is still changing. Thereby, the electrode acts unintentionally as a pulsed drift tube⁹ for these ions, which results in less kinetic energy compared to later ions.

In the last part (iii), the energy of the ions decreases again. This can be understood as an effective probe of the space-charge potential of the electron beam. In an empty trap, it lowers the nominal start potential U_A . At the time of ejection, however, the positive charge of the ion cloud partly compensates the negative electron potential. Therefore, the first ions start on a potential closer to U_A . After some time, when the main part of the ion cloud has left the trap, the negative electron space-charge potential is less compensated and later ions therefore start on a reduced potential. This leads to a reduced kinetic energy of these "tail" ions after the acceleration against the ground potential. The space-charge potential $V_e(r)$ depends on the electron current I_e as explained in Sec. 2.3.5. Hence, the frequency "chirp" in (iii) should be reduced for lower electron currents. This is indeed visible in panel (b) of Fig. 5.1 where the electron current was reduced from 80 mA to 25 mA and the axial trap depth from 71 V to 26 V. These settings yield less C^{4+} ions in total, but the space charge induced tail is less prominent and the frequency shift is strongly reduced. The main part (ii) with a constant frequency lasts considerably longer than with the high-current settings.

⁹A pulsed drift tube is typically used as an "elevator" of the ion energy. Thereby, a voltage is applied at a drift tube while ions are located inside the tube, resulting in an acceleration or deceleration of the ions after leaving the tube due to the changed tube potential.

Table 5.1: EBIS production parameters, signal-to-noise ratio, FWHM and statistical line-center uncertainty $\Delta\nu_{\text{center}}$ of the spectra in Figs. 5.1 (a, b) and 5.2 (a-d).

	Fig.	$I_e /$ mA	$\Delta U_{\text{trap}} /$ V	$p_{\text{gas}} /$ mbar	$t_{\text{breed}} /$ ms	SNR	FWHM / GHz	$\Delta\nu_{\text{center}} /$ MHz
(a)	5.1/5.2	80	71	$6 \cdot 10^{-8}$	15	58	1.59(4)	16.6
(b)		25	26	$6 \cdot 10^{-8}$	15	51	0.50(1)	5.7
(c)	5.2	25	26	$2 \cdot 10^{-8}$	15	17	0.97(4)	17.8
(d)		80	171	$6 \cdot 10^{-8}$	leaky	59	0.168(2)	0.7

Additionally, the reduced electron current does not only reduce the space-charge potential but also leads to a lower temperature of the ion cloud (see Sec. 2.3.6). The temperature induced longitudinal energy distribution of the ion cloud is the main reason for the width of the resonance spectrum. If the projection is limited to the time window (ii), the asymmetry is removed and a symmetric lineshape is observed as shown as black squares in Fig. 5.1 (c, d). It can be well fitted by a Voigt profile (red line). For better comparability, the photon counts are normalized to the respective laser induced background. The full width at half maximum (FWHM) for $I_e = 80$ mA is about 1.6 GHz. Under the assumption that this width is mainly originating from the Doppler broadening, a thermal energy of the trapped ions inside the source can be estimated with Eq. (2.48) and the compression factor R . This results in $E_{th} \approx 11.1$ eV which is only slightly larger than expected from the simulations in Sec. 2.3.10. The reduction of the FWHM to 0.50 GHz for $I_e = 25$ mA is directly visible. The signal-to-noise ratio, which is indicated by the uncertainties relative to the signal height, is similar for both electron currents $I_e = 80$ mA (a) and $I_e = 25$ mA (b), although a reduced electron current leads to a proportionally smaller ion yield. The reason is the compression of the fewer ions into a smaller frequency range due to the reduced temperature. This demonstrates the advantage of a cooled ion bunch.

The electron current is not the only parameter which influences the ion temperature. When the axial trap depth ΔU_{trap} is lowered, hot ions, which have more energy than the critical energy (see Sec. 2.3.6), start to leave the trap and energy is removed from the thermal equilibrium which cools the remaining ions. This so-called evaporative cooling is used to additionally reduce the ion temperature like in panel (b) of Fig. 5.1. However, if ΔU_{trap} is too low, the resonance signal is reduced due to the ion loss. Therefore, the trap depth together with the ion current are trade-off parameters and have been tuned carefully during the measurement preparations. The best compromise was found in the parameters for setting (b) of Tab. 5.1, corresponding to Fig. 5.1 (b+d).

In contrast, a high methane gas pressure p_{gas} improves the production of C^{4+} and cools the ion cloud at the same time. Therefore, it was always set to the maximal value of $p_{gas} = 6 \cdot 10^{-8}$ mbar given by the technical limit of stable operation with a low frequency of sparking. The breeding time was usually kept at $t_{breed} = 15$ ms since its influence on the C^{4+} production is much larger than on the linewidth.

5.1.2 Resonance spectra with a continuous ion beam

The alternative EBIS production mode is the leaky mode as explained in Sec. 3.1. It yields a continuous ion beam instead of ion bunches. A particle current of $I_p = 0.195$ pA was measured at the last diagnostic station with the production parameters listed in line (d) of Tab. 5.1. A corresponding resonance signal of the continuous ion beam is shown in the right panel of Fig. 5.2 which also depicts bunched beam spectra on the left panel for comparison with production parameters provided in lines (a-c) of Tab. 5.1. All spectra that are displayed were recorded in roughly 4 minutes.

The strongly reduced linewidth from 1.6 GHz for settings (a) to 0.168 GHz for settings (d) is striking and improves the statistical line-center uncertainty from 16.6 MHz to 0.7 MHz as denoted in Tab. 5.1. Additionally, the reduced linewidth increases the SNR of the continuous

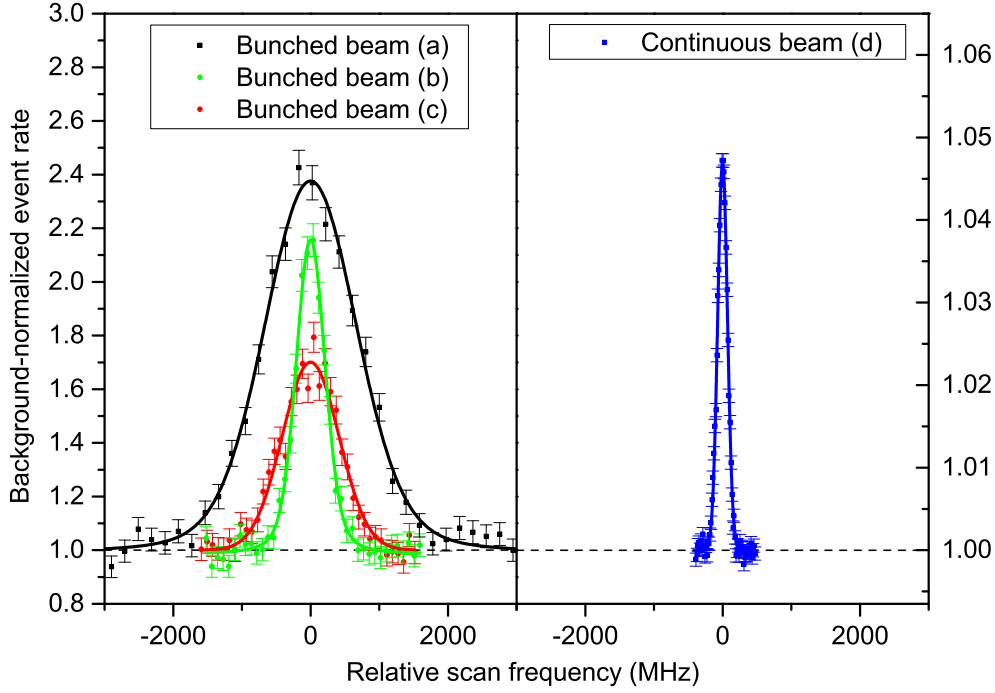


Figure 5.2: Comparison between bunched mode spectra (left) for different production parameters and a continuous beam spectrum (right) with their corresponding Voigt-profile fits (lines). All spectra have been recorded within 4 min measurement time in anti-collinear geometry leading to a similar signal-to-noise ratio. The laser power was in all cases 1.7 mW. All measurement parameters and fitting results are provided in Tab. 5.1.

beam spectrum linearly since the signal is concentrated in a smaller spectral range. However, comparing the measurement conditions of (a) and (d) in Tab. 5.2, a factor of 4.8 between the experimentally observed SN ratio and the theoretically achievable SN ratio is missing, or in other words, the SNR of (a) is $1/4.8$ times smaller than expected in comparison to the SNR of the continuous beam. A part of this discrepancy can be explained with the assumption that the laser probes a larger portion of the ion beam in case of (d) compared to (a). This cannot be quantified experimentally but is qualitatively reasonable since space-charge effects in the ion bunches make it difficult to achieve a collimated ion beam. However, this cannot explain the full factor of 4.8. Another contribution can be found in the relative population of the $1s2s\ ^3S_1$ state, which is expected to be larger in the leaky mode. The reason is the increased charge exchange rate from C^{5+} to C^{4+} in the steady state compared to a charge breeding time of 15 ms according to the simulations from Sec. 2.3.10. Figure 2.4 shows that the relative abundance of C^{5+} is increased by roughly a factor of 4 to 5 and with it also the charge exchange rate relative to the other production rates. Therefore, the main contribution of the missing factor 4.8 in the SNR is attributed to the larger population of the $1s2s\ ^3S_1$ state in the leaky mode than in the bunched mode.

Overall, the continuous beam delivers the better conditions for high-precision collinear laser spectroscopy and was therefore the preferred mode for all further investigations.

Table 5.2: SNR comparison of the spectra (a) and (d) in Fig. 5.2. Theoretically, the SNR of (a) should be 4.8 times larger than for (d) when the FWHM is included and under the assumption that the laser interacts with the same portion of ions per step in both cases. Instead, they are almost equal. The main contribution of the remaining factor 4.8 is attributed to the larger population of the $1s2s\ ^3S_1$ state in the leaky mode than in the bunched mode.

	Ions / step	Dwell time / step	Background rate	FWHM	SNR theo.	SNR exp.
(a)	$4.12 \cdot 10^9$	500 μ s	1 MHz	1.6 GHz		58
(d)	$4.8 \cdot 10^9$	4 s	0.389 MHz	0.168 GHz		59
$\frac{(a)}{(d)}$	0.86	1/8000	2.57	≈ 10	$\frac{0.86/10}{\sqrt{2.57/8000}} \approx 4.8$	≈ 1

5.1.3 Systematic drift of the line center

An important requirement for a precise rest-frame transition frequency determination through quasi-simultaneous collinear and anticollinear laser spectroscopy is a stable starting potential. Otherwise both laser beams probe different ion velocities and Eq. (2.55) is not valid anymore, resulting in a systematic shift of the measured transition frequency ν_0 . Therefore, the time dependence of the ions kinetic energy was investigated by repetitive recordings of resonances for 80 minutes. Each resonance spectrum takes about 2 min and the fitted line center with respect to the first measurement is plotted as a function of time in Fig. 5.3. The black data points were taken with the EBIS setup as delivered from the manufacturer and directly after turning on the EBIS for daily operation. In the first 30 min, moderate drifts of 50 MHz/h were observed, before the line center starts to drift more than 150 MHz in one hour which corresponds to a gradient of 2.5 MHz/min. For a typical time difference between a collinear and an anticollinear measurement of roughly 5 min as it is used in the measurements reported in Sec. 5.2, this corresponds to a systematic shift in the rest-frame frequency of 2.5 MHz/min \cdot 5 min = 12.5 MHz. Although this shift is rather large compared to the targeted accuracy of 2 MHz, it can be largely compensated by performing a collinear-anticollinear (CA) measurement after an anticollinear-collinear (AC) measurement. For a linear line-center drift $\frac{\partial \nu_{c/a}}{\partial t} = \text{const.}$, the remaining systematic shift between the real transition frequency ν_0 and the determined transition frequency from an averaged AC-CA pair measured with a constant time interval δt can be estimated as

$$\delta \nu_{\text{drift}} = \nu_0 - \frac{\sqrt{\nu_a(\nu_c + \delta \nu_t)} + \sqrt{(\nu_c + 2\delta \nu_t)(\nu_a - 3\delta \nu_t)}}{2}$$

with $\delta \nu_t = \frac{\partial \nu_{c/a}}{\partial t} \cdot \delta t$. For realistic values of ν_0 , $\nu_{c/a}$ and $\delta \nu_t \approx 12.5$ MHz, the systematic drift shift is $\delta \nu_{\text{drift}} \approx 50$ kHz, which is negligible in comparison to the targeted accuracy of 2 MHz. However, the size of $\delta \nu_t$ determines the scattering of the data points and, hence, the standard

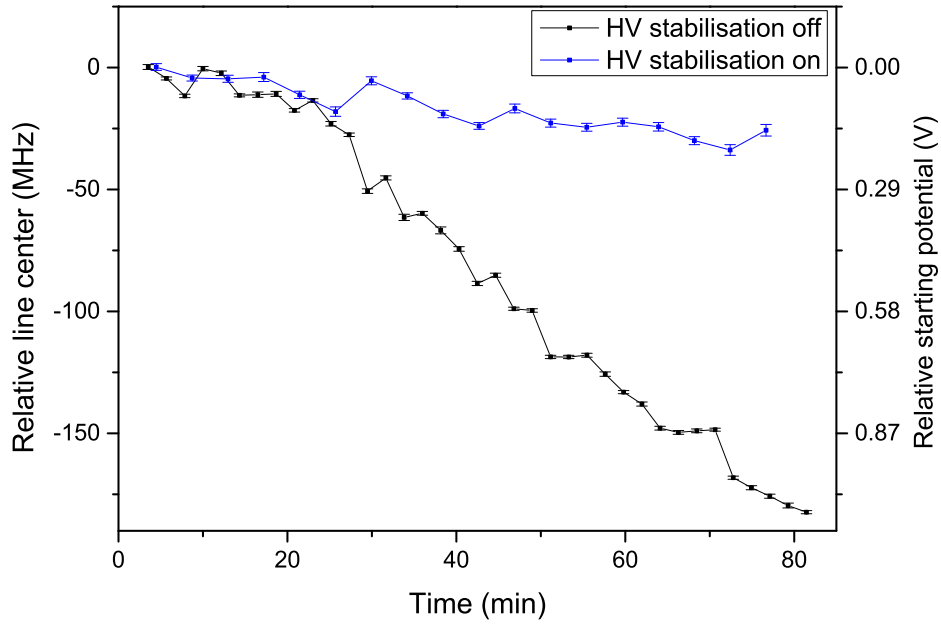


Figure 5.3: Relative line-center drift without (black) and with a high-voltage stabilization (blue) applied to the drift-tube potential U_A . The drift is reduced from approximately 2.5 MHz/min to 0.5 MHz/min which directly improves the statistical uncertainty in the quasi-simultaneous collinear and anticollinear laser spectroscopy approach and also reduces its systematic uncertainty. The remaining drift can be attributed to the degrading electron cathode of the EBIS (see text).

deviation and the uncertainty of the average.

Therefore, the drift was further investigated in order to find possibilities for improvement. With the differential Doppler-shift $\frac{\partial \nu_c}{\partial U} \approx 172 \text{ MHz/V}$ for $U_{\text{acc}} = 10.5 \text{ keV}$, the relative line-center shift can be converted to a corresponding change of the potential (right y -axis in Fig. 5.3). The drift of about 0.87 V/h is a typical value for the stability of high-voltage (HV) power supplies like the one used for the drift-tube potentials. In order to compensate this drift, the voltage applied to the central drift tube U_A was actively stabilized with a feedback-loop as explained in [84]. The basic idea is the stabilization of the HV to a precision high-voltage divider through an additional low voltage (0-5 V) generated by an electronic data acquisition card with a digital-to-analog converter¹⁰. The blue data points in Fig 5.3 are the result of a measurement series with active HV stabilization. A clear reduction of the drift from 2.5 MHz/min to 0.5 MHz/min is visible. This directly improves the accuracy in the determination of ν_0 . The reason for the remaining drift is twofold: First, the electron current in the EBIS was constantly decreasing during the measurements. This increases the starting potential of the ions through the reduction of the negative space charge. According to the manufacturer, this behavior is not typical and is attributed to a damage of the electron cathode. Unfortunately, no replacement cathode was available for this measurement campaign. Secondly, it was observed that the ion beam position

¹⁰LabJack T7, www.labjack.com

is also changing over time in one direction. This means the angle between laser and ion beam drifts and the part of the spatial ion velocity distribution probed by the laser is changing. Both effects influence the line-center position through the Doppler shift. However, the remaining drift can be tolerated since it does not severely reduce the accuracy compared to the targeted accuracy, other systematic sources and the statistical uncertainties.

5.2 Transition frequency determination in quasi-simultaneous collinear and anticollinear laser geometry

Quasi-simultaneous collinear and anticollinear laser spectroscopy has been used as explained in Sec. 2.4 to measure the $1s2s\ ^3S_1 \rightarrow 1s2p\ ^3P_J$ rest-frame transition frequencies ν_0 in $^{12}\text{C}^{4+}$. The data was recorded similar to Sec. 5.1 but for two superposed collinear and anticollinear lasers in an AC-CA scheme. To determine ν_0 from pairs of collinear (c) and anticollinear (a) measurements, the formula given by Eq. (2.55) has been used. It requires the knowledge of the respective laser frequencies $\nu_{c/a}$ measured by the frequency comb, and the voltage difference $\delta U = U_a - U_c$ of the resonance positions $U_{c/a}$ in the voltage space. For the extraction of $U_{c/a}$ from the resonance spectra, the raw data, which consists of the registered photon counts per digital-to-analog converter voltage U_{DAC} of the DAQ system, is converted into frequency space to account for the nonlinear relativistic voltage-frequency relation. The whole fitting process of the line-shape model to the data is carried out in frequency space and the center frequencies ν_{center} are determined for the collinear and anticollinear case. These frequencies are then converted back to the center voltages $U_{c/a}$ to extract the voltage difference δU . For regular measurements this voltage difference was usually smaller than $\delta U < 0.2\text{ V}$. Each rest-frame frequency ν_0 has an assigned statistical uncertainty given by

$$\Delta\nu_0 = \sqrt{\left(\frac{\partial\nu_0}{\partial\nu_a} \cdot \Delta\nu_a\right)^2 + \left(\frac{\partial\nu_0}{\partial\nu_c} \cdot \Delta\nu_c\right)^2 + \left(\frac{\partial\nu_0}{\partial\delta U} \cdot \Delta\delta U\right)^2}$$

with the laser frequency uncertainties $\Delta\nu_{c/a}$ and the propagated fit uncertainty $\Delta\delta U$. The laser frequency uncertainty $\Delta\nu_{c/a}$ is given by the standard deviation of the measured laser frequencies during a measurement.

A typical measurement cycle consists of about ten collinear and anticollinear resonance spectra pairs. Then, the resonance spectra for the two elliptic mirrors ODR1 and ODR2 are evaluated separately. The final transition frequency for a series $\bar{\nu}_0$ is then given by the mean of all single pairs weighted by $1/(\Delta\nu_0)^2$.

The statistical uncertainty σ for the mean value is chosen as the maximum of two values: The expected uncertainties of the weighted mean and the standard error of the mean (SEM)

$$\sigma_{\text{SEM}} = \frac{\sigma_{\text{std}}}{\sqrt{n}}$$

with the standard deviation σ_{std} of n extracted rest-frame frequencies. In almost all cases this was σ_{SEM} .

5.2.1 Systematic effects in quasi-simultaneous collinear and anticollinear laser spectroscopy

A main advantage of quasi-simultaneous collinear and anticollinear laser spectroscopy is that many typical systematic frequency shifts from classical CLS cancel if they appear in both directions. This raises the importance of similar conditions for both directions since systematic shifts only appear when the measurement or analysis conditions are different. Some effects leading to systematic shifts are largely compensated by doing a measurement series in the AC-CA scheme (see Sec. 5.1.3), but others do not cancel through this scheme. Therefore, several different sources for systematic shifts have been investigated and are discussed in this section.

Line shape

A crucial step in the analysis of laser spectroscopy data is the correct description of the data points by an appropriate line-shape model. In CLS, the line shape is usually given by a Voigt profile $V(\nu, \sigma, \gamma)$ which is a convolution of a Lorentzian and Gaussian shape as explained in Sec. 2.4.2. Most of the recorded data in this work is well described by

$$y(\nu, \nu_{\text{center}}, \sigma, \gamma, b) = V(\nu - \nu_{\text{center}}, \sigma, \gamma) + b \quad (5.1)$$

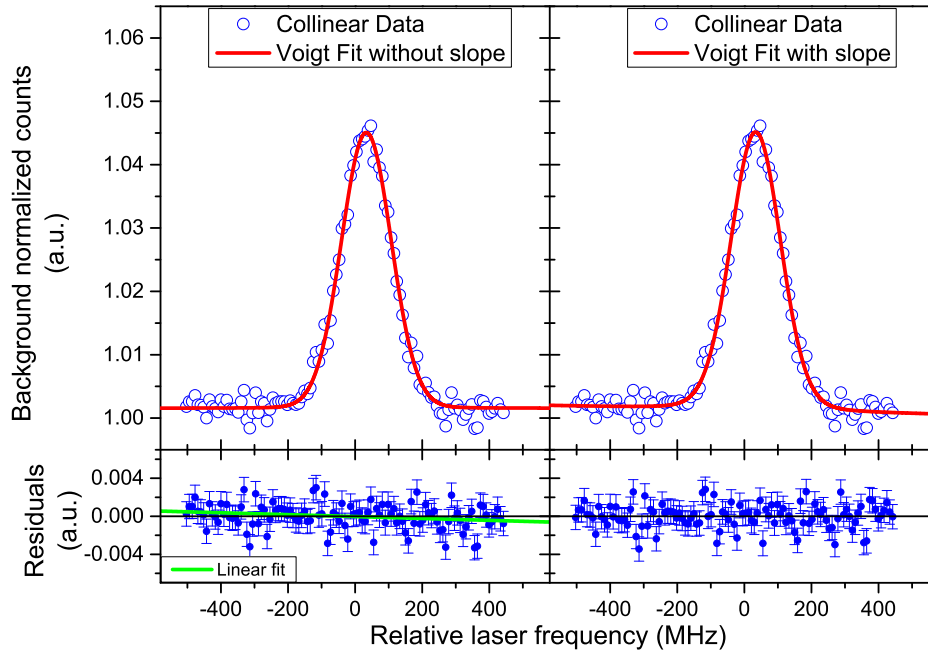


Figure 5.4: Comparison between a Voigt profile with static background (left) and with a linear background slope (right). The latter removes the slight tilt (green line) in the residuals of the static background fit. Although the line-center result is shifted by roughly 0.5 MHz, the influence to the rest-frame frequency determination is negligible when the same fit model is used for both directions.

where the line center ν_{center} , the Gaussian width σ , the Lorentzian width γ and the background offset b are free fit parameters. However, some spectra show a slight tilt in the residuals between data and fit as depicted on the left panel of Fig. 5.4 for a comparably extreme example. The green line is a linear fit to the residuals and visualizes the tilt which is probably the result of small laser power variations that are not completely compensated within the number of taken scans. In order to include this tilt in the data description, the fit model is slightly modified by a linear background slope $m \cdot b$ instead of a fixed background b . The new fit with the free parameter m is shown in the right panel of Fig. 5.4. Although this shifts ν_{center} by roughly 0.5 MHz in case of Fig 5.4, the influence to the rest-frame frequency determination has been found to be negligible as long as the same fit model is used for all resonance spectra. Nevertheless, the Voigt profile with linear background slope has been used during the analysis process.

Laser and ion beam alignment

In classical CLS, the alignment of the laser and ion beam has a strong influence on the line-center position since already a small angle between both beams can introduce shifts of some MHz through Eq. (2.39). For quasi-simultaneous collinear and anticollinear laser spectroscopy, this is strongly reduced as long as both laser beams are well aligned with respect to each other as explained in Sec. 2.4.1.

In order to verify this behavior in the experiment, the ion beam was displaced by about 1 mm relative to the laser beam position in the first diagnostic station while retaining the overlap in the second diagnostic station. Since both stations are separated by 2.6 m, this results in an angle of about $\alpha_{\text{IL}} = \arctan(1 \text{ mm}/2.6 \text{ m}) \approx 0.4 \text{ mrad}$ relative to the two laser beams which have an angle relative to each other of $\alpha_{\text{LL}} \leq \arctan(0.4 \text{ mm}/5.2 \text{ m}) \approx 0.077 \text{ mrad}$ as explained in Sec. 3.3. Figure 5.5 depicts the result and compares it against two reference measurements under optimal conditions, i.e. $\alpha_{\text{IL}} < 0.19 \text{ mrad}$. All values are compatible within their statistical uncertainties.

This behavior is expected to change significantly when a misalignment between the two laser

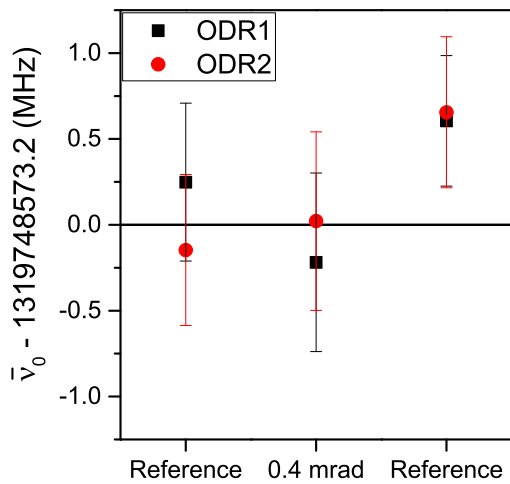


Figure 5.5: Systematic frequency shift for an ion beam misalignment of $\alpha_{\text{IL}} \approx 0.4 \text{ mrad}$ relative to the two laser beams in comparison to reference measurements where the angle was $\alpha_{\text{IL}} < 0.19 \text{ mrad}$. The counterpropagating laser beams were aligned in all cases with an angle $\alpha_{\text{LL}} < 0.07 \text{ mrad}$ between each other. No significant shift is observed.

beams is introduced. Therefore, a measurement series on different days with two different laser beam misalignments has been performed. The first configuration (a) was a horizontal crossing of the two laser beams with a separation of approximately 1 mm in front of each laser entrance window to the beamline. This introduces an angle of $\arctan(2 \text{ mm}/5.2 \text{ m}) \approx 0.38 \text{ mrad}$ between the two beams and an effective horizontal displacement of the two beam profiles in the ODR of roughly 0.55 mm. The second arrangement (b) was a vertical parallel displacement of also roughly 0.55 mm (\approx the beam radius) so that the laser beams propagated parallel to each other without crossing. The configuration (b) has also been tested without the velocity filter (VF) after the EBIS. In between each setting, reference measurements have been recorded where all beams were superposed again as good as possible. The extracted $\bar{\nu}_0$ from the first optical detection region ODR1 (black squares) and from the

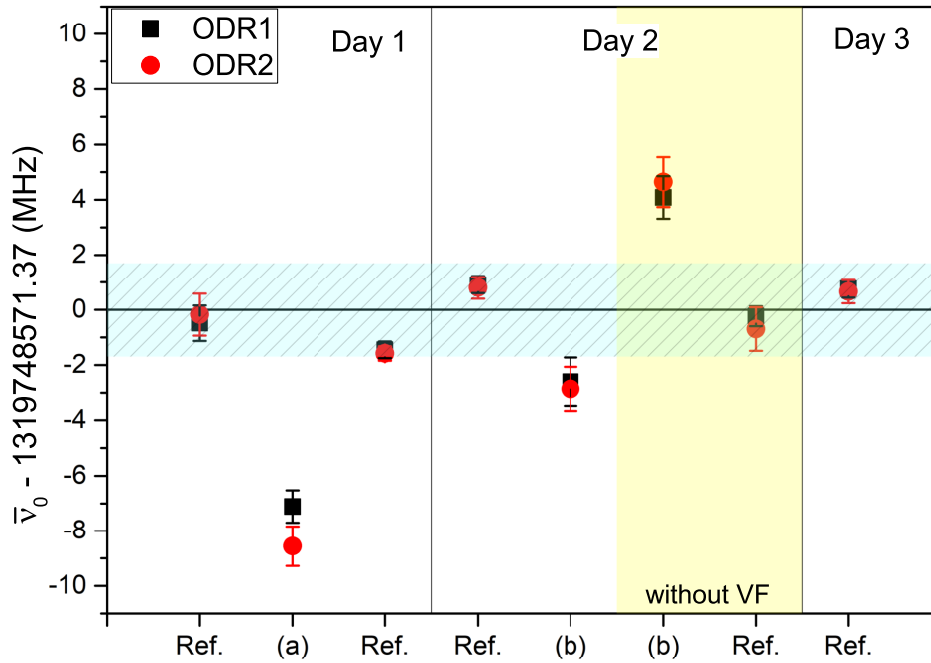


Figure 5.6: Measured rest-frame frequency $\bar{\nu}_0$ of the first optical detection region (ODR1, black squares) and the second one (ODR2, red circles) for reference measurements with optimal alignment and for two different laser beam misalignments. (a) is a horizontal crossing displacement, approximately a factor of 5 larger than the typical experimental uncertainty of the optimized setting as it is used for the reference measurements. From the maximal shift of 8.6(7) MHz a systematic uncertainty of $8.6 \text{ MHz}/5 \approx 1.7 \text{ MHz}$ for the reference measurements is estimated. This is marked as the blue shaded region, which covers indeed all reference measurements. Setting (b) is a vertical parallel displacement and shifts the results less than setting (a). When the velocity filter (VF) after the EBIS is turned off, the sign of the shift for setting (b) changes and the magnitude is increased slightly.

signal in ODR2 (red circles) are depicted in Fig. 5.6. From Eq. (2.42) and the assumption of $\alpha_{\text{IL}} \leq 0.4 \text{ mrad}$, the expected frequency shift of configuration (a) should be in the range of 0.4 MHz. The observed systematic shift of 8.6 MHz can, thus, not be explained by the introduced angle and must have a different origin. The explanation can be found in the spatial distribution of the ion velocity which is not homogeneous. Although a perfectly collimated ion beam is targeted in the experiment, this is not completely achieved. The ion beam has a residual divergence in the optical detection region and an additional small but existing horizontal energy dispersion due to the electrostatic switchyard. Thereby, two laterally displaced laser beams probe a different velocity distribution with a different mean velocity β even without any angle between them. This results in different Doppler shifts for the two lasers and a systematic shift in ν_0 . Any additional angle between the laser can either further increase or even decrease this shift depending on the probed distributions. This explanation has been confirmed through numerical simulations with SIMION 8.0 and Python 3 (see Appendix A.1).

The vertical displacement configuration (b) exhibits a smaller shift than (a). The reason can be found in the switchyard simulation from Sec. 3.2 which indicate the introduction of a stronger horizontal than vertical divergence by the switchyard. Since the Wien filter separates the ion velocities additionally in the vertical direction, a series was performed without velocity filter. This did not improve the behavior. Therefore, the Wien filter can be used without introducing additional uncertainties.

The largest shift of 8.6(7) MHz is produced in ODR2 with setting (a) which had a laser displacement of a factor $\approx 1 \text{ mm}/0.2 \text{ mm} = 5$ larger than the usual experimental reference superposition. Thereby, a systematic uncertainty for the laser beam alignment due to the spatial velocity distribution (VD) in the beam can be estimated with $\Delta\nu_{\text{VD}} = 8.6 \text{ MHz}/5 \approx 1.7 \text{ MHz}$ which is marked as a shaded light blue area in Fig. 5.6. This indeed covers all reference measurements and is only slightly larger than their 1σ -standard deviation of 0.8 MHz.

A consequence of this systematic uncertainty is that all other systematic effects need to be larger in order to be identified since the laser beam alignment uncertainty is part of every recorded measurement. So any possible shifts due to other systematic effects have to be compared to $\Delta\nu_{\text{VD}}$.

Photon recoil

During the resonant absorption of a photon, the ion has to overtake the photon momentum. After several excitation-emission cycles, this leads on average to an acceleration of the ion in the collinear setup or deceleration of the ion in the anticollinear setup as explained in Sec. 2.4.3. This means that the velocity β of the ions is changed after the first excitation differently for both directions. Therefore, a frequency shift towards a higher rest-frame frequency could in principle occur if more than one excitation takes place in the ODR. The mean number of scattered photons \bar{n}_{sc} in resonance until the middle of the first and the second mirror section (ODR1 and ODR2, respectively) can be estimated with Eq. (2.58). The result is summarized in Tab. 5.3 for two laser intensities $I_{\text{laser}} = 0.5I_0$ and $I_{\text{laser}} = I_0$. Here, a $^{12}\text{C}^{4+}$ ion beam with $E_{\text{kin}} = 42 \text{ keV}$ is assumed to be excited during its path to the middle of ODR1 ($l_1 = 11 \text{ cm}$) and to the middle of ODR2 ($l_2 = 22 \text{ cm}$). Due to the respective ion velocity of $8.22 \cdot 10^5 \text{ m/s}$, the interaction time for l_1 and l_2 is $t_1 = 133 \text{ ns}$ and $t_2 = 266 \text{ ns}$, respectively. When multiplied

Table 5.3: Estimated photon scattering in resonance ($\delta = 0$) from Eq. (2.58) for $^{12}\text{C}^{4+}$ ions with $E_{\text{kin}} = 10.5 \text{ keV}/q$ or $v = 8.22 \cdot 10^5 \text{ m/s}$, respectively.

Parameter	ODR1	ODR2
$l_{1/2}$	11 cm	22 cm
$t_{1/2}$	133 ns	266 ns
$\Gamma_{\text{sc}}(I = 0.5I_0)$	$9.45 \cdot 10^6 \text{ 1/s}$	
$\Gamma_{\text{sc}}(I = I_0)$	$1.425 \cdot 10^7 \text{ 1/s}$	
$\bar{n}_{\text{sc}}(0.5I_0)$	1.3	2.6
$\bar{n}_{\text{sc}}(I_0)$	1.9	3.9

by the corresponding scattering rate for I_{laser} , the mean number of scattered photons \bar{n}_{sc} is obtained. As shown in Tab. 5.3, this number is 1.3 and 1.9 for ODR1 and twice as much for ODR2. The velocity change per excitation is $\delta v = h\nu_{\text{c/a}}/(mc) \approx 0.146 \text{ m/s}$, resulting in a center frequency shift towards higher laser frequencies of $\partial\nu_{\text{c/a}}/\partial v \cdot \delta v \approx 0.65 \text{ MHz}$ per excitation and emission cycle. Hence, theoretically, an increase of the observed rest-frame frequency and of the frequency difference between ODR1 and ODR2 is expected for increasing laser intensity. This effect has been investigated by varying the laser intensity and looking for a systematic shift of the extracted rest-frame transition frequency. In all cases the intensity was the same for both laser beams. Measurements were performed under optimized conditions regarding beam overlap. However, even though the alignment has been checked for the different measurements, slight deviations within the laser beam alignment uncertainty of $\Delta\nu_{\text{VD}} = 1.7 \text{ MHz}$ are possible due the neutral density filters which were used to vary the laser intensities. They were placed directly behind the laser system which can lead to non-negligible laser beam shifts in the beamline, when they are slightly moved, due to the long distances between the filter and the beamline. All other conditions were similar as those described in the previous section. The result for the two mirrors in the ODRs (black squares and red circles) together with the difference between the two mirrors (blue open circles) is presented in Fig. 5.7. The extracted

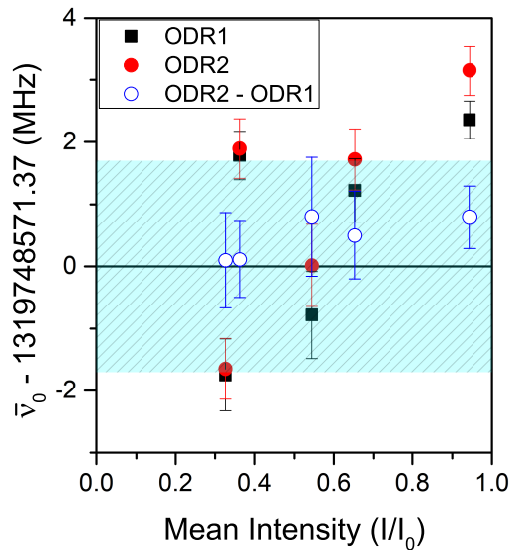


Figure 5.7: Rest-frame frequency determination (black squares and red circles) and the difference between the two optical detection regions (ODR) (blue open circles) for various laser intensities. A linear behavior as expected from theory is not observed.

frequencies scatter substantially stronger than expected from their statistical uncertainty which can be explained by the neutral density filter as mentioned above. Nevertheless, they agree within the laser beam alignment uncertainty of $\Delta\nu_{\text{VD}} = 1.7 \text{ MHz}$ indicated by the shaded blue area. Since this is only the 1σ uncertainty, it is reasonable that the scatter of the data point for $I/I_0 \approx 0.95$ is due to statistics. The same holds for the difference of the two frequencies obtained for each of the ODRs.

However, all measurements from Sec. 5.2.2 have been carried out with $I \leq 0.65I_0$ and a systematic shift from photon recoil is negligible with the current statistical uncertainty and the main systematic uncertainty $\Delta\nu_{\text{VD}}$. Therefore, no additional uncertainty for $\Delta\nu_{\text{recoil}}$ is considered.

Voltage difference δU

In CLS, the ions are brought in resonance with the fixed frequency laser by changing their kinetic energy with a tunable voltage applied at the ODR. Typically, the laser frequencies are not perfectly tuned to address exactly the same kinetic energy. However, the residual voltage difference δU between the two resonances can be compensated during analysis through Eq. (2.55) as explained in Sec. 2.4. However, this only works if the electric potential seen by the ions inside the ODR is the same for both laser directions. A reason for a possible difference is electric field penetration into the mirrors. The penetration depends roughly linearly on the ODR potential and therefore on the position of the resonances in voltage space. According to SIMION simulations, the potential on the beam axis of the ODR can differ up to 0.2 % from the applied voltage. Hence, the voltage difference δU could also differ by the same amount, introducing a systematic shift in Eq. (2.55).

In order to reduce this effect, care was taken that the voltage difference during the experiment was always smaller than 0.2 V which should limit the frequency uncertainty from field penetration (FP) to $\Delta\nu_{\text{FP}} = 0.2 \text{ V} \cdot 0.002 \cdot 172 \text{ MHz/V} < 0.07 \text{ MHz}$. Furthermore, the first mirror in the ODR has a metallic grid mounted towards the PMTs in order to prevent field penetration completely. Unfortunately, the second mirror did not have such a grid during the experiment. Therefore, an experimental check was performed: The laser frequencies were tuned such that the voltage difference δU between the resonances in the two directions were increased by a factor of 40, i.e., up to 8 V. The changes of the rest-frame frequencies determined in the two ODRs with respect to the result of the average of the measurements under standard conditions are plotted in the upper part of Fig. 5.8, while their differences are shown in the lower part. For the former, no clear dependency is visible due to the typical scattering within $\Delta\nu_{\text{VD}}$ (shaded blue area) and all values agree within their statistical uncertainties. This is also the case for the difference between the mirror systems. Therefore, this effect is negligible in comparison to the statistical uncertainty and $\Delta\nu_{\text{VD}}$.

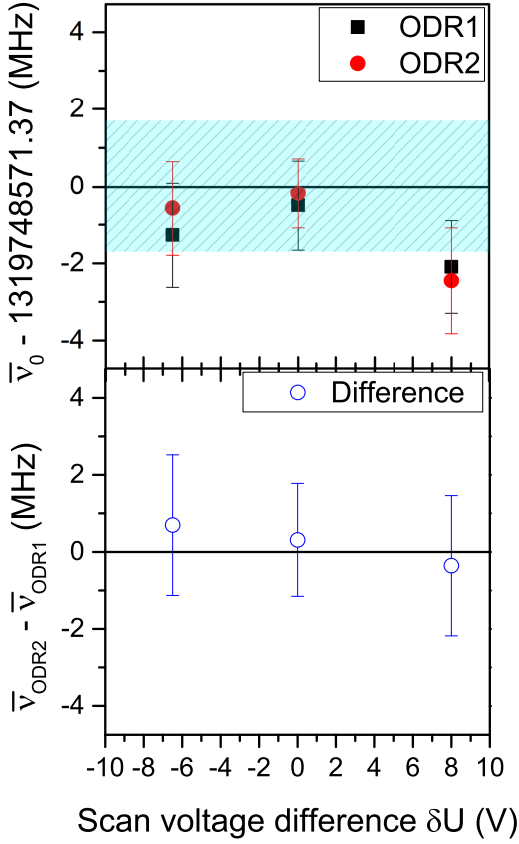


Figure 5.8: Transition frequencies $\bar{\nu}_0$ determined for several scan voltage differences δU . The absolute values for ODR1 (black squares) and ODR2 (red circles) as well as their difference (blue open circles in the lower panel) agree within their uncertainties.

Laser polarization and Zeeman splitting

Circularly polarized light can systematically shift the resonance frequency due to the Zeeman splitting in a residual magnetic field as explained in Sec. 2.4.4. A systematic comparison of the rest-frame transition frequency determination with linear and circular polarized laser light was therefore carried out in the $1s2s\ ^3S_1 \rightarrow 1s2p\ ^3P_0$ transition where the shift is expected to be 2.8 MHz/G. For the geomagnetic field $B_{\text{earth}} \approx 0.5$ G inside of the ODR, this would result in a systematic shift of 1.4 MHz. The result of the single frequency measurements is depicted in Fig. 5.9. Additionally, the mean value and the standard error of the mean (SEM) of each section is shown as two shaded areas. No systematic shift is visible due to the large scattering of the data points. The reason for the large scatter is the smaller SNR of the $1s2s\ ^3S_1 \rightarrow 1s2p\ ^3P_0$ transition due to smaller line intensity and strong drifts of the ion beam position during the measurements. With a new electron cathode and stable ion-source conditions, this effect could be investigated again in the future to check the influence of the residual earth's magnetic field to the $1s2s\ ^3S_1 \rightarrow 1s2p\ ^3P_2$ transition in $^{12}\text{C}4+$. However, this effect is neglected in the further analysis since only linear polarized light was used for the reference measurements which cannot shift the determined rest-frame frequency.

In summary, the main systematic uncertainty $\Delta\nu_{\text{sys}}$ is given by $\Delta\nu_{\text{VD}} = 1.7$ MHz which emerges

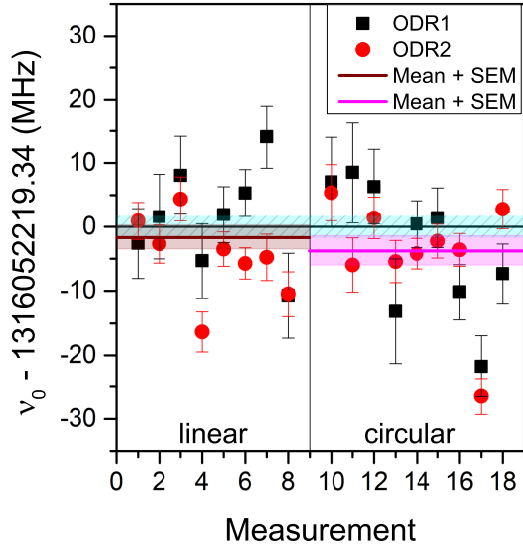


Figure 5.9: Comparison between transition frequency determinations in the $1s2s\ ^3S_1 \rightarrow 1s2p\ ^3P_0$ transition using linearly (left) and circularly (right) polarized laser light. The mean value and the standard error of the mean of each section is shown as two shaded areas. A systematic shift (see Sec. 2.4.4) of 1.4 MHz is expected but not visible due to the large scattering of the individual data points.

from a possible residual misalignment of the two laser beams in combination with the ion beam divergence. It is small enough to achieve the targeted precision of < 2 MHz. However, this could be improved in a future experiment through saturation spectroscopy with fast ions as demonstrated in [95] or optical pumping if a hyperfine structure is present [96]. First attempts have been started in [97]. Hereby it is ensured that both lasers interact with the same ions. The uncertainties caused by a misalignment between both laser beams will then reduce to Eq. (2.42) since both lasers will then definitely interact with ions of the same velocity. This will induce an uncertainty reduction by more than one order of magnitude, but also has experimental drawbacks as will be explained in the outlook.

5.2.2 $^3S_1 \rightarrow ^3P_J$ rest-frame transition frequencies

The $^3S_1 \rightarrow ^3P_J$ transitions were recorded repeatedly on different days always with an independent alignment procedure to compensate day-to-day drifts. The number of single measurements are $n(^3P_2) = 108$, $n(^3P_1) = 68$ and $n(^3P_0) = 28$ for the transition from the $1s2s\ ^3S_1$ to the respective fine-structure state. All measurements were evaluated separately for ODR1 and ODR2 and are shown in Fig. 5.10 relative to the weighted average $\bar{\nu}_0$ from all measurements of the respective transition. The blue shaded area marks the combined statistical and systematic uncertainty of each transition. The corresponding numerical values are listed in Tab. 5.4 with the statistical uncertainty $\Delta\nu_{\text{stat}}$ indicated in the first two rows. Since both values for the two mirrors agree within their statistical uncertainties, the final value $\bar{\nu}_0$ is the weighted average of all single ODR1 and ODR2 frequencies and given in the last row. Here, the bracket is the total 1σ uncertainty

$$\Delta\bar{\nu}_0 = \sqrt{\Delta\nu_{\text{stat}}^2 + \Delta\nu_{\text{sys}}^2}$$

including the systematic uncertainty $\Delta\nu_{\text{sys}} = \Delta\nu_{\text{VD}} = 1.7$ MHz as derived in Sec. 5.2.1.

The accuracy of all transitions is mainly limited by the systematic uncertainty. Only the

uncertainty of the $1s2s\ ^3S_1 \rightarrow 1s2p\ ^3P_0$ transition could be reduced by 200 kHz through an improvement of the statistical uncertainty. Possible solutions are more measurement repetitions, an increase in the signal-to-noise ratio of the resonance spectra and a reduction of the ν_0 scattering by using a new EBIS electron cathode. Nevertheless, the uncertainties $\Delta\bar{\nu}_0$ are smaller than the targeted accuracy of 2 MHz in all transitions which is an enhancement of more than three orders of magnitude compared to previous measurements reported in [98, 99]. A comparison between transition frequency values from theory and experiment is provided in Tab. 5.5 and illustrated in Fig. 5.11. It shows that also the most recent non-relativistic

Table 5.4: Results of the rest-frame frequency determination for ODR1 ($\bar{\nu}_{\text{ODR1}}$), ODR2 ($\bar{\nu}_{\text{ODR2}}$) and the weighted mean of all measurements ($\bar{\nu}_0$). The brackets in the first two rows denote the statistical uncertainties only, while in the last row the total uncertainties including the systematical uncertainty of $\Delta\nu_{\text{VD}} = 1.7$ MHz are given. All values are in MHz.

	$1s2s\ ^3S_1 \rightarrow 1s2p\ ^3P_2$	$1s2s\ ^3S_1 \rightarrow 1s2p\ ^3P_1$	$1s2s\ ^3S_1 \rightarrow 1s2p\ ^3P_0$
$\bar{\nu}_{\text{ODR1}}$	1 319 748 571.37(20)	1 315 677 193.06(58)	1 316 052 219.5(13)
$\bar{\nu}_{\text{ODR2}}$	1 319 748 571.38(20)	1 315 677 192.64(53)	1 316 052 219.3(13)
$\bar{\nu}_0$	1 319 748 571.37(171)	1 315 677 192.77(174)	1 316 052 219.34(194)

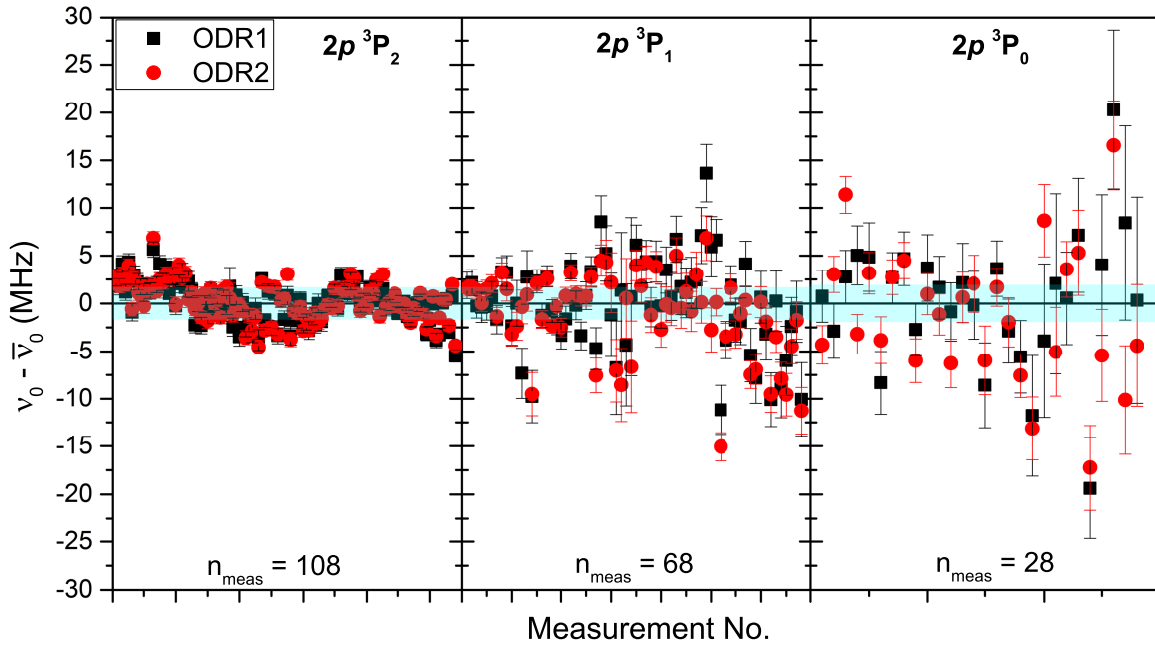


Figure 5.10: Single frequency measurements of the $1s2s\ ^3S_1 \rightarrow 1s2p\ ^3P_J$ transitions relative to the weighted mean $\bar{\nu}_0$ with their statistical uncertainty. All spectra have been evaluated separately for ODR1 (black squares) and ODR2 (red dots). The shaded blue area indicates the combined uncertainty $\Delta\bar{\nu}_0$.

QED calculations [32] refined their accuracy by one order of magnitude. The theory values agree well within their stated uncertainties with the experimental value from this work. The $1s2s\ ^3S_1 \rightarrow 1s2p\ ^3P_1$ transition has the largest uncertainty due to fine-structure mixing of the $2p\ ^1P_1$ and $2p\ ^3P_1$ state since they have the same angular momentum and parity. Therefore, they have to be treated as quasidegenerate levels in second-order perturbation theory which results in larger uncertainties [32].

Theory made significant progress over the last years and surpassed the experimental knowledge. With the improved measurements presented here, the improved theory has been tested experimentally for the first time and experimental accuracy has exceeded that of theory again by two orders of magnitude. Thus, the direct exploration of nuclear charge radii is now only limited by theory as will be discussed below.

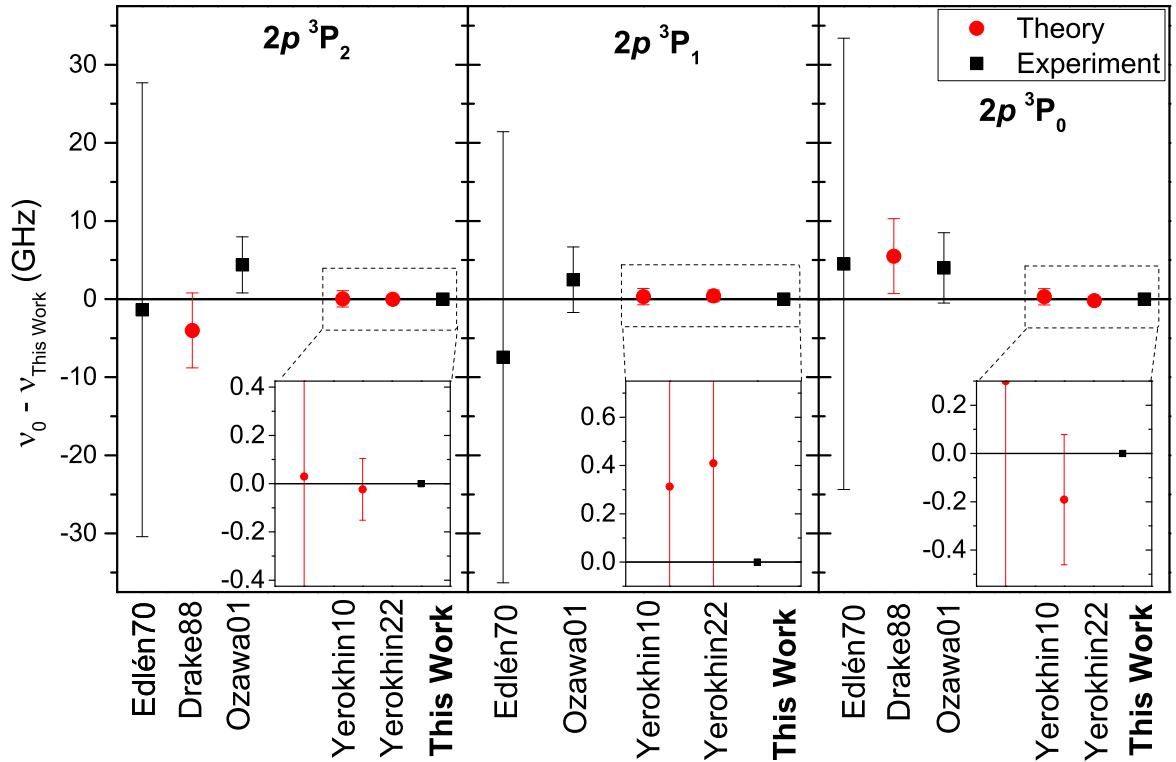


Figure 5.11: Illustration of Tab. 5.5 relative to the frequencies acquired in this work. The experimental accuracy has been improved by more than three orders of magnitude compared to the so-far most precise measurement by Ozawa *et al.* [98]. Also theory improved by an order of magnitude in a recent publication [32] compared to [49], but it is still two orders of magnitude worse than the experimental accuracy. The uncertainty of this work is not visible on this scale.

Table 5.5: Rest-frame transition frequency comparison between literature values and this work. All values are in GHz.

$1s2s\ ^3S_1 \rightarrow 1s2p\ ^3P_2$	$1s2s\ ^3S_1 \rightarrow 1s2p\ ^3P_1$	$1s2s\ ^3S_1 \rightarrow 1s2p\ ^3P_0$	
1 319 747(29)	1 315 669(29)	1 316 056(29)	[99] (Exp.)
1 319 744.6(48)	1 315 076.2(48)	1 316 057.7(48)	[100] (Theory)
1 319 753.0(36)	1 315 679.7(42)	1 316 056.2(45)	[98] (Exp.)
1 319 748.6(10)	1 315 677.5(10)	1 316 052.5(10)	[49] (Theory)
1 319 748.55(13)	1 315 677.60(75)	1 316 052.03(27)	[32] (Theory)
1 319 748.5714(17)	1 315 677.1928(17)	1 316 052.2193(19)	This work

5.2.3 Fine-structure splitting

The $2p\ ^3P_J \rightarrow 2p\ ^3P_{J'}$ fine-structure splitting $\nu_{JJ'}$ in helium and helium-like ions is a valuable tool to test QED theory. Alternatively, accurate measurements of $\nu_{JJ'}$ can be used together with QED calculations to determine the fine-structure constant α as demonstrated, e.g., in [52]. Here, remarkable calculations have been completed using NRQED up to the order of $m\alpha^7$. This led to a very good agreement with available experimental data of He [101, 102], Li^+ [103], Be^{2+} [104], B^{3+} [105], N^{5+} [106] and F^{7+} [107]. Furthermore, the determination of α to an accuracy of 31 part-per-billion (ppb) was achieved together with experimental He data [101]. The main contribution to the uncertainty of α stems from the QED terms of the next missing order $m\alpha^8$. However, it was suggested that a precise measurement of the fine-structure splitting in $^{12}\text{C}^{4+}$ could help to estimate the size of the $m\alpha^8$ contribution and thereby reduce the corresponding uncertainty of α by a factor of 2 [52].

Tab. 5.6 holds the values of fine-structure splitting directly from the difference of the $1s2s\ ^3S_1 \rightarrow 1s2p\ ^3P_J$ transitions acquired in this work and the theory values from [52]. The denoted number for this work is the propagated error of the total uncertainty in Tab. 5.4. The uncertainty of the theory is estimated from the missing $m\alpha^8$ contributions. Therefore, the $m\alpha^8$ contribution can be derived from the difference of the experimental and theory value with the assumption that the theory value is complete to $m\alpha^7$. This difference is also listed in Tab. 5.6 as $m\alpha^8$ contribution.

Table 5.6: Fine-structure splitting of the $1s2p\ ^3P_J$ levels in $^{12}\text{C}^{4+}$ acquired from this work and theory [52]. Due to the high-precision values from this work, the $m\alpha^8$ contribution that is missing in theory can be determined as difference between experiment and theory. All values are in MHz.

(J, J')	This work	Theory [52]	$m\alpha^8$ contr.
(0, 1)	−375 026.5(25)	−374 996.3(480)	−30.2(25)
(0, 2)	3 696 352.1(25)	3 696 343.5(100)	8.6(25)

5.3 All-optical nuclear charge radius of ^{12}C

The nuclear charge radius R_C of ^{12}C is already known on a 0.4 % level from elastic electron scattering [33–36] and on a 0.08 % level from muonic X-ray spectroscopy [37, 38]. Therefore, this nucleus is a perfect candidate for a proof-of-principle of the all-optical nuclear charge radius determination. Here, the nuclear charge radius is obtained through

$$R_C = \langle r^2 \rangle^{1/2} = \sqrt{\frac{\nu_{0,\text{exp}} - \nu_{0,\text{point}}}{F}} \quad (5.2)$$

with the experimental transition frequency $\nu_{0,\text{exp}}$, the corresponding theoretical transition frequency for a point-like nucleus $\nu_{0,\text{point}}$ and the field-shift factor F in this transition. $\nu_{0,\text{point}}$ and F are provided by non-relativistic (NR) QED calculations and can be extracted from the latest publication [32]. All numerical values needed for the all-optical charge radius determination together with the results for R_C are listed in Tab. 5.7.

A nuclear charge radius can be calculated for each measured transition, but the $1s2s\ ^3S_1 \rightarrow 1s2p\ ^3P_2$ transition delivers the most accurate R_C of all transitions since here the theory value $\nu_{0,\text{point}}$ has the smallest uncertainty. The uncertainty ΔR_C in all transitions is completely dominated by the theoretical uncertainty, which limits the accuracy for an all-optical R_C to 4.8 %. A comparison between the all-optical approach and previous data is depicted in Fig. 5.12. It illustrates that the all-optical determination is not yet competitive with other methods despite significant progress in experiment and theory. A refinement of the NRQED calculations by one order of magnitude would reduce the uncertainty and the accuracy would be comparable with that of electron scattering. An improvement by two orders of magnitude would even surpass the reported accuracy from the muonic measurement from Ruckstuhl *et al.* [38].

Hence, this work laid the experimental foundation for a precise all-optical determination of the nuclear charge radius of ^{12}C . Once theory is improved, the most accurate charge radius for this nucleus can be extracted from the data presented in this work, which is improved by more than 3 orders of magnitude compared to previous experiments. Furthermore, the rest-frame transition frequency measurements in $^{12}\text{C}^{4+}$ can be used together with ongoing measurements in $^{13}\text{C}^{4+}$ for a conventional determination of the mean-square charge radius difference $\delta\langle r^2 \rangle^{12,13}$ between ^{12}C and ^{13}C which has not been measured so far by laser spectroscopy.

Table 5.7: Parameters for the all-optical nuclear charge radius determination of ^{12}C . $\nu_{0,\text{point}}$ and F are taken from [32].

	$1s2s\ ^3S_1 \rightarrow 1s2p\ ^3P_2$	$1s2s\ ^3S_1 \rightarrow 1s2p\ ^3P_1$	$1s2s\ ^3S_1 \rightarrow 1s2p\ ^3P_0$
$\nu_{0,\text{exp}}$ (GHz)	1 319 748.5714(17)	1 315 677.1928(17)	1 316 052.2193(19)
$\nu_{0,\text{point}}$ (GHz)	1 319 749.83(13)	1 315 678.89(75)	1 316 053.32(27)
F (GHz/fm ²)	0.2115	0.2115	0.2113
R_C (fm)	2.45(12)	2.83(63)	2.28(28)

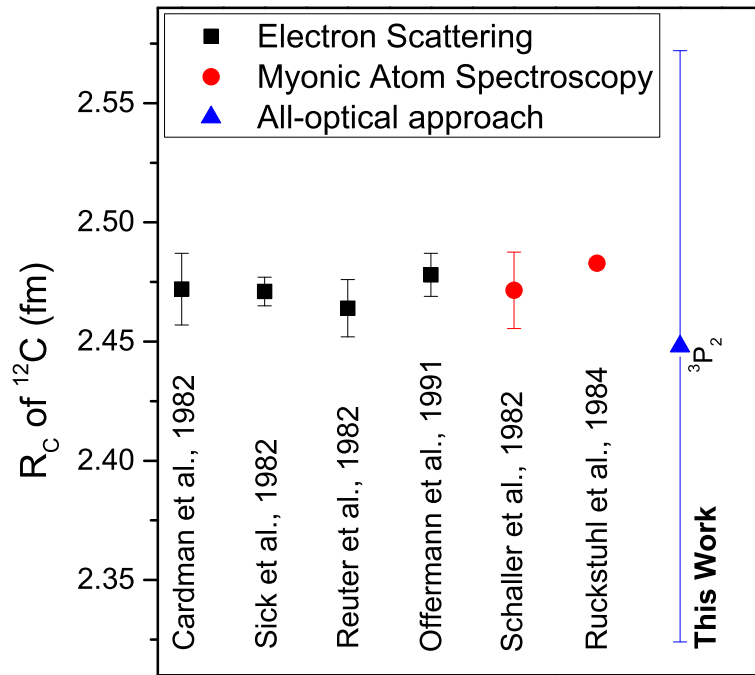


Figure 5.12: Comparison of all available ^{12}C charge radii. Only the most precise value of the all-optical approach which has been extracted from the $1s2s\ ^3S_1 \rightarrow 1s2p\ ^3P_2$ transition is plotted since the statistical accuracy in the other two transitions is worse. The value from this work agrees with previous data but the theory-limited uncertainty is still too large to compete with the other methods.

6 Summary and outlook

Laser spectroscopy of $^{12}\text{C}^{4+}$ was performed at the Collinear Apparatus for Laser Spectroscopy and Applied Science (COALA) [80], situated at the Institute for Nuclear Physics at the Technical University Darmstadt. Namely, the $1s2s\ ^3\text{S}_1 \rightarrow 1s2p\ ^3\text{P}_J$ transition frequencies were measured with better than 2 MHz precision. Collinear laser spectroscopy (CLS) was chosen since the 21 ms lifetime of the $1s2s\ ^3\text{S}_1$ state in C^{4+} requires a fast measurement cycle from the production of the ions to the laser spectroscopic investigation.

In order to enable CLS on highly charged ions, numerous improvements and upgrades of the COALA beamline were realized within this work. First, a new electron beam ion source (EBIS) including a Wien-filter for charge/mass separation was installed and commissioned at COALA in order to produce the highly charged C^{4+} ions. Therefore a new switchyard including additional beam diagnostics was designed, built and installed. It allows to keep up to three ion sources installed in parallel to quickly switch between different projects. Additionally, the existing beam diagnostic stations were upgraded by implementing new iris diaphragms and MCP stacks that facilitate the optimization of the ion beam shape and the ion and laser beam superposition.

An EBIS has two operation modes, namely the bunched and the continuous mode. The production parameters of both modes were optimized with respect to the ion yield and the properties of the laser resonance spectrum like their width and signal-to-noise ratio. It turned out that the continuous beam mode produces the narrowest resonances with a full width at half maximum of 170 MHz which results in statistical uncertainties in the center frequency determination of roughly 1 MHz.

In order to extract the rest-frame transition frequency from a Doppler-shifted laboratory-frame resonance spectrum, the ion velocity must be known to correct for the Doppler shift. Since the starting potential of the ions in an EBIS is only roughly known, this would strongly limit the accuracy of the rest-frame frequency. An uncertainty of only 1 V in the 10.5 keV starting potential would translate into an uncertainty of 170 MHz in the rest-frame transition frequency determination. To overcome this limit and to become largely independent of the ion velocity, quasi-simultaneous collinear and anticollinear laser spectroscopy was exploited at COALA as demonstrated in [83, 84, 96]. This technique is based on collinear and anticollinear measurements with well-aligned laser beams which are performed in fast iteration. The rest-frame transition frequency is then given by the geometric mean of the collinear and anticollinear laboratory-frame resonance frequency and only changes of the potentials between the recordings of the collinear and anticollinear spectra and misalignments between the ion and laser beams contribute to the Doppler-shift uncertainty. Overall, a combined statistical and systematic uncertainty of less than 2 MHz for all $1s2s\ ^3\text{S}_1 \rightarrow 1s2p\ ^3\text{P}_J$ transition frequencies in $^{12}\text{C}^{4+}$ was achieved. The dominant uncertainty arose from the superposition of the two

laser beams in combination with the spatial velocity distribution. Thereby, both lasers can probe different ions with slightly different ion velocities when the two lasers are not perfectly aligned, which results in a systematic shift of the rest-frame transition frequency. This can be improved with saturation spectroscopy since this ensures a simultaneous interaction of both lasers with the same ions. First attempts have been started in [97], but have not yet delivered more precise results. The main challenges are the increased laser background of two lasers, the lack of laser power to strongly saturate the transition, and the necessity to scan the laser instead of Doppler tuning. Especially the laser scan is currently rather slow in comparison to the remaining drift of the ions starting potential which smears out the resonance. However, all points should be solvable with some effort.

The achieved precision in this work is an improvement by more than three orders of magnitude compared to previous experiments [98, 99] and tests non-relativistic QED calculations of two-electron systems at an unprecedented level of precision for elements beyond lithium for the first time. Excellent agreement with NRQED calculations of the $1s2s\ ^3S_1 \rightarrow 1s2p\ ^3P_J$ transition frequencies is found. The results enable the estimation of the next missing order $m\alpha^8$ of the fine-structure NRQED calculations for the first time. Moreover, the nuclear charge radius of ^{12}C was determined exclusively from atomic structure calculations and the measured frequencies of the individual fine-structure transitions from this work. This all-optical approach results in $R_c = 2.45(12)$ fm and agrees with previous values from elastic electron scattering and muonic atom spectroscopy, but its uncertainty is not yet competitive with that of the other techniques despite the significant progress achieved in experiment and theory. But the experimental uncertainty provided here will allow for a competitive and even surpassing determination of R_c once theory is further improved by one to two orders of magnitude. Thus, the experimental foundation for a precise all-optical determination of the nuclear charge radius of ^{12}C is now firmly established.

Additionally, the rest-frame transition frequency measurements in $^{12}\text{C}^{4+}$ can be combined with ongoing measurements in $^{13}\text{C}^{4+}$ for a conventional determination of the mean-square charge radius difference $\delta\langle r^2 \rangle^{12,13}$ between ^{12}C and ^{13}C which has not been measured so far by laser spectroscopy. This will enable a comparison between conventional mass and field-shift calculations and the new all-optical approach through the determination of $\delta\langle r^2 \rangle^{12,13}$ from the isotope shift and from the all-optical radii $R_c(^{12}\text{C})$ and $R_c(^{13}\text{C})$. Both ways must provide the same result and would additionally verify the theory. This is the first step of the planned "pathway" to the investigation of the proton-halo candidate ^8B which is illustrated in Fig. 6.1. It consists of several laser spectroscopic measurements in neutral atoms or singly charged ions (black) and multiply charged ions (blue) of boron and beryllium which enables a consistency check (magenta) between the theory of helium-like systems (red) and conventional mass-shift calculations (green) performed with Hylleraas or explicitly correlated Gaussian (ECG) wavefunctions. The determination of $\delta\langle r^2 \rangle^{10,11}$ and $\delta\langle r^2 \rangle^{9,7}$ from the isotope shift in neutral boron [12] and singly ionized beryllium [108] from the respective isotope shifts have already been completed and the measurement of the isotope shift of ^8B is in preparation at the Argonne National Laboratory in Chicago, USA [31]. The investigation of the multiply charged ions will be continued at COALA. After the campaign with $^{13}\text{C}^{4+}$, it is planned to investigate $^{10,11}\text{B}^{2+}$ ($1s^2 2s\ ^2S_{1/2} \rightarrow 1s^2 2p\ ^2P_{1/2,3/2}$ at 206.5 nm) and $^{10,11}\text{B}^{3+}$ ($1s2s\ ^3S_1 \rightarrow 1s2p\ ^3P_J$ at 282 nm). These ions can easily be produced by feeding trimethyl borate ($\text{BO}_3\text{C}_3\text{H}_9$), which has

a high vapor pressure, into the EBIS. For Be^{2+} ($1s2s\ ^3S_1 \rightarrow 1s2p\ ^3P_J$ at 372 nm), the situation is different. Here, Be^+ must be produced with a different ion source first and then injected into the EBIS. This is a new procedure at COALA and has to be developed. However, the new switchyard constructed in this work has already been designed to allow for this procedure. The primary Be^+ source can be installed directly opposite to the EBIS, which should simplify the EBIS injection for the charge breeding of Be^{2+} . In the last step, the nuclear charge radius of ^8B and ^7Be will be obtained and the halo distance d_{halo} of ^8B will be extracted. This will enable a definite statement about the halo character of ^8B and serve as a strong test of nuclear halo effective field theory.

Finally, it should be noted that if the injection-breeding-ejection procedure can be realized and is sufficiently efficient, it could serve for online laser spectroscopy, e.g., of carbon isotopes for which currently no other laser spectroscopic scheme has been established.

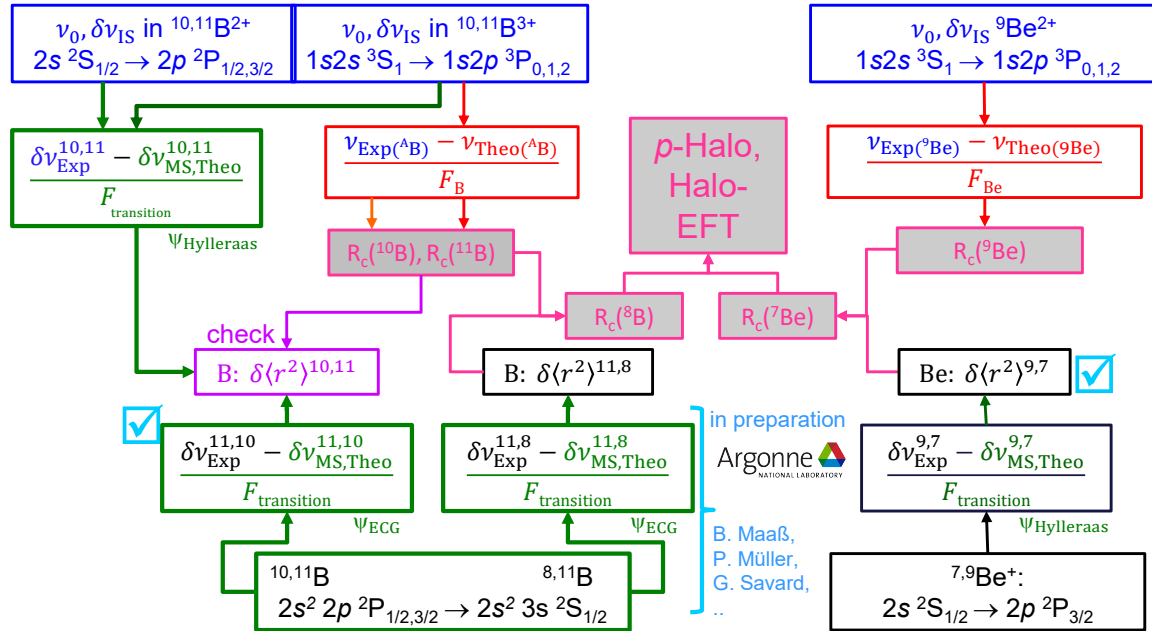


Figure 6.1: "Pathway" to the halo distance d_{halo} of ^8B . Several laser spectroscopic measurements in neutral atoms or singly charged ions (black) and multiply charged ions (blue) of boron and beryllium enable a consistency check (magenta) between the theory of helium-like systems (red) and conventional mass-shift calculations (green) performed with Hylleraas or explicitly correlated Gaussian (ECG) wavefunctions. The determination of $\delta\langle r^2 \rangle^{10,11}$ from neutral boron [12] and $\delta\langle r^2 \rangle^{9,7}$ from singly ionized beryllium [108] have already been completed. The measurement of the isotope shift of ^8B is in preparation at the Argonne National Laboratory in Chicago, USA [31]. The investigation of the multiply charged ions will be continued at COALA.

A Appendix

A.1 Spatial velocity distribution simulation

The influence of the spatial velocity distribution of an ion beam to the rest-frame determination in quasi-simultaneous collinear and anticollinear laser spectroscopy was identified as the main uncertainty in Sec. 5.2.1. This explanation has been supported by ion beam simulations with SIMION and subsequent numerical calculations/simulations in Python 3 in the following way:

1. **Simulation of an ion beam.** The trajectory of $2 \cdot 10^5$ $^{12}\text{C}^{4+}$ ions with a kinetic energy of $E_{\text{kin}} = (42000 \pm 4)$ eV through the switchyard has been simulated with SIMION (see Sec. 3.2 and Fig. 3.4). In an analysis plane at the exit of the switchyard (fixed z position), ion properties like the horizontal and vertical coordinates (x and y) and the velocity $\vec{v} = v \cdot \vec{i}$ have been saved in a comma-separated values (csv) data file. All subsequent calculations are completed with Python 3.
2. **Generation of laser beams.** For each ion position (x, y) , two corresponding laser beam intensities I/I_0 were calculated (collinear and anticollinear). Here, a Gaussian 2D distribution given by

$$\frac{I}{I_0}(x, y) = A \cdot e^{-\left(\frac{(x-x_0)^2}{2\sigma_x^2} + \frac{(y-y_0)^2}{2\sigma_y^2}\right)}$$

with the amplitude $A = 1$, the standard deviation $\sigma_x = \sigma_y = 0.5$ mm and the relative displacement coordinates $x_0^{\text{col}} - x_0^{\text{acol}} = 0.55$ mm and $y_0^{\text{col}} - y_0^{\text{acol}} = 0$ mm has been used. The divergence of the laser beam has been neglected and the laser beam vector has been assumed as $\vec{l}_{\text{c/a}} = (0, 0, \pm 1)^T$ for the collinear and anticollinear direction, respectively.

3. **Calculation of the angle between laser and ion beam.** The angle α between the two laser beams and the ions has been calculated through

$$\alpha_{\text{c/a}} = \arccos \frac{\vec{i} \cdot \vec{l}_{\text{c/a}}}{|\vec{i}| \cdot |\vec{l}_{\text{c/a}}|}.$$

4. **Calculation of the laboratory-frame transition frequency.** The laboratory-frame transition frequency $\nu_{\text{c/a}}$ has been calculated for each ion with Eq. (2.39) and the ion velocity v , the angle $\alpha_{\text{c/a}}$ and the rest-frame transition frequency $\nu_0 = 1319748571.4$ MHz.
5. **Calculation of the resonance spectrum.** A scattering rate is calculated for each ion with Eq. (2.58) within a laser scan range $\Delta = \nu - \nu_{\text{a/c}} = \pm 500$ MHz, and the relative intensity

I/I_0 and the Einstein coefficient for spontaneous decay $A_{ik} = 5.669 \cdot 10^7$ 1/s. The sum of all scattering rates for a respective laser frequency yields the resonance spectrum for the collinear and anticollinear direction.

6. **Fitting and evaluation.** The line-center frequencies $\nu_{c/a}^{\text{center}}$ of both resonance spectra is determined by fitting a Voigt profile to the simulated points. Then, the systematic shift is given by

$$\Delta\nu = \nu_0 - \sqrt{\nu_c^{\text{center}} \cdot \nu_a^{\text{center}}}.$$

This procedure has been used to demonstrate, that the divergence introduced by the switchyard can produce shifts in the same order of magnitude as seen in the experiment. Several plots of the steps above are depicted in Fig. A.1. The resulting shift for the parameters above is roughly 10 MHz, which is close to the 8.6 MHz in the experiment.

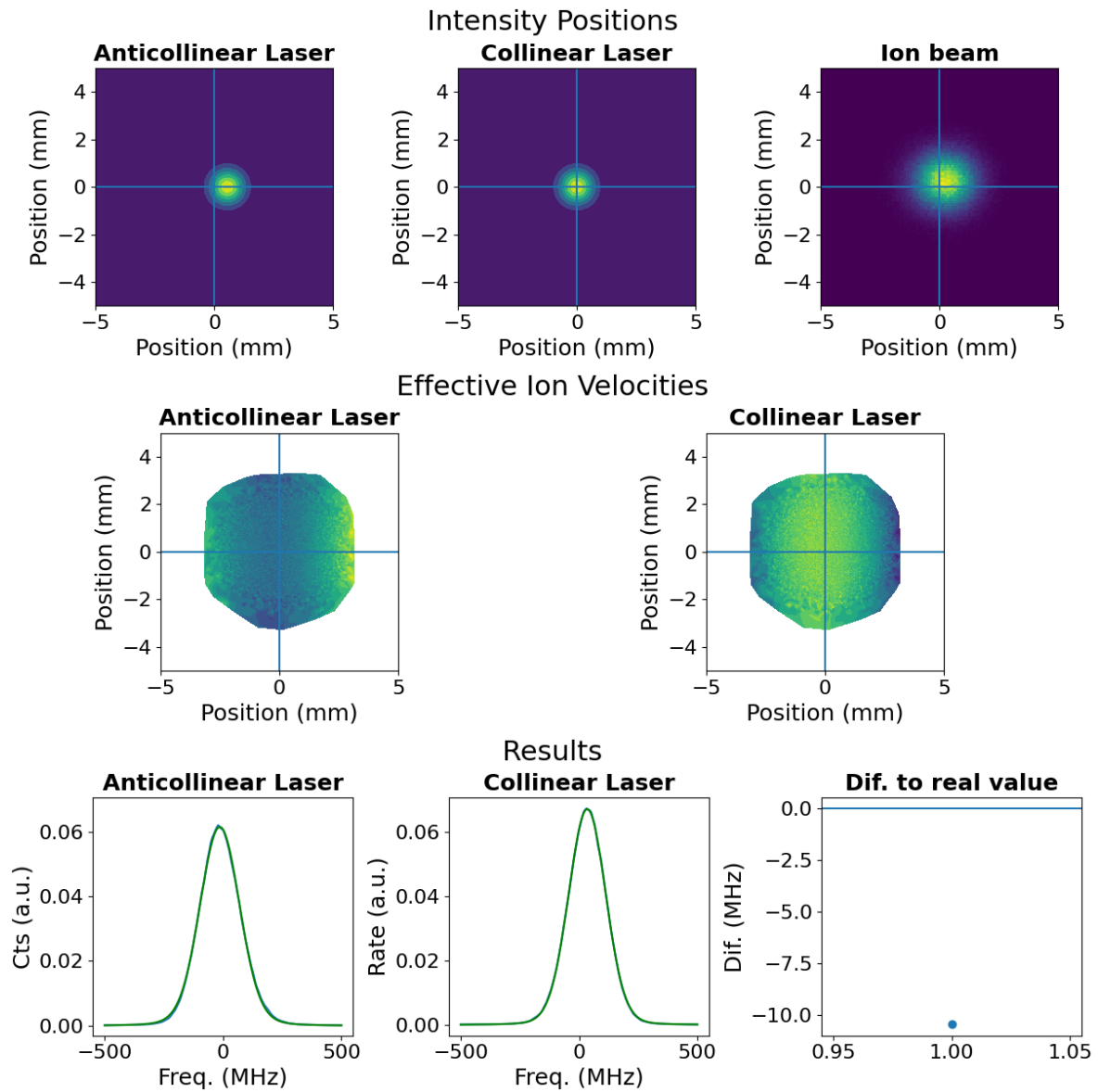


Figure A.1: Results of the simulation described in the text. The simulated shift of roughly 10 MHz has the order of magnitude of the observed experimental shift from Sec. 5.2.1.

Bibliography

- ¹E. Rutherford, “The scattering of α and β particles by matter and the structure of the atom”, The London, Edinburgh, and Dublin Philosophical Magazine and Journal of Science **21**, 669–688 (1911).
- ²N. Bohr, “I. On the constitution of atoms and molecules”, The London, Edinburgh, and Dublin Philosophical Magazine and Journal of Science **26**, 1–25 (1913).
- ³H. C. Urey, F. G. Brickwedde, and G. M. Murphy, “A hydrogen isotope of mass 2”, Phys. Rev. **39**, 164–165 (1932).
- ⁴W. E. Lamb and R. C. Retherford, “Fine Structure of the Hydrogen Atom by a Microwave Method”, Phys. Rev. **72**, 241–243 (1947).
- ⁵W. Pauli, “Zur Frage der theoretischen Deutung der Satelliten einiger Spektrallinien und ihrer Beeinflussung durch magnetische Felder”, Naturwissenschaften **12**, 741–743 (1924).
- ⁶H. Nagaoka, Y. Sugiura, and T. Mishima, “Binding of Electrons in the Nucleus of the Mercury Atom”, Nature **113**, 567–568 (1924).
- ⁷H. Casimir, “Über die hyperfeinstruktur des Europiums”, Physica **2**, 719–723 (1935).
- ⁸K. Blaum, J. Dilling, and W. Nörtershäuser, “Precision atomic physics techniques for nuclear physics with radioactive beams”, Physica Scripta **2013**, 014017 (2013).
- ⁹P. Campbell, I. Moore, and M. Pearson, “Laser spectroscopy for nuclear structure physics”, Progress in Particle and Nuclear Physics **86**, 127–180 (2016).
- ¹⁰X. F. Yang, S. J. Wang, S. G. Wilkins, and R. F. G. Ruiz, *Laser Spectroscopy for the Study of Exotic Nuclei*, published on arXiv.org: <https://arxiv.org/abs/2209.15228>, 2022.
- ¹¹D. T. Yordanov, L. V. Rodríguez, D. L. Balabanski, J. Bieroń, M. L. Bissell, K. Blaum, B. Cheal, J. Ekman, G. Gaigalas, R. F. Garcia Ruiz, G. Georgiev, W. Gins, M. R. Godefroid, C. Gorges, Z. Harman, H. Heylen, P. Jönsson, A. Kanellakopoulos, S. Kaufmann, C. H. Keitel, V. Lagaki, S. Lechner, B. Maaß, S. Malbrunot-Ettenauer, W. Nazarewicz, R. Neugart, G. Neyens, W. Nörtershäuser, N. S. Oreshkina, A. Papoulia, P. Pyykkö, P.-G. Reinhard, S. Sailer, R. Sánchez, S. Schiffmann, S. Schmidt, L. Wehner, C. Wraith, L. Xie, Z. Xu, and X. Yang, “Structural trends in atomic nuclei from laser spectroscopy of tin”, Communications Physics **3**, 107 (2020).
- ¹²B. Maaß, T. Hüther, K. König, J. Krämer, J. Krause, A. Lovato, P. Müller, K. Pachucki, M. Puchalski, R. Roth, R. Sánchez, F. Sommer, R. B. Wiringa, and W. Nörtershäuser, “Nuclear Charge Radii of $^{10,11}\text{B}$ ”, Phys. Rev. Lett. **122**, 182501 (2019).
- ¹³R. Hofstadter, “Electron Scattering and Nuclear Structure”, Rev. Mod. Phys. **28**, 214–254 (1956).

-
- ¹⁴L. A. Schaller, “Muonic atoms spectroscopy”, *Z. Physik C* **56**, S48–S58 (1992).
- ¹⁵M. Smith, M. Brodeur, T. Brunner, S. Ettenauer, A. Lapierre, R. Ringle, V. L. Ryjov, F. Ames, P. Bricault, G. W. F. Drake, P. Delheij, D. Lunney, F. Sarazin, and J. Dilling, “First Penning-Trap Mass Measurement of the Exotic Halo Nucleus ^{11}Li ”, *Phys. Rev. Lett.* **101**, 202501 (2008).
- ¹⁶C. Bachelet, G. Audi, C. Gaulard, C. Guénaut, F. Herfurth, D. Lunney, M. de Saint Simon, and C. Thibault, “New Binding Energy for the Two-Neutron Halo of ^{11}Li ”, *Phys. Rev. Lett.* **100**, 182501 (2008).
- ¹⁷I. Tanihata, H. Hamagaki, O. Hashimoto, Y. Shida, N. Yoshikawa, K. Sugimoto, O. Yamakawa, T. Kobayashi, and N. Takahashi, “Measurements of Interaction Cross Sections and Nuclear Radii in the Light p -Shell Region”, *Phys. Rev. Lett.* **55**, 2676–2679 (1985).
- ¹⁸T. Kobayashi, O. Yamakawa, K. Omata, K. Sugimoto, T. Shimoda, N. Takahashi, and I. Tanihata, “Projectile Fragmentation of the Extremely Neutron-Rich Nucleus ^{11}Li at 0.79 GeV/nucleon”, *Phys. Rev. Lett.* **60**, 2599–2602 (1988).
- ¹⁹H. Simon, D. Aleksandrov, T. Aumann, L. Axelsson, T. Baumann, M. J. G. Borge, L. V. Chulkov, R. Collatz, J. Cub, W. Dostal, B. Eberlein, T. W. Elze, H. Emling, H. Geissel, A. Grünschloss, M. Hellström, J. Holeczek, R. Holzmann, B. Jonson, J. V. Kratz, G. Kraus, R. Kulesa, Y. Leifels, A. Leistenschneider, T. Leth, I. Mukha, G. Münzenberg, F. Nickel, T. Nilsson, G. Nyman, B. Petersen, M. Pfützner, A. Richter, K. Riisager, C. Scheidenberger, G. Schrieder, W. Schwab, M. H. Smedberg, J. Stroth, A. Surowiec, O. Tengblad, and M. V. Zhukov, “Direct Experimental Evidence for Strong Admixture of Different Parity States in ^{11}Li ”, *Phys. Rev. Lett.* **83**, 496–499 (1999).
- ²⁰Z.-T. Lu, P. Mueller, G. W. F. Drake, W. Nörtershäuser, S. C. Pieper, and Z.-C. Yan, “Colloquium: Laser probing of neutron-rich nuclei in light atoms”, *Rev. Mod. Phys.* **85**, 1383–1400 (2013).
- ²¹T. Minamisono, T. Ohtsubo, I. Minami, S. Fukuda, A. Kitagawa, M. Fukuda, K. Matsuta, Y. Nojiri, S. Takeda, H. Sagawa, and H. Kitagawa, “Proton halo of ^8B disclosed by its giant quadrupole moment”, *Phys. Rev. Lett.* **69**, 2058–2061 (1992).
- ²²T. Sumikama, T. Nagatomo, M. Ogura, T. Iwakoshi, Y. Nakashima, H. Fujiwara, K. Matsuta, T. Minamisono, M. Fukuda, and M. Mihara, “Electric quadrupole moment of the proton halo nucleus ^8B ”, *Phys. Rev. C* **74**, 024327 (2006).
- ²³W. Schwab, H. Geissel, H. Lenske, K.-H. Behr, A. Brünle, K. Burkard, H. Irnich, T. Kobayashi, G. Kraus, A. Magel, G. Münzenberg, F. Nickel, K. Riisager, C. Scheidenberger, B. M. Sherrill, T. Suzuki, and B. Voss, “Observation of a proton halo in ^8B ”, *Z. Physik A* **350**, 283–284 (1995).
- ²⁴J. H. Kelley, S. M. Austin, A. Azhari, D. Bazin, J. A. Brown, H. Esbensen, M. Fauerbach, M. Hellström, S. E. Hirzebruch, R. A. Kryger, D. J. Morrissey, R. Pfaff, C. F. Powell, E. Ramakrishnan, B. M. Sherrill, M. Steiner, T. Suomijärvi, and M. Thoennessen, “Study of the Breakup Reaction $^8\text{B} \rightarrow ^7\text{Be} + p$: Absorption Effects and $E2$ Strength”, *Phys. Rev. Lett.* **77**, 5020–5023 (1996).

-
- ²⁵F. Negoita, C. Borcea, F. Carstoiu, M. Lewitowicz, M. G. Saint-Laurent, R. Anne, D. Bazin, J. M. Corre, P. Roussel-Chomaz, V. Borrel, D. Guillemaud-Mueller, H. Keller, A. C. Mueller, F. Pougheon, O. Sorlin, S. Lukyanov, Y. Penionzhkevich, A. Fomichev, N. Skobelev, O. Tarasov, Z. Dlouhy, and A. Kordyas, “ ^8B proton halo via reaction and breakup cross section measurements”, *Phys. Rev. C* **54**, 1787–1797 (1996).
- ²⁶M. Smedberg, T. Baumann, T. Aumann, L. Axelsson, U. Bergmann, M. Borge, D. Cortina-Gil, L. Fraile, H. Geissel, L. Grigorenko, M. Hellström, M. Ivanov, N. Iwasa, R. Janik, B. Jonson, H. Lenske, K. Markenroth, G. Münzenberg, T. Nilsson, A. Richter, K. Riisager, C. Scheidenberger, G. Schrieder, W. Schwab, H. Simon, B. Sitar, P. Strmen, K. Sümmerer, M. Winkler, and M. Zhukov, “New results on the halo structure of ^8B ”, *Phys. Lett. B* **452**, 1–7 (1999).
- ²⁷A. Dobrovolsky, G. Korolev, A. Inglessi, G. Alkhazov, G. Colò, I. Dillmann, P. Egelhof, A. Estradé, F. Farinon, H. Geissel, S. Ilieva, Y. Ke, A. Khanzadeev, O. Kiselev, J. Kurcewicz, X. Le, Y. Litvinov, G. Petrov, A. Prochazka, C. Scheidenberger, L. Sergeev, H. Simon, M. Takechi, S. Tang, V. Volkov, A. Vorobyov, H. Weick, and V. Yatsoura, “Nuclear-matter distribution in the proton-rich nuclei ^7Be and ^8B from intermediate energy proton elastic scattering in inverse kinematics”, *Nuclear Physics A* **989**, 40–58 (2019).
- ²⁸T. Stovall, J. Goldemberg, and D. Isabelle, “Coulomb form factors of ^{10}B and ^{11}B ”, *Nuclear Physics* **86**, 225–240 (1966).
- ²⁹A. Cichocki, J. Dubach, R. S. Hicks, G. A. Peterson, C. W. de Jager, H. de Vries, N. Kalantar-Nayestanaki, and T. Sato, “Electron scattering from ^{10}B ”, *Phys. Rev. C* **51**, 2406–2426 (1995).
- ³⁰A. Olin, P. Poffenberger, G. Beer, J. MacDonald, G. Mason, R. Pearce, and W. Sperry, “Measurement of pionic and muonic X-rays in $^{10,11}\text{B}$ ”, *Nuclear Physics A* **360**, 426–434 (1981).
- ³¹B. Maaß, “Laser spectroscopy of the boron isotopic chain”, en, PhD thesis (Technische Universität Darmstadt, Darmstadt, Feb. 2020).
- ³²V. A. Yerokhin, V. Patkoš, and K. Pachucki, “QED calculations of energy levels of heliumlike ions with $5 \leq Z \leq 30$ ”, *Phys. Rev. A* **106**, 022815 (2022).
- ³³L. Cardman, J. Lightbody, S. Penner, S. Fivozinsky, X. Maruyama, W. Trower, and S. Williamson, “The charge distribution of ^{12}C ”, *Phys. Lett. B* **91**, 203–206 (1980).
- ³⁴I. Sick, “Precise nuclear radii from electron scattering”, *Phys. Lett. B* **116**, 212–214 (1982).
- ³⁵W. Reuter, G. Fricke, K. Merle, and H. Miska, “Nuclear charge distribution and rms radius of ^{12}C from absolute elastic electron scattering measurements”, *Phys. Rev. C* **26**, 806–818 (1982).
- ³⁶E. A. J. M. Offermann, L. S. Cardman, C. W. de Jager, H. Miska, C. de Vries, and H. de Vries, “Energy dependence of the form factor for elastic electron scattering from ^{12}C ”, *Phys. Rev. C* **44**, 1096–1117 (1991).
- ³⁷L. Schaller, L. Schellenberg, T. Phan, G. Piller, A. Ruetschi, and H. Schnewly, “Nuclear charge radii of the carbon isotopes ^{12}C , ^{13}C and ^{14}C ”, *Nuclear Physics A* **379**, 523–535 (1982).

-
- ³⁸W. Ruckstuhl, B. Aas, W. Beer, I. Beltrami, K. Bos, P. Goudsmit, H. Leisi, G. Strassner, A. Vacchi, F. De Boer, U. Kiebe, and R. Weber, “Precision measurement of the 2p-1s transition in muonic ^{12}C : Search for new muon-nucleon interactions or accurate determination of the rms nuclear charge radius”, *Nuclear Physics A* **430**, 685–712 (1984).
- ³⁹T. Udem, A. Huber, B. Gross, J. Reichert, M. Prevedelli, M. Weitz, and T. W. Hänsch, “Phase-Coherent Measurement of the Hydrogen 1S – 2S Transition Frequency with an Optical Frequency Interval Divider Chain”, *Phys. Rev. Lett.* **79**, 2646–2649 (1997).
- ⁴⁰R. Pohl, A. Antognini, F. Nez, F. D. Amaro, F. Biraben, J. M. R. Cardoso, D. S. Covita, A. Dax, S. Dhawan, L. M. P. Fernandes, A. Giesen, T. Graf, T. W. Hänsch, P. Indelicato, L. Julien, C.-Y. Kao, P. Knowles, E.-O. Le Bigot, Y.-W. Liu, J. A. M. Lopes, L. Ludhova, C. M. B. Monteiro, F. Mulhauser, T. Nebel, P. Rabinowitz, J. M. F. dos Santos, L. A. Schaller, K. Schuhmann, C. Schwob, D. Taqqu, J. F. C. A. Veloso, and F. Kottmann, “The size of the proton”, *Nature* **466**, 213–216 (2010).
- ⁴¹R. Pohl, F. Nez, L. M. P. Fernandes, F. D. Amaro, F. Biraben, J. M. R. Cardoso, D. S. Covita, A. Dax, S. Dhawan, M. Diepold, A. Giesen, A. L. Gouvea, T. Graf, T. W. Hänsch, P. Indelicato, L. Julien, P. Knowles, F. Kottmann, E.-O. L. Bigot, Y.-W. Liu, J. A. M. Lopes, L. Ludhova, C. M. B. Monteiro, F. Mulhauser, T. Nebel, P. Rabinowitz, J. M. F. dos Santos, L. A. Schaller, K. Schuhmann, C. Schwob, D. Taqqu, J. F. C. A. Veloso, and A. Antognini, “Laser spectroscopy of muonic deuterium”, *Science* **353**, 669–673 (2016).
- ⁴²J. J. Krauth, K. Schuhmann, M. A. Ahmed, F. D. Amaro, P. Amaro, F. Biraben, T.-L. Chen, D. S. Covita, A. J. Dax, M. Diepold, L. M. P. Fernandes, B. Franke, S. Galtier, A. L. Gouvea, J. Götzfried, T. Graf, T. W. Hänsch, J. Hartmann, M. Hildebrandt, P. Indelicato, L. Julien, K. Kirch, A. Knecht, Y.-W. Liu, J. Machado, C. M. B. Monteiro, F. Mulhauser, B. Naar, T. Nebel, F. Nez, J. M. F. dos Santos, J. P. Santos, C. I. Szabo, D. Taqqu, J. F. C. A. Veloso, J. Vogelsang, A. Voss, B. Weichelt, R. Pohl, A. Antognini, and F. Kottmann, “Measuring the α -particle charge radius with muonic helium-4 ions”, *Nature* **589**, 527–531 (2021).
- ⁴³H. Gao and M. Vanderhaeghen, “The proton charge radius”, *Rev. Mod. Phys.* **94**, 015002 (2022).
- ⁴⁴A. Beyer, L. Maisenbacher, A. Matveev, R. Pohl, K. Khabarova, A. Grinin, T. Lamour, D. C. Yost, T. W. Hänsch, N. Kolachevsky, and T. Udem, “The Rydberg constant and proton size from atomic hydrogen”, *Science* **358**, 79–85 (2017).
- ⁴⁵N. Bezginov, T. Valdez, M. Horbatsch, A. Marsman, A. C. Vutha, and E. A. Hessels, “A measurement of the atomic hydrogen Lamb shift and the proton charge radius”, *Science* **365**, 1007–1012 (2019).
- ⁴⁶W. Xiong, A. Gasparian, H. Gao, D. Dutta, M. Khandaker, N. Liyanage, E. Pasyuk, C. Peng, X. Bai, L. Ye, K. Gnanvo, C. Gu, M. Levillain, X. Yan, D. W. Higinbotham, M. Mezziane, Z. Ye, K. Adhikari, B. Aljawrneh, H. Bhatt, D. Bhetuwal, J. Brock, V. Burkert, C. Carlin, A. Deur, D. Di, J. Dunne, P. Ekanayaka, L. El-Fassi, B. Emmich, L. Gan, O. Glamazdin, M. L. Kabir, A. Karki, C. Keith, S. Kowalski, V. Lagerquist, I. Larin, T. Liu, A. Liyanage, J. Maxwell, D. Meekins, S. J. Nazeer, V. Nelyubin, H. Nguyen, R. Pedroni, C. Perdrisat, J. Pierce, V. Punjabi, M. Shabestari, A. Shahinyan, R. Silwal, S. Stepanyan, A. Subedi, V. V. Tarasov, N. Ton, Y.

-
- Zhang, and Z. W. Zhao, “A small proton charge radius from an electron–proton scattering experiment”, *Nature* **575**, 147–150 (2019).
- ⁴⁷H. Fleurbaey, S. Galtier, S. Thomas, M. Bonnaud, L. Julien, F. Biraben, F. Nez, M. Abgrall, and J. Guéna, “New Measurement of the $1S - 3S$ Transition Frequency of Hydrogen: Contribution to the Proton Charge Radius Puzzle”, *Phys. Rev. Lett.* **120**, 183001 (2018).
- ⁴⁸A. D. Brandt, S. F. Cooper, C. Rasor, Z. Burkley, A. Matveev, and D. C. Yost, “Measurement of the $2S_{1/2} - 8D_{5/2}$ Transition in Hydrogen”, *Phys. Rev. Lett.* **128**, 023001 (2022).
- ⁴⁹V. A. Yerokhin and K. Pachucki, “Theoretical energies of low-lying states of light helium-like ions”, *Phys. Rev. A* **81**, 022507 (2010).
- ⁵⁰V. Patkóš, V. A. Yerokhin, and K. Pachucki, “Complete $\alpha^7 m$ Lamb shift of helium triplet states”, *Phys. Rev. A* **103**, 042809 (2021).
- ⁵¹V. A. Yerokhin, V. Patkóš, and K. Pachucki, “Relativistic Bethe logarithm for triplet states of helium-like ions”, *The European Physical Journal D* **76**, 142 (2022).
- ⁵²K. Pachucki and V. A. Yerokhin, “Fine Structure of Heliumlike Ions and Determination of the Fine Structure Constant”, *Phys. Rev. Lett.* **104**, 070403 (2010).
- ⁵³G. Drake, *Springer Handbook of Atomic, Molecular, and Optical Physics*, eng (Springer New York, NY, 2006).
- ⁵⁴E. A. Hylleraas, “Neue Berechnung der Energie des Heliums im Grundzustande, sowie des tiefsten Terms von Ortho-Helium”, *Z. Physik* **54**, 347–366 (1929).
- ⁵⁵I. Angeli and K. Marinova, “Table of experimental nuclear ground state charge radii: An update”, *Atomic Data and Nuclear Data Tables* **99**, 69–95 (2013).
- ⁵⁶I. Klaft, S. Borneis, T. Engel, B. Fricke, R. Grieser, G. Huber, T. Kühl, D. Marx, R. Neumann, S. Schröder, P. Seelig, and L. Völker, “Precision Laser Spectroscopy of the Ground State Hyperfine Splitting of Hydrogenlike $^{209}\text{Bi}^{82+}$ ”, *Phys. Rev. Lett.* **73**, 2425–2427 (1994).
- ⁵⁷A. Gumberidze, T. Stöhlker, D. Banaś, K. Beckert, P. Beller, H. F. Beyer, F. Bosch, S. Hagmann, C. Kozhuharov, D. Liesen, F. Nolden, X. Ma, P. H. Mokler, M. Steck, D. Sierpowski, and S. Tashenov, “Quantum Electrodynamics in Strong Electric Fields: The Ground-State Lamb Shift in Hydrogenlike Uranium”, *Phys. Rev. Lett.* **94**, 223001 (2005).
- ⁵⁸P. Beiersdorfer, H. Chen, D. B. Thorn, and E. Träbert, “Measurement of the Two-Loop Lamb Shift in Lithiumlike U^{89+} ”, *Phys. Rev. Lett.* **95**, 233003 (2005).
- ⁵⁹M. G. Kozlov, M. S. Safronova, J. R. Crespo López-Urrutia, and P. O. Schmidt, “Highly charged ions: Optical clocks and applications in fundamental physics”, *Rev. Mod. Phys.* **90**, 045005 (2018).
- ⁶⁰J. D. Gillaspy, “Highly charged ions”, *J. Phys. B* **34**, R93–R130 (2001).
- ⁶¹J. D. Gillaspy, J. M. Pomeroy, A. C. Perrella, and H. Grube, “The potential of highly charged ions: possible future applications”, *J. Phys.: Conf. Ser.* **58**, 451–456 (2007).

-
- ⁶²T. Stöhlker, T. Ludziejewski, H. Reich, F. Bosch, R. W. Dunford, J. Eichler, B. Franzke, C. Kozhuharov, G. Menzel, P. H. Mokler, F. Nolden, P. Rymuza, Z. Stachura, M. Steck, P. Swiat, A. Warczak, and T. Winkler, “Charge-exchange cross sections and beam lifetimes for stored and decelerated bare uranium ions”, *Phys. Rev. A* **58**, 2043–2050 (1998).
- ⁶³T. Kanesue, M. Kumaki, S. Ikeda, and M. Okamura, “Laser ion source for isobaric heavy ion collider experiment”, *Rev. Sci. Instrum.* **87**, 02A920 (2016).
- ⁶⁴G. D. Shirkov and G. Zschornack, *Electron Impact Ion Sources for Charged Heavy Ions*, eng (Vieweg+Teubner Verlag Wiesbaden, 1996).
- ⁶⁵M. Schmidt, A. Thorn, and G. Zschornack, *Electron Beam Ion Sources*, en, 2014.
- ⁶⁶W. Lotz, “An empirical formula for the electron-impact ionization cross-section”, *Z. Physik* **206**, 205–211 (1967).
- ⁶⁷A. Müller and E. Salzborn, “Scaling of cross sections for multiple electron transfer to highly charged ions colliding with atoms and molecules”, *Physics Letters A* **62**, 391–394 (1977).
- ⁶⁸Y. S. Kim and R. H. Pratt, “Direct radiative recombination of electrons with atomic ions: Cross sections and rate coefficients”, *Phys. Rev. A* **27**, 2913–2924 (1983).
- ⁶⁹B. M. Penetrante, J. N. Bardsley, D. DeWitt, M. Clark, and D. Schneider, “Evolution of ion-charge-state distributions in an electron-beam ion trap”, *Phys. Rev. A* **43**, 4861–4872 (1991).
- ⁷⁰J. Huba, *NRL Plasma Formulary* (Naval Research Laboratory, Washington, DC 20375, USA, 2013).
- ⁷¹J. A. Tully, “Total cross sections for electron impact excitation of the $1^1S \rightarrow 2^3S$ transition in He-like ions”, *J. Phys. B* **11**, 2923–2939 (1978).
- ⁷²S. Kaufman, “High-resolution laser spectroscopy in fast beams”, *Opt. Comm.* **17**, 309–312 (1976).
- ⁷³B. Schinzler, W. Klempt, S. Kaufman, H. Lochmann, G. Moruzzi, R. Neugart, E.-W. Otten, J. Bonn, L. Von Reisky, K. Spath, J. Steinacher, and D. Weskott, “Collinear laser spectroscopy of neutron-rich Cs isotopes at an on-line mass separator”, *Phys. Lett. B* **79**, 209–212 (1978).
- ⁷⁴R. Neugart, “Laser spectroscopy on mass-separated radioactive beams”, *Nucl. Instrum. Methods* **186**, 165–175 (1981).
- ⁷⁵A. Krieger, “Laser systems for collinear spectroscopy and the charge radius of ^{12}Be ”, eng, PhD thesis (Mainz, 2012).
- ⁷⁶W. Demtröder, *Laser Spectroscopy 1*, eng (Springer Berlin, Heidelberg, 2014).
- ⁷⁷W. Demtröder, *Laser Spectroscopy 2*, eng (Springer Berlin, Heidelberg, 2015).
- ⁷⁸M. Weidemüller and C. Zimmermann, *Ultracold Gases*, eng (WILEY-VCH Verlag Berlin GmbH, 2011).
- ⁷⁹W. Demtröder, *Experimentalphysik 3*, ger, 5th ed. (Springer, Heidelberg/Berlin, 2016).
- ⁸⁰K. König, J. Krämer, C. Geppert, P. Imgram, B. Maaß, T. Ratajczyk, and W. Nörtershäuser, “A new Collinear Apparatus for Laser Spectroscopy and Applied Science (COALA)”, *Rev. Sci. Instrum.* **91**, 081301 (2020).

-
- ⁸¹J. Krämer, K. König, C. Geppert, P. Imgram, B. Maaß, J. Meisner, E. W. Otten, S. Passon, T. Ratajczyk, J. Ullmann, and W. Nörtershäuser, “High-voltage measurements on the 5 ppm relative uncertainty level with collinear laser spectroscopy”, *Metrologia* **55**, 268–274 (2018).
- ⁸²K. L. König, “Laser-based high-voltage metrology with ppm accuracy”, en, PhD thesis (Technische Universität, Darmstadt, 2019).
- ⁸³P. Imgram, K. König, J. Krämer, T. Ratajczyk, R. A. Müller, A. Surzhykov, and W. Nörtershäuser, “Collinear laser spectroscopy at ion-trap accuracy: Transition frequencies and isotope shifts in the $6s^2S_{1/2} \rightarrow 6p^2P_{1/2,3/2}$ transitions in Ba^+ ”, *Phys. Rev. A* **99**, 012511 (2019).
- ⁸⁴P. Müller, K. König, P. Imgram, J. Krämer, and W. Nörtershäuser, “Collinear laser spectroscopy of Ca^+ : Solving the field-shift puzzle of the $4s^2S_{1/2} \rightarrow 4p^2P_{1/2,3/2}$ transitions”, *Phys. Rev. Research* **2**, 043351 (2020).
- ⁸⁵R. Powel, M. Koble, J. Palmes, N. Everett, P. Imgram, K. König, J. Lantis, K. Minamisono, W. Nörtershäuser, R. Parker, S. Pineda, F. Sommer, and A. Klose, “Improved wavelength meter calibration in near infrared region via doppler-free spectroscopy of molecular iodine”, *Appl. Phys. B* **127**, 104 (2021).
- ⁸⁶L. Renth, P. Imgram, J. Krämer, K. König, T. Lellinger, B. Maaß, P. Müller, T. Ratajczyk, and W. Nörtershäuser, “First experiments with a laser ablation source at the COALA setup”, *Hyperfine Interact.* **241**, 56 (2020).
- ⁸⁷T. Ratajczyk, P. Bollinger, T. Lellinger, V. Varentsov, and W. Nörtershäuser, “Towards a He-buffered laser ablation ion source for collinear laser spectroscopy”, *Hyperfine Interact.* **241**, 52 (2020).
- ⁸⁸T. Ratajczyk, “Isotope shift measurements in Ti^+ transitions using laser-ablated and thermalized ions”, en, PhD thesis (Technische Universität, Darmstadt, 2022).
- ⁸⁹L. Renth, D. Hanstorp, P. Imgram, D. Koestel, D. Lu, B. Maaß, W. Nörtershäuser, and T. Walther, *Collinear laser spectroscopy on photodetached atoms*, to be published.
- ⁹⁰B. Maaß, K. König, J. Krämer, A. J. Miller, K. Minamisono, W. Nörtershäuser, and F. Sommer, *A 4 fluorescence detection region for collinear laser spectroscopy*, published on arXiv.org: <https://arxiv.org/abs/2007.02658>, 2020.
- ⁹¹F. Ullmann, “Untersuchung der Erzeugung hochgeladener Ionen in einer Raumtemperatur-Elektronenstrahl-Ionenfalle”, de, PhD thesis (Technische Universität, Dresden, 2005).
- ⁹²J. Fischer, *Erzeugung hochgeladener Ionen von Bor, Eisen und Antimon für Experimente auf der HITRAP Plattform*, de, Bachelor Thesis, Darmstadt, Sept. 2017.
- ⁹³V. Chohan, C. Alanzeau, M. E. Angoletta, J. Baillie, D. Barna, W. Bartmann, P. Belochitskii, J. Borburgh, H. Breuker, F. Butin, M. Buzio, O. Capatina, C. Carli, E. Carlier, M. Cattin, T. Dobers, P. Chiggiato, L. Ducimetiere, T. Eriksson, S. Fedemann, T. Fowler, R. Froeschl, R. Gebel, N. Gilbert, S. Hancock, J. Harasimowicz, M. Hori, L. V. Jorgensen, R. Kersevan, D. Kuchler, J. M. Lacroix, G. LeGodec, P. Lelong, L. Lopez-Hernandez, S. Maury, J. Molendijk, B. Morand, A. Newborough, D. Nisbet, A. Nosych, W. Oelert, M. Paoluzzi, S. Pasinelli, F. Pedersen, D. Perini, B. Puccio, J. Sanchez-Quesada, D. Schoerling, L. Sermeus, L. Soby,

-
- M. Timmins, D. Tommasini, G. Tranquille, G. Vanbavinckhove, A. Vorozhtsov, C. Welsch, and T. Zickler, *Extra Low ENergy Antiproton (ELENA) ring and its Transfer Lines: Design Report*, CERN Yellow Reports: Monographs (CERN, Geneva, 2014).
- ⁹⁴S. Kaufmann, “Laser spectroscopy of nickel isotopes with a new data acquisition system at ISOLDE”, en, PhD thesis (Technische Universität, Darmstadt, 2019).
- ⁹⁵S. B. Reinhardt, “Measurement of time dilation by laser spectroscopy on fast stored Lithium Ions”, en, PhD thesis (Universität Heidelberg, Heidelberg, 2005).
- ⁹⁶K. König, J. Krämer, P. Imgram, B. Maaß, W. Nörtershäuser, and T. Ratajczyk, “Transition frequencies and hyperfine structure in $^{113,115}\text{In}^+$: Application of a liquid-metal ion source for collinear laser spectroscopy”, *Phys. Rev. A* **102**, 042802 (2020).
- ⁹⁷J. Spahn, “Untergrundbereinigte kollineare Sättigungsspektroskopie an $^{12}\text{C}^{4+}$ ”, ger, Bachelor Thesis (TU Darmstadt, 2022).
- ⁹⁸S. Ozawa, T. Ariga, N. Inabe, M. Kase, I. Tanihata, M. Wakasugi, and Y. Yano, “Isotope Shift Measurement Between He-like ^{12}C and ^{13}C Ions in $1s2s\ ^3\text{S}_1 - 1s2p\ ^3\text{P}_{0,1,2}$ Transitions”, *Physica Scripta* **T92**, 195–196 (2001).
- ⁹⁹B. Edlen and B. Lofstrand, “The term systems of C V”, *J. Phys. B* **3**, 1380–1388 (1970).
- ¹⁰⁰G. W. Drake, “Theoretical energies for the $n = 1$ and 2 states of the helium isoelectronic sequence up to $Z = 100$ ”, *Can. J. Phys.* **66**, 586–611 (1988).
- ¹⁰¹T. Zelevinsky, D. Farkas, and G. Gabrielse, “Precision Measurement of the Three 2^3P_J Helium Fine Structure Intervals”, *Phys. Rev. Lett.* **95**, 203001 (2005).
- ¹⁰²J. S. Borbely, M. C. George, L. D. Lombardi, M. Weel, D. W. Fitzakerley, and E. A. Hessels, “Separated oscillatory-field microwave measurement of the $2\ ^3P_1 - -2\ ^3P_2$ fine-structure interval of atomic helium”, *Phys. Rev. A* **79**, 060503 (2009).
- ¹⁰³E. Riis, A. G. Sinclair, O. Poulsen, G. W. F. Drake, W. R. C. Rowley, and A. P. Levick, “Lamb shifts and hyperfine structure in $^6\text{Li}^+$ and $^7\text{Li}^+$: Theory and experiment”, *Phys. Rev. A* **49**, 207–220 (1994).
- ¹⁰⁴T. J. Scholl, R. Cameron, S. D. Rosner, L. Zhang, R. A. Holt, C. J. Sansonetti, and J. D. Gillasp, “Precision measurement of relativistic and QED effects in heliumlike beryllium”, *Phys. Rev. Lett.* **71**, 2188–2191 (1993).
- ¹⁰⁵T. P. Dinneen, N. Berrah-Mansour, H. G. Berry, L. Young, and R. C. Pardo, “Precision measurements of relativistic and QED effects in helium-like boron”, *Phys. Rev. Lett.* **66**, 2859–2862 (1991).
- ¹⁰⁶J. K. Thompson, D. J. H. Howie, and E. G. Myers, “Measurements of the $1s2s\ ^1\text{S}_0 - 1s2p\ ^3\text{P}_{1,0}$ transitions in heliumlike nitrogen”, *Phys. Rev. A* **57**, 180–188 (1998).
- ¹⁰⁷E. G. Myers, H. S. Margolis, J. K. Thompson, M. A. Farmer, J. D. Silver, and M. R. Tarbutt, “Precision Measurement of the $1s2p\ ^3\text{P}_2 - ^3\text{P}_1$ Fine Structure Interval in Heliumlike Fluorine”, *Phys. Rev. Lett.* **82**, 4200–4203 (1999).

-
- ¹⁰⁸W. Nörtershäuser, D. Tiedemann, M. Žáková, Z. Andjelkovic, K. Blaum, M. L. Bissell, R. Cazan, G. W. F. Drake, C. Geppert, M. Kowalska, J. Krämer, A. Krieger, R. Neugart, R. Sánchez, F. Schmidt-Kaler, Z.-C. Yan, D. T. Yordanov, and C. Zimmermann, “Nuclear Charge Radii of $^{7,9,10}\text{Be}$ and the One-Neutron Halo Nucleus ^{11}Be ”, *Phys. Rev. Lett.* **102**, 062503 (2009).

Curriculum Vitae

Phillip Imgram

Graduation

- 04/2018 - 12/2022 Graduation in the group of Prof. Wilfried Nörtershäuser,
Institut für Kernphysik, Technische Universität Darmstadt.
Thesis title: *High-precision laser spectroscopy of helium-like carbon $^{12}\text{C}^{4+}$*
- Regular participation at experiments at
GSI Helmholtzzentrum für Schwerionenforschung Darmstadt,
CERN European Organization for Nuclear Research, Geneva,
NSCL National Superconducting Laboratory, East Lansing,
Argonne National Laboratory, Chicago,
University of Jyväskylä.
- Member of the Sonderforschungsbereich SFB 1245
Member of the Helmholtz Graduate School for Hadron and Ion Research
Member of the Graduiertenschule Giersch
Awarded with the Giersch-Excellence-Award 2019 & 2022
- Certified Laser Safety Officer

Academic education

- 10/2012 - 03/2018 Studies of physics, Technische Universität Darmstadt
- 03/2017 - 04/2018 Master's degree in the group of Prof. Wilfried Nörtershäuser,
Institut für Kernphysik, Technische Universität Darmstadt.
Thesis title: *Accurate isotope shift measurements in the
 $6s\ ^2\text{S}_{1/2} \rightarrow 6p\ ^2\text{P}_{1/2,3/2}$ lines of Ba^+*
- 10/2015 - 02/2016 Bachelor's degree in the group of Prof. Wilfried Nörtershäuser
Institut für Kernphysik, Technische Universität Darmstadt.
Thesis title: *Aufbau eines Diodenlasersystems mit*

Frequenzverdopplung am ALIVE-Experiment

School education

06/2012 Abitur at Einhardschule Seligenstadt

List of publications

Publications in peer-reviewed journals

Charge Radii of $^{55,56}\text{Ni}$ Reveal a Surprisingly Similar Behavior at $N = 28$ in Ca and Ni Isotopes

Felix Sommer, Kristian König, Dominic M. Rossi, Nathan Everett, David Garand, Ruben P. de Groote, Jason D. Holt, Phillip Imgram, Anthony Incorvati, Colton Kalman, Andrew Klose, Jeremy Lantis, Yuan Liu, Andrew J. Miller, Kei Minamisono, Takayuki Miyagi, Witold Nazarewicz, Wilfried Nörtershäuser, Skyy V. Pineda, Robert Powel, Paul-Gerhard Reinhard, Laura Renth, Elisa Romero-Romero, Robert Roth, Achim Schwenk, Chandana Sumithrarachchi, and Andrea Teigelhöfer
Phys. Rev. Lett. 129, 132501 (2022)

Evidence of a sudden increase in the nuclear size of proton-rich silver-96

M. Reponen, R. P. de Groote, L. Al Ayoubi, O. Beliuskina, M. L. Bissell, P. Campbell, L. Cañete, B. Cheal, K. Chrysalidis, C. Delafosse, A. de Roubin, C. S. Devlin, T. Eronen, R. F. Garcia Ruiz, S. Geldhof, W. Gins, M. Hukkanen, P. Imgram, A. Kankainen, M. Kortelainen, Á. Koszorús, S. Kujanpää, R. Mathieson, D. A. Nesterenko, I. Pohjalainen, M. Vilén, A. Zadvornaya, and I. D. Moore
Nature Communications 12, 4596 (2021)

Probing the single-particle behavior above ^{132}Sn via electromagnetic moments of $^{133,134}\text{Sb}$ and $N = 82$ isotones

S. Lechner, Z. Y. Xu, M. L. Bissell, K. Blaum, B. Cheal, G. De Gregorio, C. S. Devlin, R. F. Garcia Ruiz, A. Gargano, H. Heylen, P. Imgram, A. Kanellakopoulos, Á. Koszorús, S. Malbrunot-Ettenauer, R. Neugart, G. Neyens, W. Nörtershäuser, P. Plattner, L. V. Rodríguez, X. F. Yang, and D. T. Yordanov
Phys. Rev. C 104, 014302 (2021)

Improved wavelength meter calibration in near infrared region via Doppler-free spectroscopy of molecular iodine

Robert Powel, MaKenna Koble, Julian Palmes, Nathan Everett, Phillip Imgram, Kristian König, Jeremy Lantis, Kei Minamisono, Wilfried Nörtershäuser, Ryan Parker, Skyy Pineda, Felix Sommer, and Andrew Klose
Appl. Phys. B 127, 104 (2021)

Collinear laser spectroscopy of Ca^+ : Solving the field-shift puzzle of the $4s^2S_{1/2} \rightarrow 4p^2P_{1/2,3/2}$ transitions

Patrick Müller, Kristian König, Phillip Imgram, Jörg Krämer, and Wilfried Nörtershäuser
Phys. Rev. Research 2, 043351 (2020)

Transition frequencies and hyperfine structure in $^{113,115}\text{In}^+$: Application of a liquid-metal ion source for collinear laser spectroscopy

Kristian König, Jörg Krämer, Phillip Imgram, Bernhard Maaß, Wilfried Nörtershäuser, and Tim Ratajczyk
Phys. Rev. A 102, 042802 (2020)

A new Collinear Apparatus for Laser Spectroscopy and Applied Science (COALA)

K. König, J. Krämer, C. Geppert, P. Imgram, B. Maaß, T. Ratajczyk, and W. Nörtershäuser
Review of Scientific Instruments 91, 081301 (2020)

On the performance of wavelength meters: Part 2—frequency-comb based characterization for more accurate absolute wavelength determinations

Kristian König, Phillip Imgram, Jörg Krämer, Bernhard Maaß, Konstantin Mohr, Tim Ratajczyk, Felix Sommer, and Wilfried Nörtershäuser
Appl. Phys. B 126, 86 (2020)

Collinear laser spectroscopy at ion-trap accuracy: Transition frequencies and isotope shifts in the $6s^2S_{1/2} \rightarrow 6p^2P_{1/2,3/2}$ transitions in Ba^+

Ph. Imgram, K. König, J. Krämer, T. Ratajczyk, R. A. Müller, A. Surzhykov, and W. Nörtershäuser
Phys. Rev. A 99, 012511 (2019)

High voltage measurements on the 5 ppm relative uncertainty level with collinear laser spectroscopy

J. Krämer, K. König, Ch. Geppert, P. Imgram, B. Maaß, J. Meisner, E. W. Otten, S. Passon, T. Ratajczyk, J. Ullmann, and W. Nörtershäuser
Metrologia 55, 268 (2018)

Conference Contributions

Collinear Laser Spectroscopy of Helium-like $^{11}\text{B}^{3+}$

Konstantin Mohr, Axel Buß, Zoran Andelkovic, Volker Hannen, Max Horst, Phillip Imgram, Kristian König, Bernhard Maaß, Wilfried Nörtershäuser, Simon Rausch, Rodolfo Sánchez and Christian Weinheimer

Atoms 11(1), 11 (2023)

High-precision collinear laser spectroscopy at the Collinear Apparatus for Laser Spectroscopy and Applied Physics (COALA)

P. Imgram, K. König, J. Krämer, T. Ratajczyk, B. Maaß, P. Müller, F. Sommer, and W. Nörtershäuser
Hyperfine Interact 241, 48 (2020)

Accurate high voltage measurements based on laser spectroscopy

K. König, Ch. Geppert, P. Imgram, B. Maaß, J. Meisner, W. Nörtershäuser, E.W. Otten, S. Passon, T. Ratajczyk, J. Ullmann, and J. Krämer

VDE High Voltage Technology 2018; ETG-Symposium, pp. 1-4. (2018)

High Voltage Metrology with Collinear Laser Spectroscopy

J. Krämer, K. König, C. Geppert, P. Imgram, B. Maaß, J. Meisner, E. W. Otten, S. Passon, T. Ratajczyk, J. Ullmann, and W. Nörtershäuser

Conference on Precision Electromagnetic Measurements (CPEM 2018), pp. 1-2 (2018)

Acknowledgments

I started my studies in Darmstadt 10 years ago and besides all the gathered knowledge and experiences, I most importantly met great people and made new friends which I would like to thank in this section.

First of all, I want to thank Wilfried Nörtershäuser who mentored and guided me since my Bachelor's thesis in 2015. Especially during my PhD, he gave me the opportunity to work in this fascinating field and he always took the time to discuss ideas and problems even at his most busy days. Furthermore, he enabled me to participate in various on-line beamtimes and summer schools all over the world where I made connections to brilliant scientist from whom I learned a lot.

In the laboratory, I really enjoyed to work with Jörg, Kristian, Bernhard and Patrick. You are all great minds and have always constructive ideas to overcome challenges. At the same time, we also had a lot of fun together which made the work always diverting.

Of course I also have to thank the rest of the current but also former LaserSpHERE group members for all the provided help and an always great atmosphere. Especially the usually immediate TILDA support during tense beamtimes from Simon and Felix saved a lot of my nerves. Thank you!

I wish to thank Joachim Enders, Robert Roth and Thomas Walther that they agreed to take part in my examination.

I also want to thank the administration of the IKP namely Giovanna Umberti and Carina Seeger who were always happily helping in the jungle of bureaucracy. Similarly, I want to thank the whole mechanical and electronic workshop teams of the IKP who have supplied many parts of the COALA beamline.

For the laser part, I want to thank Mr. Wünsche and Mr. Borstel from Sirah Lasertechnik GmbH. They always supported me when problems with our laser system occurred and tried to organize spare parts as fast as possible.

Natürlich muss ich mich auch bei meiner Studentenclique mit Martin (Mathieu), Felix, Yannik, Max, Patrick, Markus und Sascha bedanken. Wir haben uns am Anfang unseres Studium kennengelernt und einfach eine unfassbar gute und vor allem lustige Zeit gehabt, die ich auf keinen Fall missen möchte. Es gibt so viele Geschichten die wir zusammen erlebt haben und die mir hoffentlich für immer im Gedächtnis bleiben. Vor allem haben wir schon lange vor Corona erkannt, wie praktisch Homeoffice ist ;) Auch wenn wir uns mittlerweile leider nicht mehr ganz so häufig sehen auf Grund von verschiedensten Wohnorten, seid ihr bei mir immer herzlich willkommen!

Ich möchte mich auch nochmal extra bei Bernhard, Kristian und Felix bedanken. Nicht nur im Labor, sondern auch auch bei diversen Grill-, Kneipen- und Skatabenden hatte ich viel Spaß mit euch. Auch die Zeit in den USA auf verschiedensten Wanderungen mit Bernhard und Felix werden mir immer in toller Erinnerung bleiben.

Vielen Dank auch an meine Seligenstädter Freunde und Fußballkollegen, allen voran Marcel, Kai, Mona, Robin, Frederick, Riccarda, Jannis, Inga, Kevin, Louis, Carlos usw. (sorry wenn sich hier jemand vermisst). Durch euch kann ich auch mal an was anderes als Physik denken. Das tut mir gut und hilft mir auch manchmal einfach nochmal neu anzusetzen und dadurch eine Lösung zu finden.

Einen sehr großen Anteil an meinem Weg bis hierher hat selbstverständlich auch meine Familie, allen voran mein Opa Josef und Oma Hannelore, meine Eltern Andrea und Bardo, mein Bruder Johannes, aber natürlich auch Bärbel. Ihr habt mich immer unterstützt und gefördert wo es euch möglich war. Vielen Dank dafür!

Nadine, vielen Dank für alles was du für mich tust. Mit deiner Liebe und Geduld unterstützt du mich mehr als du denkst. Ich weiß, dass es manchmal nicht ganz einfach mit mir ist, aber du schaffst es mit deiner positiven Art mich selbst nach einem Tag, an dem einfach nichts geklappt hat, aufzubauen und auf andere Gedanken zu bringen. Du hast immer einen Platz in meinem Herz.

„Wer Newton nicht ehrt, ist Einstein nicht wert.“
– Kai Friedrich